12-2012

Hydromechanical Well Testing Using a 3D Fiber Optic Extensometer

Glenn Skawski
Clemson University, glenns487@gmail.com

HYDROMECHANICAL WELL TESTING USING A 3D FIBER OPTIC EXTENSOMETER

A Thesis
Presented to
the Graduate School of
Clemson University

In Partial Fulfillment
of the Requirements for the Degree
Master of Science
Hydrogeology

by
Glenn Skawski
December 2012

Accepted by
Dr. Lawrence C. Murdoch
Dr. Ronald Falta
Dr. Stephen Moysey

ABSTRACT

Some fractured rock formations hold important resources, such as water, hydrocarbons or heat, whereas others are good candidates for waste disposal. Hydromechanical well tests have been developed to improve characterization of formation properties and parameter distributions by measuring displacement along with pressure while stressing a well. The displacement that occurs during a well test depends on the geometry of fractures or other sources of permeability, as well as the distribution of compliance or elastic modulus. Current methods of hydromechanical well testing, measures axial displacements along a wellbore, which may cause ambiguity in interpretations when 3-D components of deformation are present. The objectives of this research are to develop an instrument that can measure deformation of rock enveloping wells in three dimensions using technology that will facilitate applications over a wide range of conditions, and demonstrate the performance of this device during well tests in shallow wells in fractured rock. The approach is to use fiber optic strain gauges attached to a flexible coupling, which can move through 5 degrees of freedom. The device that was developed, which will be called the 3DX, has the capability to be lowered in a borehole, anchored into a desired section for testing, and deployed in a different location or removed from the borehole. Transverse displacement is calculated by taking the difference of strain measured between two opposing gauges, whereas axial displacement is calculated from the average displacement of the gauges. The RMS noise level of a 5-minute sample at 1 Hz is 80 nm in the axial direction, and 250 nm in the transverse direction based on field data and calibration factors determined in the lab. Field tests

were conducted in Japan in the summer of 2011, and in Clemson, SC and Trenton, NJ during summer, 2012. The field tests show that the 3DX compressed axially approximately 3 to 6 μm per meter of drawdown and extended axially when the pressure increases. The transverse displacement was approximately 6 to 12 μm towards the south-southeast during the tests at Clemson in fractured gneiss at a depth of 25m. This is similar to the tilt direction from tiltmeters, providing a field validation of the measurements. The interpretation is that tilting is caused by a fracture that strikes roughly E-W and dips to the south. During ambient conditions in an open borehole the 3DX responds to changes in barometric pressure by closing approximately 0.15 μm with a 2 cm change in head when the water level rises and opening similarly when the water level drops.

The results suggest that 3D displacement can be measured during pumping and ambient monitoring in a rock enveloping borehole. The inclusion of the transverse displacement signal allows fracture orientation to be evaluated.

DEDICATION

To my parents, Brittany, and TNVT

ACKNOWLEDGMENTS

TABLE OF CONTENTS

LIST OF FIGURES

1. INTRODUCTION

Oil, natural gas, heat, and water can be recovered from subsurface formations and CO_2 can be stored there, so improving the understanding of fluid flow and storage in aquifer materials has the potential to advance understanding of resource recovery or storage. Well tests have long been used to evaluate the properties of subsurface materials (Theis, 1935), and they are a key component in understanding flow and storage processes.

A variety of well tests have been proposed, but a common one is to pump a well at constant rate and measure the resulting pressure, or hydraulic head, at pumping and monitoring wells. A typical approach is to invert an analytical solution (Theim 1906; Theis 1935; Barker 1988; Cooper and Jacob 1946; M. S. Hantush 1956; Neuman and Witherspoon 1969;) that considers geometry appropriate for the site in order to estimate aquifer parameters. One pitfall with this approach is that it requires averaging aquifer properties over large scales, so heterogeneities below that scale cannot be resolved. The result is that multiple combinations of subsurface geometries and properties can result in the same average parameters. This type of non-unique interpretation is particularly common in fractured rock where geometries and properties of fracture networks can be highly variable. Some applications may only require broad, average estimates of aquifer properties, but finer resolution of aquifer properties will improve many applications.

One strategy to improve the resolution of well tests is to use additional data to better constrain the interpretation. Displacements of the aquifer or casing occur in response to pressure changes in aquifers, and the magnitude and direction of

displacements depend on the distribution of aquifer properties. The dependence of displacements on aquifer properties makes them a suitable candidate for improving the resolution of well tests. Including displacement measurements along with a pressure signal is called *hydromechanical well testing* (Gale 1975; Cappa 2005; Schweisinger et al. 2009). Techniques for measuring and interpreting hydromechanical well tests have been developed (Murdoch and Germanovich 2006; Svenson et al. 2007; Cappa et al. 2009; Schweisinger et al. 2009), and this technique shows promise for improving understanding of rock aquifers (Cappa et al. 2009; Cappa et al. 2005; Svenson et al. 2008, Schweisinger and Murdoch 2011).

Previous measurements during hydromechanical well tests have been limited to axial displacements along the wellbore (Svenson et al. 2008; Schweisinger and Murdoch 2011; Martin et al. 1990), and interpretations have assumed the fracture being tested is flat lying. This assumption is acceptable as a first approximation because permeable fractures at shallow depths commonly are roughly flat-lying (). At the Clemson field site, for example, three major permeable zones with dips less than 20° are recognized (Slack 2010). Slack (2010) used a Modified Line Search to adjust the location of packers used for slug tests in four boreholes to match conductive zones in boreholes. The results are that the top zone is at 26 m and is poorly connected relative to the other two zones. There is a fractured zone 4 meters thick with a moderate K at 35 meters, and the lowest zone is a single flat lying fracture at 47 meters. All the zones strike to approximately east to west and dips to the south (Slack 2010). Gently-dipping fracture zones are also recognized at

other sites underlain by crystalline rock (Ruelleu et al. 2010; Jancin and Ebaugh 2002; Lecomte et al. 2011; Williams and Burton 200).

Despite the common occurrence of gently dipping fractures, most fractured rock sites also include fractures with moderate to steep dips, and gently dipping fractures probably are characterized by lateral heterogeneities in aperture. These effects will result in displacements transverse to the wellbore that are not resolved by axial measurements. In cases of a single dipping fracture, for example, opening of the fracture during a well test will cause displacements that are both axial and transverse to the borehole. Measuring only the axial component will underestimate the total response of the fracture by an amount that increases with dip of the fracture. Assuming that the axial displacement represents the total response will underestimate the response of the fracture, and this will cause the hydraulic compliance of the fracture to be underestimated.

A similar problem occurs where lateral heterogeneities are present. In some cases it is possible to estimate the presence of lateral heterogeneities from axial displacements alone (Svenson et al. 2007; Schweisinger 2011; Cappa et al. 2005), but the direction of the heterogeneity cannot be determined. Axial displacement may be only weakly sensitive to other lateral heterogeneities, so axial measurements may simply be unable to resolve these cases.

Hydromechanical well tests have the potential to advance the reliability of CO_2 sequestration by improving the ability to characterize injection intervals and by detecting deformation caused by leakage. Technology developed for hydromechanical well tests has focused on electromagnetic sensors (Hisz et al. 2012), which provide excellent

resolution, but with several drawbacks. These sensors are vulnerable to electromagnetic interference, which could impact performance in the field. Moreover, they require power and signal conditioning at depth, and it may be impractical to keep these electronic components operational during long deployments. 3D measurements will require perhaps as many as 8 sensors, which will further increase the burden of downhole electronics.

Optical fiber strain gauges have the potential to address many of the problems recognized for electromagnetic sensors. However, optical fiber gauges have never been evaluated for use during hydromechanical well tests, so their applicability remains unknown.

The main objective of this work is to evaluate the feasibility of measuring both transverse and axial displacements during hydromechanical well tests. This will improve the resolution of hydromechanical data, and it will allow the assumption that displacements are largely axial (or vertical) in settings where fractures are gently dipping to be verified. Another objective is to evaluate the feasibility of using fiber optic strain gauges as displacement sensors during hydromechanical well tests in order to prepare for applications in deep wells used for CO_2 sequestration or petroleum applications.

The following section introduces the general topics of flow through fractured rock and well testing addressed by the thesis, and it introduces the main objectives and approach of the research.

FRACTURE MODEL

        To understand how fractures affect aquifer properties it is important to develop a

conceptual model that idealizes fracture characteristics. The hydraulic conductivity is a

property of the material, and the transmissivity is a property of the aquifer. Therefore, a

single fracture is analogous to a porous, confined aquifer for which the transmissivity is

the product of the hydraulic conductivity and thickness (Golder Associates 2010)

$$K = 1/b \sum_{i=1}^{n} T_n$$

<div align="right">(1.0.1)</div>

where K is the hydraulic conductivity, b is the aquifer thickness, and T is the

transmissivity. The transmissivity of a fracture is commonly described by the cubic law

$$T = \frac{\delta^3 \rho g}{12 \mu}$$

<div align="right">(1.1)</div>

where δ is the aperture, ρ is the fluid density, g is the gravitational constant, and μ is

the dynamic viscosity. The cubic law assumes that the boundaries of the fracture are

composed of two smooth parallel plates (Witherspoon et. al., 1979; Olsson and Barton,

2000). The distance between the plates is the aperture. Expanding on this model would

be to assume that both boundaries of a fracture are rough (Figure 1.1). This is

represented by two plates in contact by protruding asperities (Neuzil and Tracy 1981;

Pollard and Aydin, 1988; Tsang and Witherspoon 1983). Beneath the water table where

the rock is saturated, the fracture consists of contacting asperities and water-filled voids.

The fracture is held open by the stress on the contacting asperities and the fluid pressure

<div align="center">5</div>

in the voids (Murdoch and Germanovich 2006). The fracture will deform and the aperture will change when the total stress on the fracture face changes.
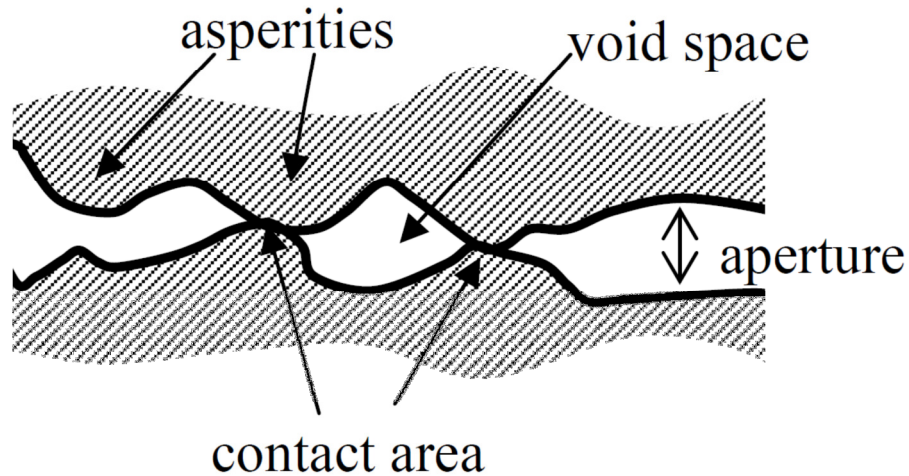
Figure 1.1: Idealized model of a fracture (Alm 1999).

AQUIFER PROPERTIES

      A fractured aquifer will contain many of these fractures that contribute to the storage and flow. The hydraulic conductivity (K) and storativity (S) are aquifer properties that are affected by the effective properties of fractures in the aquifer. Hydraulic conductivity relates the fluid flow to the driving head gradient (Fetter, 2001). In fractured rock, the hydraulic conductivity is related to the size, connectivity, shape, orientation and spacing of fractures, fluid viscosity, and fluid density. Storativity is the volume of water released per area of fracture in response to a unit change in fluid pressure within the void spaces (Fetter, 2001)

$$S = \frac{\Delta V}{A \Delta H}$$

(1.2)

6

where, *V* is a volume of water released from storage, *A* is an area of fracture, and *h* is the hydraulic head in the void spaces. Storativity is related to the normal stiffness of the formation, k_n, and compressibility of water, C_f. The compliance of the formation depends on the orientation and spacing of individual fractures. Thus, S of a confined aquifer can be expressed as (Doe et al. 1982)

$$S = g\rho(\frac{1}{k_n} + C_f\delta)$$
(1.3)

where ρ is the density of water, δ is the fracture aperture, and *g* is the acceleration due to gravity.

    The hydraulic conductivity and the storativity are affected by the fracture aperture, which changes as a function of effective stress. The reason for this is as the effective stress changes as a function of fluid pressure the fracture aperture is affected by the stress related rock properties.

$$\delta_L(r) = \delta_0 - \frac{\sigma_e}{k_n}$$
(1.01)

where $\delta_L(r)$ is the local aperture a radial distance, *r*, from the wellbore, δ_0 is the aperture when effective stress is zero, and k_n is the normal stiffness of the fracture (Murdoch and Germonovich 2006).

CONSTANT RATE PUMPING TESTS

Aquifer characterization involves measuring aquifer parameters (fracture aperture, fracture density, etc.) in the field, and using inversion to match analytical models to estimate aquifer properties (hydraulic conductivity and storativity). An estimation of the fluid flow and storage of the aquifer is made by adjusting the aquifer properties until the results of analytical models match field data.

A constant-rate well test is a common testing method that involves pumping water from a well, and measuring the pressure through time at either the pumping or monitoring wells. The injection or withdrawal should be large enough so the flow rate is measureable, but not so large that it changes the properties of the rock (N. R. C., 1996). Pumping causes fluid flow towards the well, and induces a hydraulic head gradient in the formation. The hydraulic conductivity and storativity controls the shape of the hydraulic head gradient. We can infer the aquifer properties from the drawdown as a function of time in the well because it is sensitive to the hydraulic conductivity and storativity of the aquifer.

There are many methods used for interpreting the hydraulic conductivity and storativity from the hydraulic well test data (Kruseman and deRidder 1994; Dawson and Istok 1991; Butler 1997). Many of the methods used assume that the aquifer is composed of porous media, where the aquifer properties are homogeneous and independent of radial distance from the well (Kruseman and deRidder 1994; Dawson and Istok 1991; Butler 1997). The distribution of fractures within the matrix ranges from simple, regular patterns tocomplex and irregular patterns. Analyses of the

8

drawdown in fractured aquifers of different characteristics are given by Gringarten and Ramey (1974),; Barker and Black (1983), Doe and Osnes (1985) Elsworth and Doe (1986), and Karasaki et al. (1988). Analyses are also available to identify hydraulic boundaries (Chapuis 1994; Butler 1997), lateral heterogeneities (Fenske 1984; Streltosova 1988; Grader 1991) and dual porosity (Moench 1988; Streltsova 1988).

Another problem when measuring drawdown with time is that there may be different sets of hydraulic conductivity and storativity values that match the field measured drawdown with time. This is referred to as non-uniqueness (Doe and Osnes 1985; Elsworth and Doe 1986; Hsieh 2000). Analysis of hydraulic well tests have been developed that attempt to address this problem by measuring other types of field data, and use it in combination with the pressure change to increase the analytical accuracy.

To improve the performance of hydraulic well tests the Clemson research group (Svenson, 2006; Schweisinger 2007; and Slack 2010) has been measuring axial fracture displacements during slug and pumping tests. The compliance is related to storativity because dropping the pressure in the formation will cause the fracture aperture to close and releasing fluids from storage, and the magnitude of this effect depends on the compliance. This allows a more accurate estimate of storativity. The aperture change as a function of displacement is also valuable because it is related to the fracture distribution throughout the aquifer. This is important because previous analysis of fluid flow and fracture deformation assume that changes in storage result from deformations in response to local pressure changes, and flow properties are independent of fluid pressure (Long et al. 1982). This is assumption is not viable because previous tests have shown that

9

displacement is a hysteretic function of pressure; displacements early in a test when head is decreasing are always less than when the pressure change is increasing during recovery. This occurs because displacement depends on the distribution of pressure throughout the aquifer, not just on the local pressure at the well bore (Murdoch and Germanovich, 2006).

This coupling between elastic deformation and the pore fluid pressure is described by the theory of poroelasticity (Biot 1956; Geertsma 1966). It can be used to analyze stress changes and displacement during fluid extraction or injection in fluid-saturated rock formations (Settari 2002; Fabian and Kumpel 2003; Kim and Parizek 2005; Kim and Parizek 1997; Yin et al. 2007; Tseng et al. 2008) or how changes in loads applied to the surface of an aquifer change water-level in wells (Wang 2000; Schevenels et al. 2004; Theodorakopoulos et al. 2004; Comerlati et al. 2004; Tsai 2009).

Poroelasticity involves a solid-to-fluid coupling where a change in applied stress produces a change in fluid pressure or mass, and a fluid-to-solid coupling where a change in fluid pressure produces a change in the volume of the porous media (Wang, 2000). In fractures increasing the fluid pressure opens the aperture, which affects the fluid pressure along the length of the fracture (Schweisinger 2007). Due to this effect fractures can be treated as thin layers that deform using the fluid and solid coupling associated with poroelasticity (Murdoch and Germanovich 2006).

HYDROMECHANICAL WELL TESTING

The aquifer characterization method that measures displacements during pressure changes is a hydromechanical well test. The measured displacement and pressure change can be used to calculate the hydraulic compliance

$$C_n = \frac{d\delta}{dP}$$

(1.9)

The compliance can be used to determine the storativity of a single fracture using assumptions from Doe et al. (1982), Rutqvist (1995), and Rutqvist et al. (1998). This translates to (Schweisinger et al. 2009)

$$S \approx \gamma \alpha C_n$$

(1.10)

where γ is the unit weight of water and α is the ratio of void area to total fracture area.

Previous hydromechanical well tests have measured only axial displacement (Schweisinger et al. 2011; Svenson et al. 2008). The analysis of these data assumes that a fracture is flat and radially extending from the borehole. Certain heterogeneities such as leakage and blockage can be inferred from the results (Schweisinger et al. 2011). We would like to improve on this and measure deformation in three dimensions. This will include axial displacement along the length of the borehole and displacements transverse to the axis of the borehole. With the addition of monitoring transverse displacement, it may be possible to detect preferential flow paths such as fracture zones in the aquifer. This occurs because during pumping there will be volume changes that induce displacements. In a horizontal and homogeneous formation the induced transverse

displacements will be distributed concentrically around the pumping well (Karasaki et al., 2000). If there are heterogeneities then the distribution of the volume will be different and the displacements will be skewed. The distribution of volume change is tightly coupled with the permeability and compressibility (Karasaki et al., 2000). This can be seen through the hydromechanical interactions are related to the fracture network geometry and the heterogeneity in both the fracture and the rock matrix (Cappa et al. 2005). This includes the mechanical connections with other fractures, and the orientation and magnitude of effective stresses imposed on fracture walls, and orientation or dip of the fractures (Capp et al. 2006; Svenson 2007).

A study by Urlaub and Fabian (2010) explained how tilting during pumping in sedimentary layers moved towards the higher permeability fault that was in the area. Svenson (2006) used axial displacement during pumping to characterize heterogeneities in the aquifer, such as crossing fractures and blockages. A study by Burbey et al. (2011) used extensometers and tilt meters during hydromechanical well tests to resolve the dipping direction of a fracture. The deformation of fractured rock may follow the same trend, and be helpful when interpreting well tests.

We can gain insight into 3D displacement monitoring of fractures during pumping by looking at these measurements in porous media under the same conditions. The causes of deformation magnitude and tilt direction during pumping in porous media have been summarized by Fabian and Kumpel (2003) using solutions of tilt during pumping in different geometries (Kumpel, 1989; Lehmann, 2001, Wang and Kumpel 2003; Burbey and Helm 1999). Important findings are that the total tilt amplitude is (a) proportional to

the pore pressure gradient caused during pumping, (b) a function of poroelastic rock parameter values, (c) depends on the location of the tilt sensors, pumping well, and pump, and (d) the dip direction of tilt is towards the pumping well in a homogeneous formation (Fabian and Kumpel 2003). Deviation from the dip direction towards the well could indicate lateral heterogeneity in the aquifer (Fabian and Kumpel 2003). Urlaub and Fabian (2010) modeled the effects that a less permeable fault 100 m east of a pumping well might have on tilt in the surrounding area. The comparative tilt directions are the same in cases where there is a fault and when there is no fault. The difference is that the tilt magnitude is greater on the side where the fault was located compared to the tilt on the opposite side of the pumping well. The study attributed this to the increased pressure gradient due to the fault.

Pumping tests with two tiltmeters at three sites were carried out by Fabian and Kumpel (2003) to determine if the analytical solutions could be verified in the field. The results were different from the analytical solutions, suggesting that the tilt signals are affected by heterogeneities. Reasons for the unexpected tilts were structural inhomogeneities, non-linear deformation process, Noordbergum effect, and anisotropic hydraulic diffusivity. These results give rise to more accurately detecting heterogeneities within fractured aquifers, which are commonly less uniform than porous media. By determining the lateral displacement of the fracture, heterogeneities could be identified and characterized. An example of this is during pumping when the pressure front interacts with a more permeable zone. What may happen is this zone will contribute more to the flow and deform in response to the volume changes. Based on the location of

this zone and the fracture being measured relative to one another, the fracture might transversely displace due to the volume change of the permeable zone.

APPLICATION FOR CO2 SEQUESTRATION

The technology described in the previous section would be useful during CO2 sequestration for the same reason that it is helpful to characterize aquifers during pumping tests. One of the challenges inherent to storing carbon dioxide is optimization of the methodology to demonstrate that storage in geologic formation is feasible i.e. that the formations have a large enough storage capacity and good injectivity for safe and long-term containment without adverse effects (Bachu 2000). Potential sequestration sites must be characterized to determine if the overlying cap rock will provide an effective seal, and if there is sufficient volume ofof permeable storage formation, and whether any abandoned or active wells will compromise the integrity of the seal (IPCC 2005). The technology needed to accomplish this must be capable of being deployed to depths greater than 1 km and be able to detect multi-dimensional deformation.

Previous and current extensometers used at Clemson implement electronic Differential Variable Reluctance Transducers (DVRT) to measure displacements. This technology has several problems that may make characterization difficult for sequestration wells. For example, they are vulnerable to electromagnetic interference and damage. The resolution can be impaired when the device is used in the same well as an AC pump, and DVRTs can be destroyed by lightning. DVRTs also require significant signal conditioning electronics in close proximity to the sensor. This requires specialized enclosures to armor the electronics from damage by water. These enclosures are bulky

14

and limit the size of boreholes where deployment can take place.   Furthermore, advanced applications for this technology in harsh conditions of elevated temperature and corrosive fluids (e.g. in wells used for CO_2 sequestration or oil production, for example) could challenge the functionality of the support electronics.

3D measurements would require many displacement sensors (as many as 10).The size of the sensor itself and the need for supporting electronics would place significant design constraints on the use of DVRTs for applications requiring many sensors.

A possible alternative displacement sensing technology is fiber bragg grating (FBG) sensors, which are connected to optical fibers. Fiber bragg sensors avoid many of the problems associated DVRTs. They are immune to electromagnetic interference or damage from lightning, and they can function in harsh conditions, such as corrosive fluids. They require no electronics in the well, so they can be compact and avoid the logistical difficulties encountered when armoring electronics. Review of the design specifications for FBG sensors indicate that they could provide the necessary resolution.

FBGs appear to offer an alternative to DVRTs for hydromechanical well testing, and indeed the technology has been used for this type of application (Cappa et al. 2006). However, considerable uncertainty remains over the feasibility of implementing FBGs in a 3D system.

OBJECTIVES

The objective of this work is to evaluate the feasibility of measuring three dimensional well bore displacements during hydromechanical well tests.

The approach to meeting the objective consists of the following tasks:

1. Develop and build an instrument capable of measuring deformation of rock enveloping wells in three dimensions

2. Calibrate the instrument in the lab, and evaluate its capabilities

3. Demonstrate the performance of the instrument during hydromechanical well tests

4. Evaluate and interpret 3D displacement data and pressure data from well tests

5. Evaluate the possibility of being able to deploy the device to depths greater than 1 km.

MOTIVATION

1. **Characterizing heterogeneities during CO2 sequestration:** Injecting fluid into a borehole elevates pressures that cause the wellbore to dilate radially and lengthen, while the adjacent confining units are compressed. Heterogeneities in the vicinity of the well will induce deformations that are non-radially symmetric, warping the bore into an ellipse or bending it sinuously. The loads are from the transient changes in fluid pressure, and their distribution is linked to the mechanical and fluid properties in the formation (Bai and Elsworth 2000). Measuring the wellbore deformation can be used to estimate the formation properties, and advance the design of an efficient and safe CO2 injection well (Murdoch 2010).

2. **Monitor CO2 sequestration process:** The high injection pressures needed for CO2 sequestration might cause hydraulic fractures, induce faults, deform seals,

break casing, and create other detrimental effects. Monitoring deformation in a well bore during injection could be used to prevent this (Murdoch 2010).

3. **Improve performance of hydromechanical well tests:** The transverse displacement data could provide insight into the distribution and magnitude of aquifer properties.

4. **Improving existing extensometer technology:** Current technology utilizes electronic transducers, which can be adversely affected by lightning, water, temperature. Th displacement signal can be affected by other electronic devices, and the components and wires can be bulky. For extensometers to be used during CO_2 sequestration they will be exposed to high pressures and temperatures, and will need to go down perhaps a few kilometers. It would be beneficial to analyze other sensor technology to be used when designing the 3D extensometer.

THESIS ORGANIZATION

Chapter One describes the design and laboratory evaluation of the extensometer. It will demonstrate that the device is able to detect 3D displacement and could be used for CO_2 sequestration.

Chapter Two describes the results during a series of hydromechanical well tests. It begins with a description of tests that were done in Japan, and it also includes results from tests at a well field in Clemson, SC.

2. EXTENSOMETER DESIGN AND CALIBRATION

Extensometers have been used to measure displacements during hydraulic well tests to better understand aquifer properties (Martin et al. 1990; Myer 1991; Thompson and Kozak 1991; Schweisinger and Murdoch 2002; Cornet et al. 2003; Cappa 2005; Cappa et al. 2005; Cappa et al. 2006). These instruments anchor to the borehole wall at two locations and use a high resolution displacement transducer or strain gauge to measure the movement of one anchor relative to the other. High resolution borehole extensometers have been under development at Clemson University for the past 10 years.

Hydromechanical well tests have been conducted at a handful of field sites in the U.S. and France (Burbey et al. 2012; Svenson 2008; Cappa et al. 2005). Insights into how aquifers behave and aquifer properties in a particular geologic setting have resulted from these tests. This includes estimates of fracture aperture, fracture normal stiffness, elastic modulus, fracture radius, fracture orientation, leakage, and blockage (Svenson 2007, Burbey et al. 2011). We have conducted hydromechanical well tests in metamorphic (Svenson et al. 2007; Schweisinger, 2008, Hisz et al. 2012) and sedimentary rock (Murdoch et al. 2009).

A multi-dimensional extensometer being used at Clemson currently is the Tilt-X 3DX. The Tilt-X is a combination of an extensometer and a tiltmeter. The tiltmeter is a Dual-axis Lily tiltmeter from Applied Geomechanics and the extensometer uses DVRT (differential variable reluctance transducer) to measure displacements. The Tilt-X consists of two pneumatically activated anchors (2-m spacing) separated by an invar reference rod (Hisz et al, 2012). The measurement range of the tilt meter is ±330 µrad,

18

and a noise level of less than ±30 nrad. The DVRT can resolve displacements of less than 0.01 μm.

DESIGN REQUIREMENTS

The design of the device is based on the objectives of developing a 3D extensometer that can eventually be deployed in a well-used for CO2 sequestration. The target displacement resolution is less than .01 μm, and total span should be more than 100 μm in both the axial and transverse direction. The device should have the capability of being deployed and removed from a borehole to depths of at least 3000 m, although the initial target depth for testing is 100 m. The device should be able to adjust and fit in boreholes with different diameters. It should be able to be transported easily, and be used in a test with minimum amount of equipment.

THREE DIMENSIONAL DISPLACEMENT

The design strategy for measuring displacement in three dimensions is achieved using two anchor points connected by a stiff rod with a flexure within the rod (Figure 1.1). The flexure can bend during transverse displacement, and it can extend or compress. When the two contact points move relative to each other the displacement is concentrated within the flexures. During axial displacement, the flexure compresses or extends when the anchors move relative to each other. When there is transverse displacement, one side of the flexure compresses while the other side extends. Three dimensional displacements can be determined by measuring the compressive or extensive displacement on each side of the flexure.

19
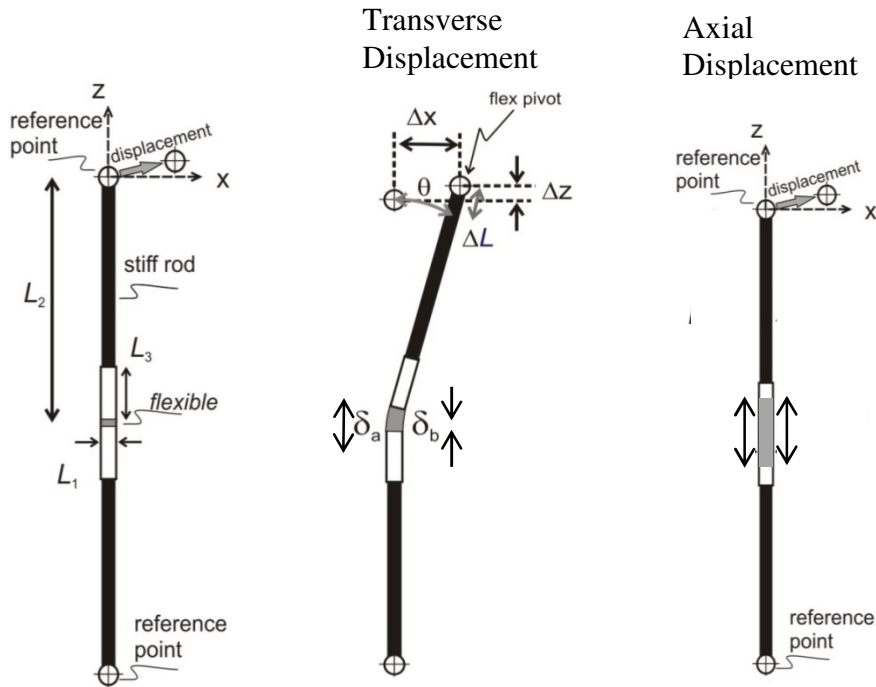
Figure 2.1: Conceptualization of how the two contact points on the device move relative to each other during 3D displacement (Murdoch et al., 2011).

PRINCIPAL COMPONENTS OF THE 3DX

The device used to measure 3D displacement for hydromechanical well tests is referred to as the *3DX* (Figure 2.2). It has seven main components: 1.) two anchors that grip the borehole; 2.) a strain bar where displacement will be localized; 3.) a frame used to move the device; 4.) centralizers to locate the device in the center of the borehole; 5.) fiber optic sensors used to measure displacement; 6.) a reference rod between the anchors; 7.) and an interrogator used to process the fiber optic signals.
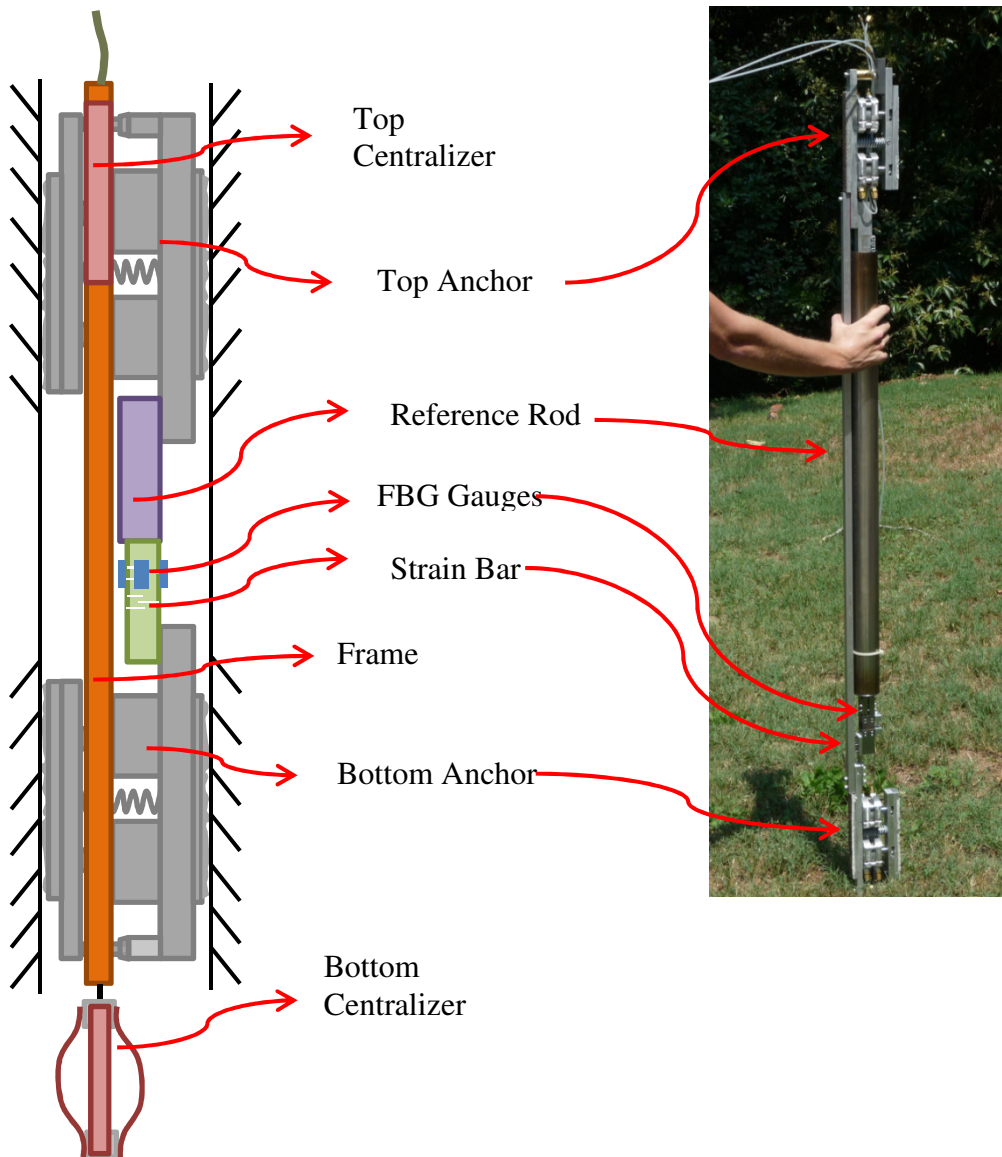
Figure 2.2: Conceptual diagram the 3DX, and an image of the actual 3DX.

Strain bar

The strain bar is designed to accommodate two types of displacement; bending

and extension.   The strain bar is a 15.2 x 2.5 cm stainless steel bar with six, transverse

parallel cuts that extend through approximately 80 percent of the thickness of the bar

(Figure 2.3).   Three cuts separate the bar into a pair of parallel plates joined to each

other along one edge and to the bar along the other. The plates are approximately 3 mm thick and 2 cm long, and they act as flexures that are much more compliant than the bar itself. Axial or bending forces applied to the bar primarily cause displacement of the flexures. One set of cuts is arranged to create flexures that are joined along two opposing sides of the bar. These flexures allow bending about an axis normal to the axis of the bar and parallel to joined edge of the flexures. Another set of cuts creates flexures that allow bending in the orthogonal direction. Axial displacements can be accommodated at both sets of flexures.
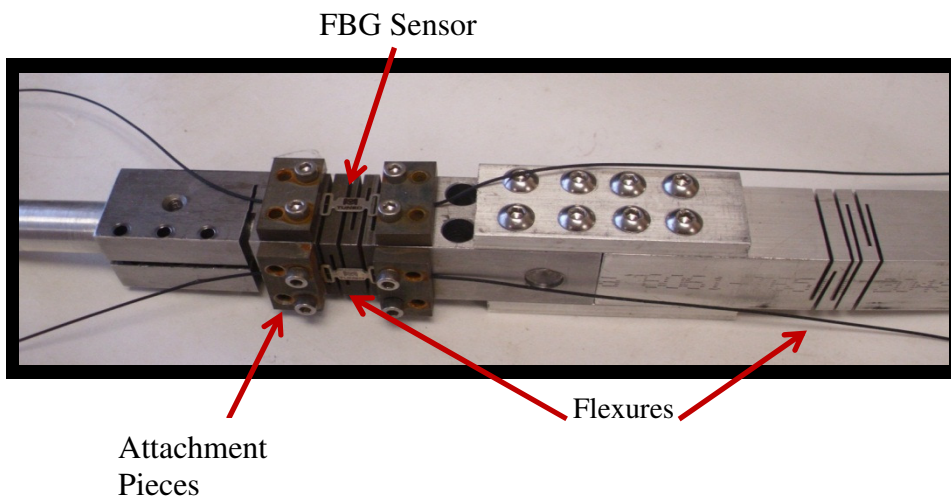
Figure 2.3: The strain bar used in the 3DX. The set of flexures on the right is where the gauges are secured by tightening the rectangular attachment pieces down holding the gauges in place.

The six cuts creating four flexures are spaced over 25 mm of the bar, concentrating displacement over that interval. The displacement is measured by four optical fiber strain gauges bolted on the surface of the bar. The strain gauges used in the device are thin stainless steel plates approximately 30 mm long, 10 mm wide and 1 mm

22

thick. An optical fiber with a Fiber Bragg Grating strain gauge extends along the axis of the gauge and is the active component. Two holes give the stainless steel body of the gauge compliance. The gauges are manufactured by Micron Optics and sold under the product name os3100 (Figure 2.4). The gauges are packaged with a one meter-long strand of fiber optic cable extending from either side of the steel body with FC/APC connecters at the end of each fiber optic strand. The connectors allow multiple gauges to be attached in series. FC/APC connectors can be linked together with an adaptor. The maximum number of gauges that can be connected to each other is limited by the number of Bragg wavelengths the interrogator can read on one channel.

Another option for connecting gauges is to splice them together. This method involves using a fusion splicer, which joins two optical fibers end to end using heat. Both methods have been used during this project, and both have advantages and disadvantages. The fusion splicer is beneficial for saving space, since the FC/APC connectors are bulky, and space must be considered when the borehole is only slightly larger than the device. The drawback of the fusion splice is that it is fragile and more vulnerable than the FC/APC connector to breakage. If the fiber optic cable were to break between two FP/APC connectors then another gauge can be inserted into the series. However, considerable fiber length is used to make a splice, so repeatedly repairing a splice will render a gauge unusable. The FP/APC connectors are stronger than the splices, but they are considerably more vulnerable to breakage than the cable itself.
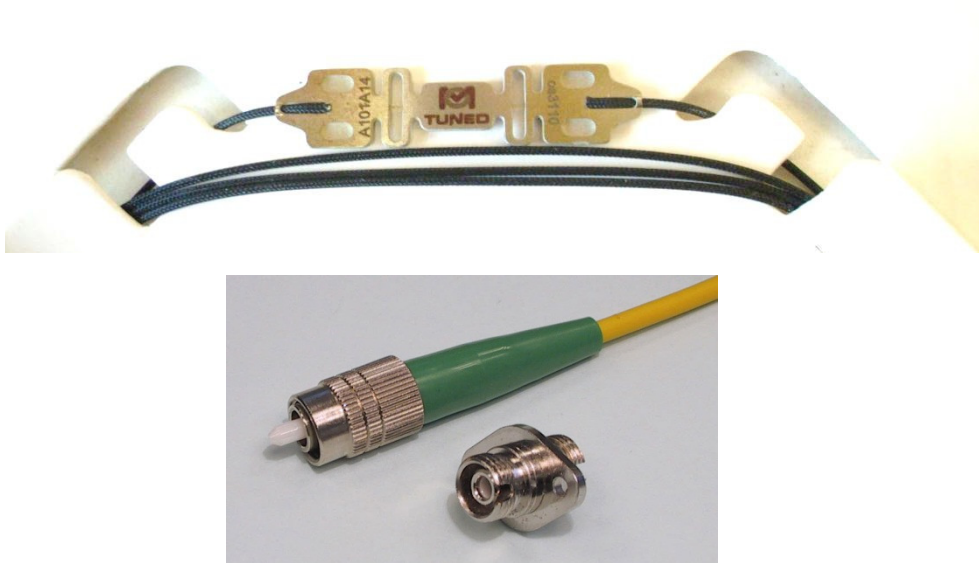
Figure 2.4: The top picture is the FBG sensor. The fiber optic cable is in the middle of the steel carrier which keeps the FBG etchings in tension. The bottom picture is the FP/APC connector and the adapter.

The strain gauges were place axially along the strain bar to span the compliant interval containing the cuts. The gauges were designed to be welded in place, but instead they were clamped them onto the strain bar using two 6-32 bolts and a stainless steel plate. This was an important feature because it allowed the delicate strain gauges to be decoupled from the strain bar when the instrument was moved, and then secured in place prior to deployment in the field. It also allowed the gauges to be removed and replaced when they were damaged.

There are two strain bars attached to each other axially on the 3DX. Two strain bars are necessary to accomplish the range of motion needed. The strain bar rotates during transverse displacement and this would be impossible if there was only one set of flexures. When there is transverse displacement the flexures compress on one side and extend on the other causing rotation (Figure 2.5). The difference in displacement of the

two opposing gauges gives the total transverse displacement of the strain bar with the equation

$$\delta_t = \frac{L_2}{L_1}(\delta_a - \delta_b)$$

(2.1)

where L_2 is the distance between the cuts and the end of the strain bar, L_1 is the width of the strain bar, and $\delta_{a,b}$ is the displacement of both gauges in line with the direction of displacement. The axial displacement is given by

$$\delta_A = \frac{(\delta_a + \delta_b + \delta_c + \delta_d)}{4}$$

(2.2)

where δ is the displacement of each gauge.
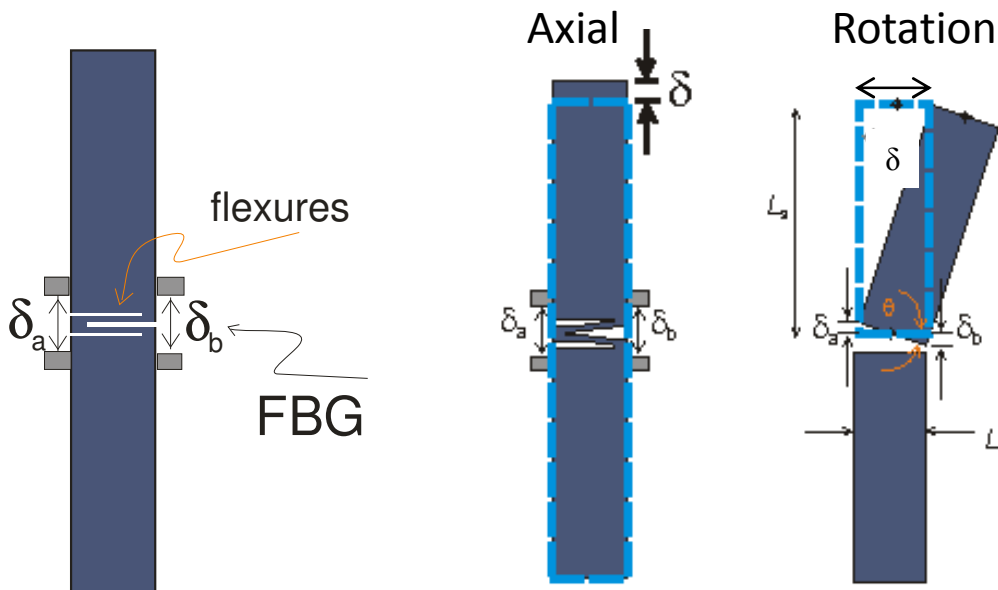
Figure 2.5: The conceptual model of how the strain bar moves during 3D deformation (Murdoch et al. 2011).

Fiber Optic Sensors

The sensor used to determine the strain uses a fiber Bragg grating (FBG), which acts as a wavelength-specific reflector. When light is injected into the fiber, the grating will either reflect or refract a specific wavelength defined by the spacing between the gratings and the effective refractive index of the grating in the optical fiber (Figure 2.6). Maximum reflectivity occurs at the Bragg wavelength given by:

$$\lambda_B = 2n_e\Delta$$

(2.3)

where λ_B is the Bragg wavelength, n_e is the effective refractive index of the grating in the fiber core, Δ is the grating spacing . The change of the reflected bragg wavelength is analogous to displacement based on

$$\frac{\Delta\lambda_B}{\lambda_B} = C_S \frac{\Delta L}{L} + C_T\Delta T$$

(2.4)

where C_S is the coefficient of strain, L is the length of the sensor, C_T is the coefficient of temperature, and T is the temperature. The displacement (ΔL) can be measured when the gauges are coupled with temperature gauges that compensate for the change in displacement caused by the temperature.

The reflected wavelength is called the Bragg wavelength (Grattan and Sun, 1999). When the sensor extends, the spacing between the grating increases and the reflected Bragg wavelength shifts towards a higher wavelength. The spacing between the etchings decreases when compression occurs, and the reflected wavelength decreases. . The

26

change in wavelength due to increasing or decreasing the spacing of the etchings is

proportional to displacement by rearranging eq. 2.4 (Schmidt-Hattenberger et al. 2003).
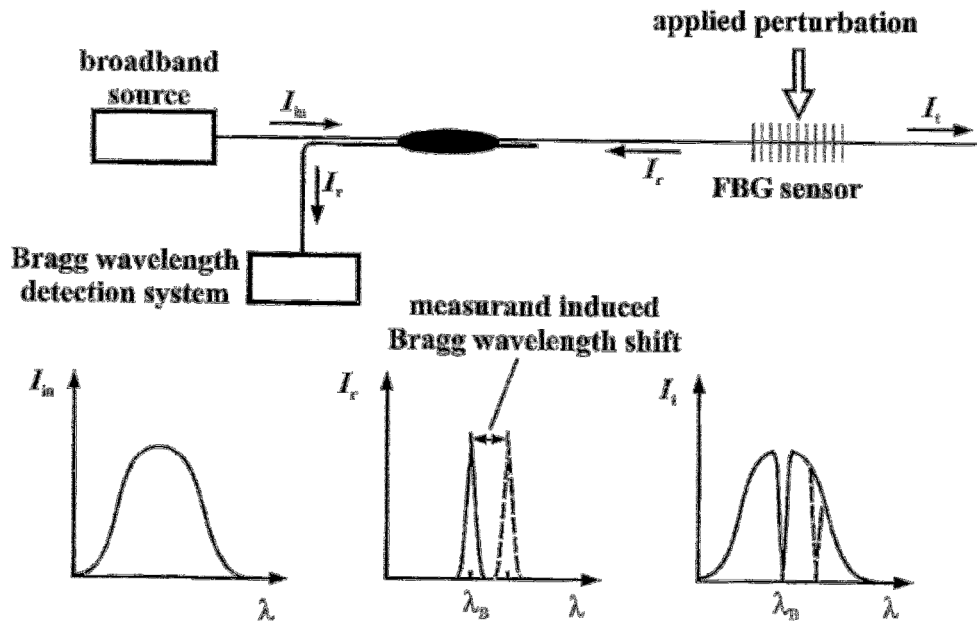
Figure 2.6: A schematic of how FBG gauges detect displacement. (Grattan and Sun, 1999).

<u>Interrogator</u>

The interrogator is the signal processing instrument used to send a broadband

light source through the fiber optic cable, and then detect the wavelength reflected by the

FBG. . The Micron Optics FBG gauges have been used with three different interrogators

during this work: Micron Optics sm125, FOS&S Spectraleye version 3.0.25, and Anritsu

AR4011A. The Spectraleye and Anritsu interrogators were used during the tests in

Japan, and the Micron Optics device was used during tests in Clemson, SC. Interrogators

have different specifications (i.e. size, scan frequency, number of optical channels,

wavelength range, etc.), so tests can be optimized based on the benefits of the different interrogators.

The Spectraleye is a hand held interrogator with a maximum scan frequency of 1 Hz (Figure 2.7). Instead of requiring a computer the interrogator attaches to a personal digital assistant (PDA). The interrogator has one channel, and has a wavelength range between 1530 and 1570 nm. The device can run off a battery for 90 minutes or from an external power supply. The benefit of this device is how compact it is, and does not require a computer in the field. It is also the least expensive of the three interrogators used.

The Anritsu interrogator has a maximum scan frequency of 1 KHz (Figure 2.8). It requires a computer, and needs an external power supply. The device has one channel. The wavelength range is between 1510 and 1590 nm. It is the most expensive of the three, and currently limited for sale only in Japan

The Micron Optics sm125 has a maximum scan frequency of 2Hz (Figure 2.9). The device has 4 channels and each channel can detect up to 10 gauges. The sm125 requires a laptop or PC, and requires an external power supply. It has a wavelength range between 1510 and 1590 nm (Figure 2.9).

Figure 2.7: The FOS&S Spectraleye interrogator

Anritsu
interrogator
program

Anritsu
AR4011A

Strain bar
with gauges
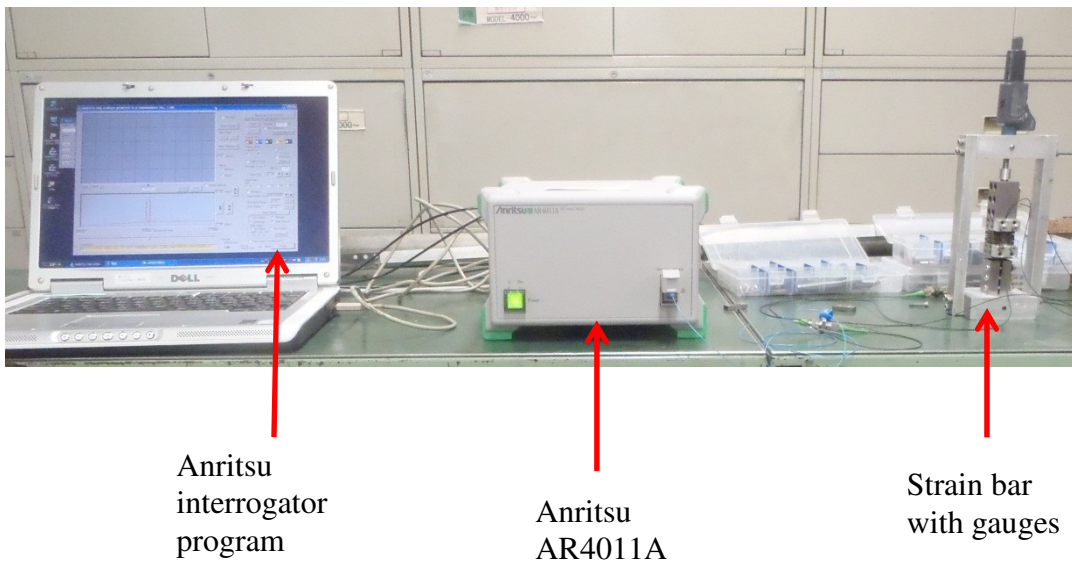
Figure 2.8: The Anritsu AR4011A set up
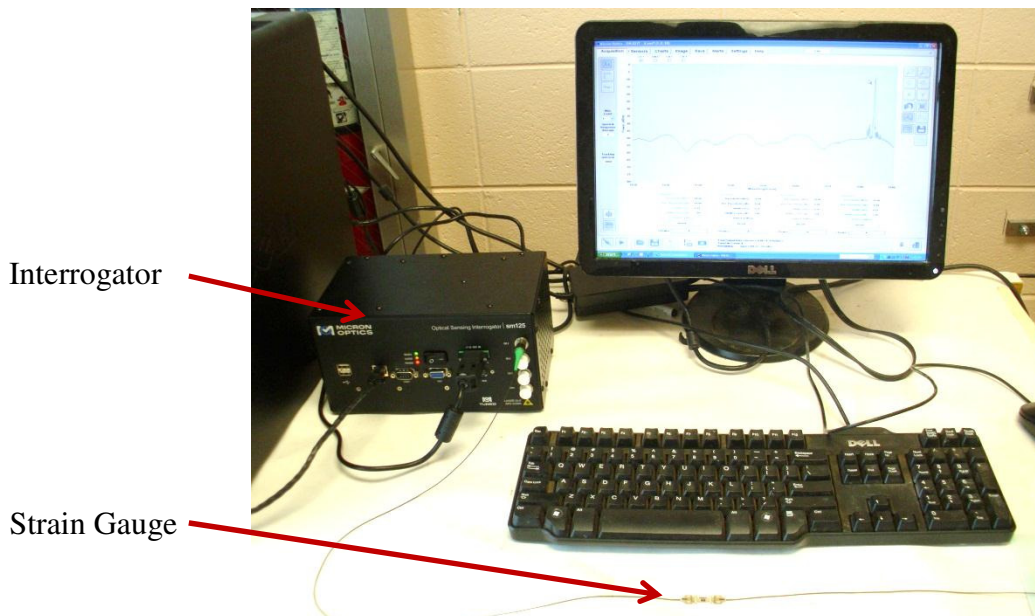
Figure 2.9: The Micron Optics sm125 interrogator

Anchors

There are two anchors located at each end of the 3DX that are responsible for securing the 3DX into borehole and holding the frame in place during deployment. During three dimensional displacements the anchors are the contact points with the borehole. The features of the anchors are two air cylinders, a spring, frame clamp, spacers, and carbide friction strips (Figure 2.10). The top bar of the anchor retracts when pressurized air is injected into the top of the air cylinder. The ability for the anchor to retract is necessary when deploying the 3DX to a specific location in the borehole. When air is released from the air cylinders the center spring extends the top bar, and applies a

constant force to the walls of the borehole (Figure 2.11).   The carbide strips increase the friction between the wall of the borehole and anchor preventing the 3DX from slipping.

The frame clamping mechanism is composed of a hollowed brass cylinder connected to the bottom bar, and a steel rod attached to the top bar of the anchor. The brass cylinder is conical at the top. When the anchors retract the steel rod is driven through the brass cylinder reducing the distance between the top anchor and the brass cylinder (Fig. 2.11).

The 3DX has the capability to be deployed in a wide range of borehole diameters. The top bar, where the carbide strips are attached, can be removed and spacers can be inserted between the sections. It also has interchangeable carbide pieces with different widths. Currently it has been deployed in holes ranging in diameter from 9 to 15 cm.
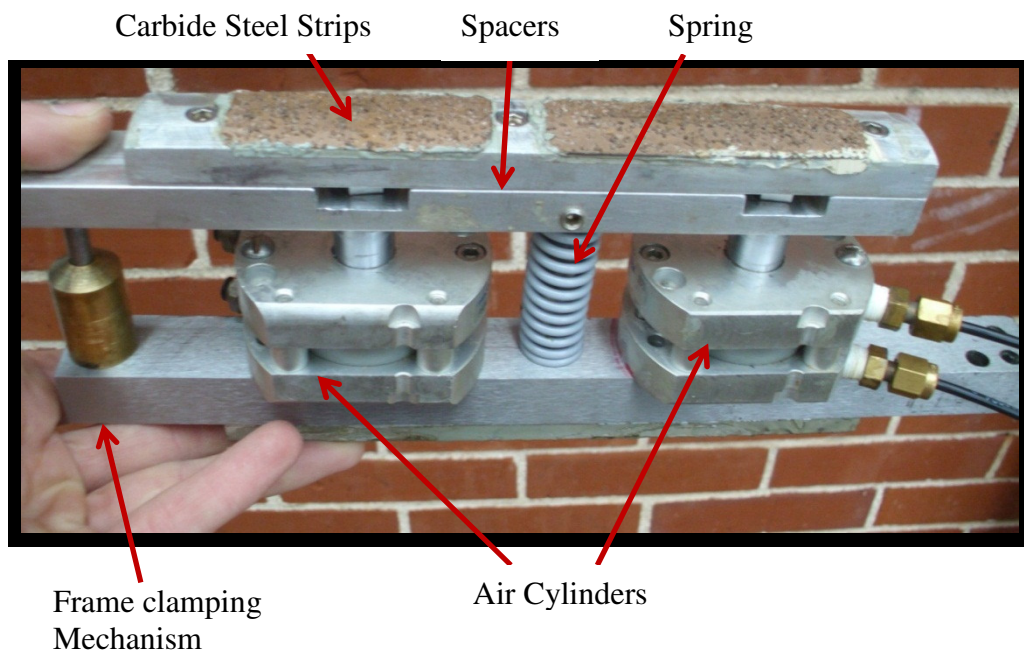
Figure 2.10: An anchor used in the 3DX. There are two air cylinders that can compress and extend the anchor, and there is a spring in between the air cylinders. Carbide steel strips are located on both sides of the anchor.
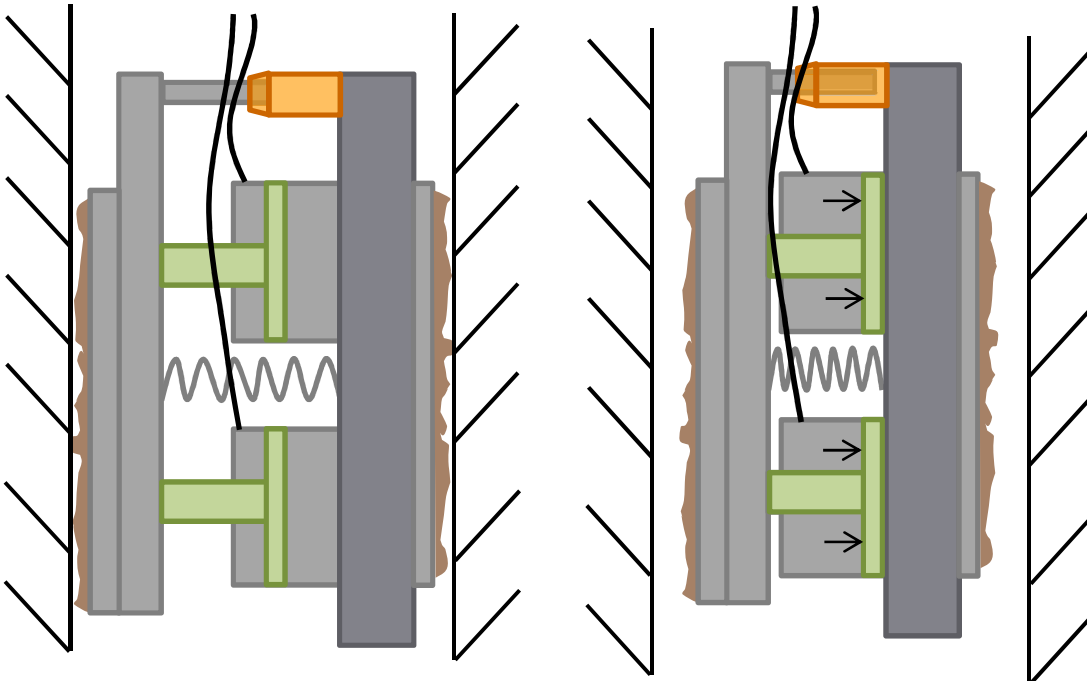
Figure 2.11: A sketch of the 3Dx anchor. The spring in the anchor extends the anchor and applies a force to the borehole walls. Pressurized air is used to overcome the spring force and retract anchors. The frame clamping mechanism drives the rod into the brass cylinder

Reference Rod

The reference rod increases the length of the 3DX, which makes it possible to concentrate more displacement between the anchors. The reference rod is a thin-walled steel tube that connects to the strain bar and one of the anchors (Figure 2.12). The reference rod has an outside diameter of 5.08 cm, an inside diameter of 4.915 cm, and a length of 1 meter

The reference rod should be much stiffer than the strain bar with the strain gauges attached in order to reduce the bending that would occur when the two anchors displace transversely relative to each other. The hollow reference rod was used to increase the

stiffness to weight ratio of the rod. A smaller weight is required to reduce the force on

the strain gauges during deployment.

Comparing the stiffness of different cylinders and the stiffness to weight ration

illustrates why a hollow cylinder was chosen (Table 1). If a 1 Kg weight is hung from

the end of three different cylinders with the same length, a solid cylinder with a radius of

0.635 cm has a lower stiffness and stiffness to weight ratio compared to the hollow

cylinder, and the weight of both rods is the same. The solid cylinder with the same radius

as the hollow cylinder is stiffer than the hollow cylinder, but due to its weight has

stiffness to weight ratio that is half of the hollow cylinder.

Description	Radius (m)	Stiffness (N/m)	Weight (Kg)	Stiffness/Weight (N/m*kg)
hollow cylinder	Outer:0.0254 Inner:0.024575	24867	1.01	23867
Solid cylinder	0.0254	196144	15.9	12327
Solid cylinder	0.00635	766	.99	770
Table 1: Stiffness comparison for different rod geometries				

Figure 2.12: The reference rod is a hollow cylinder with two end pieces used to attach to the top anchor and the top of the strain bar.

Frame

The frame consists of two aluminum bars approximately 183x2.5x.75 cm

(72x1x0.3 in) (Figure 2.13). There are 4 cross pieces that connect the two outer bars.

The frame is located along the entire length of the 3DX. The frame clamping mechanism

on the anchor goes through the cross pieces with the conical depression. The purpose of

the frame is to support the weight of the 3DX during deployment, and prevent the

anchors from moving relative to each other. Restricting the movement of the anchors

prevents the gauges from breaking during deployment. The retracted anchors hold the

frame in place through a frame clamping mechanism. During the deployment process the

anchors retract and the frame clamping mechanism repositions the frame so the cone of

the brass cylinder fits into the conical depression of the cross piece (Figure 2.14). The

anchors apply a force against the cross pieces and the weight of the 3DX is held by the

contact between the conical depression and the cone of the brass cylinder.

During deployment a rope or steel cable is attached to an eye bolt that screws onto

the top of the frame. The bottom of the frame is used to attach the bottom centralizer as

well.
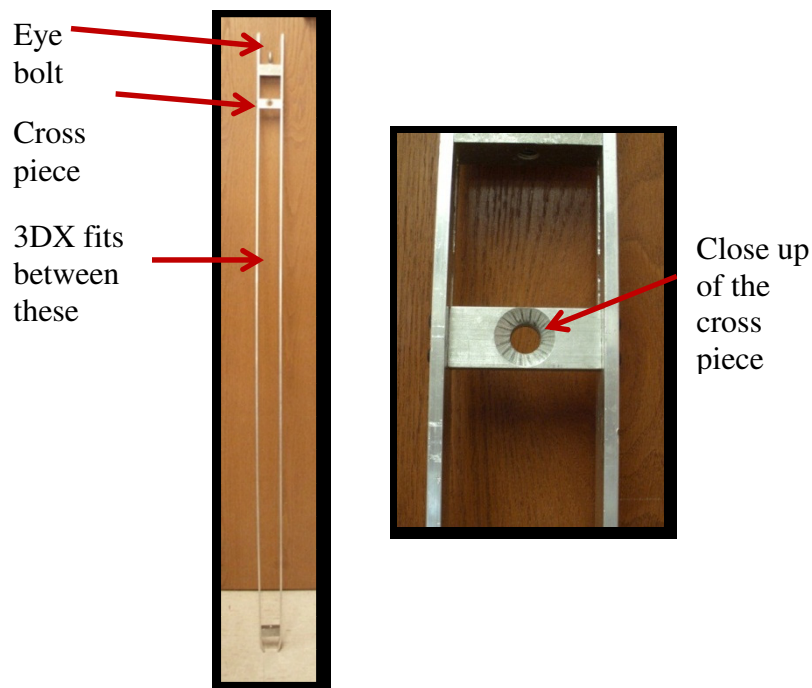
Figure 2.13: The frame is two aluminum bars attached by four cross pieces. The two
middle cross pieces have a conical depression that connects to the anchor through the
frame clamping mechanism. The top most cross piece holds the eye bolt, and the bottom
most cross piece holds the bottom centralizer.
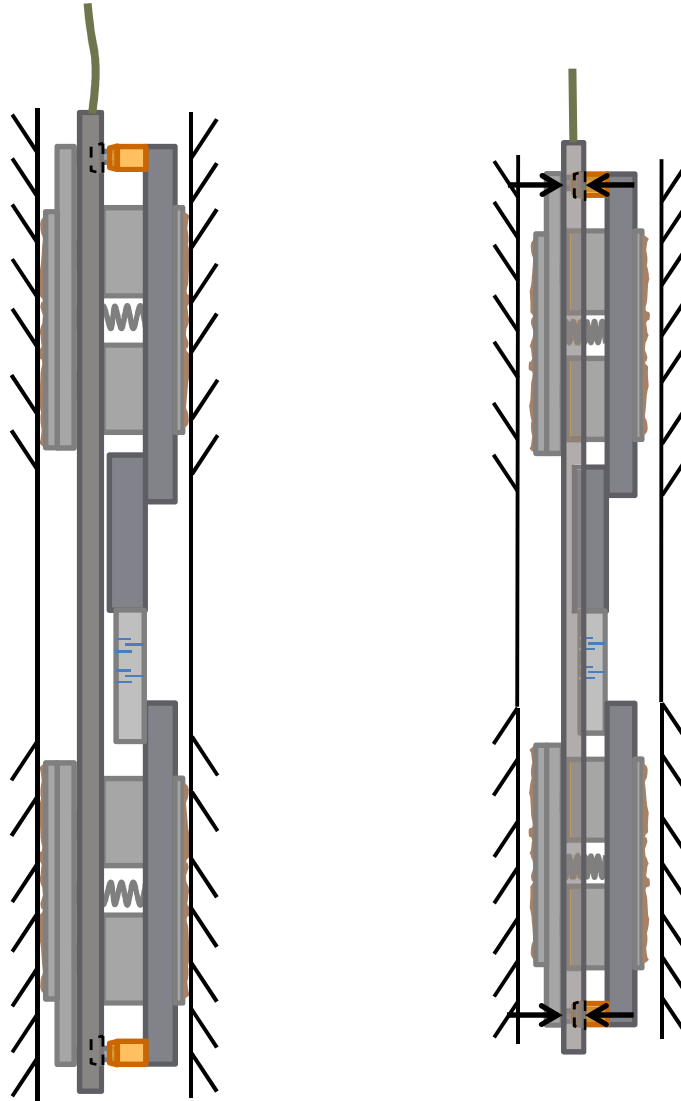
Figure 2.14: A conceptual model of the mechanics of the 3DX during deployment. When the anchors of the 3DX are extended the frame detaches from the frame clamping mechanism. When the anchors retract, the frame is positioned so the conical brass piece fits into the conical depression of the frame. During anchor retraction the weight of the 3DX is together by the frame, and it can be deployed or removed from the borehole

Centralizer

The centralizer centers the 3DX in the borehole during deployment. This prevents the anchors from being offset from each other when they are extended in the borehole, and it allows for easier deployment in a borehole with varying diameters. There are two sets of centralizers on the 3DX. This creates two points of contacts between the 3DX and the well bore preventing the 3DX from rotating. The locations of the centralizers are one on the top and another on the bottom. The bottom centralizer centers the 3DX in both the x and y plane, and the top centralizer only centers the 3DX in the x plane.

The bottom centralizer is made of four strips of spring steel that attach to a threaded rod (Figure 2.15). The top centralizer is two strips of spring steel that attach to the sides of the frame.

The centralizers are bow-shaped springs. The strips of metal composing the centralizer on the top and bottom can slide when pushed down on. With this design the centralizers can fit into a borehole with a smaller diameter than the length they bow out to, and allow for the 3DX to go down a hole.
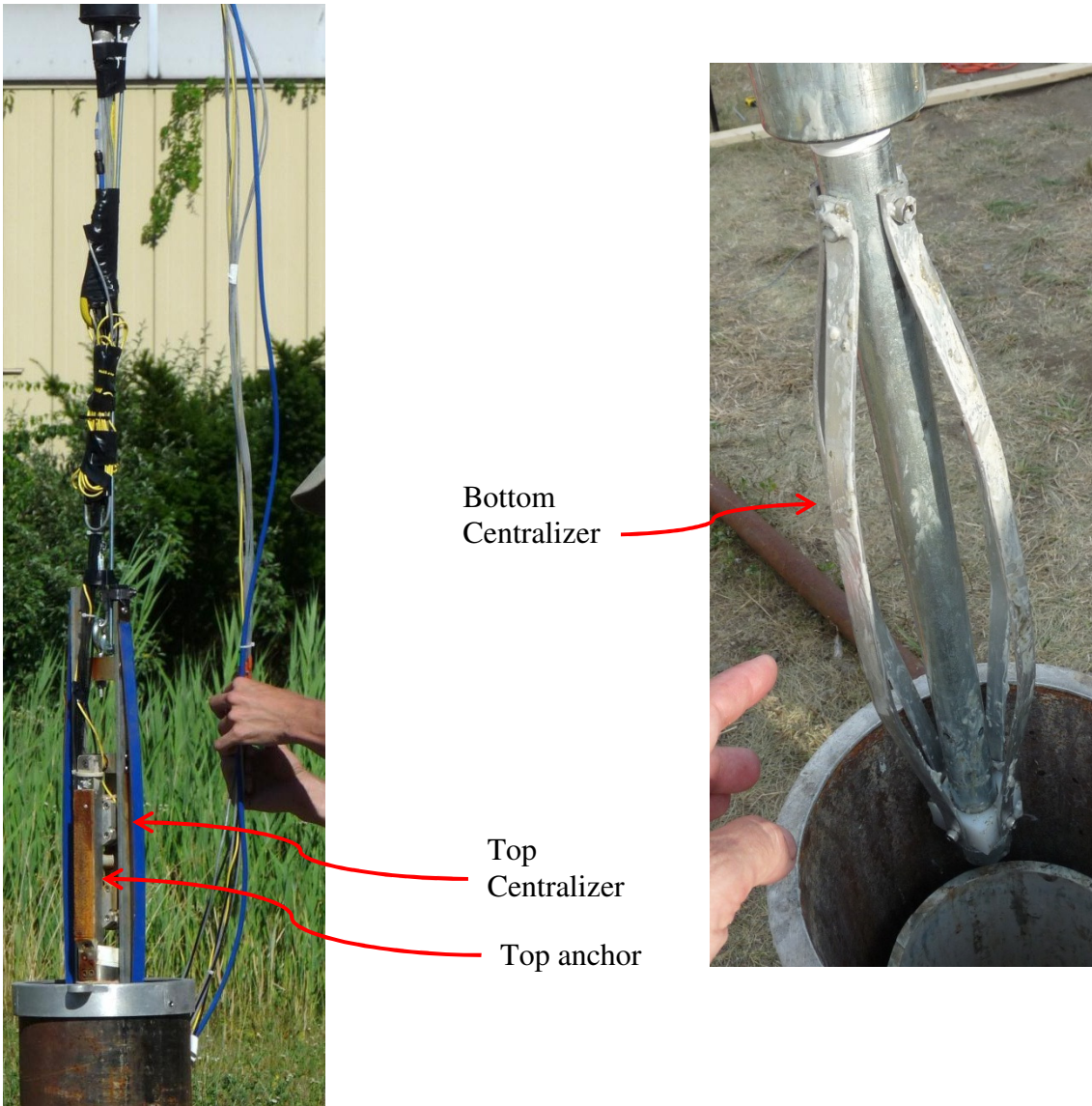
Figure 2.15: The right figure is the bottom centralizer located on another Clemson extensometer, and the left figure is the top centralizer on the 3DX.

CALIBRATION

Calibration involved determining the functionality of the 3DX in the laboratory.

This includes measuring the wavelength response to displacement axially and

transversely and the resolution of the FBG gauges.

Transverse Displacement Calibration

The transverse displacement calibration involved determining how the Bragg wavelength from the gauges changes when the top anchor displaces transversely relative to the bottom anchor. A calibration frame was developed that holds the 3DX vertically, securing the top and bottom anchor in place (Figure 2.16). Both anchors are extended in hollow aluminum cylinders. These cylinders are then supported by the calibration frame. The top cylinder is held in place by four threaded rods, two on one side and two on the opposing side of the cylinder. The threaded rods are tightened into the cylinder holding it in place. The top of the calibration frame contains micrometers on one side of the frame. The bottom cylinder is secured using hose clamps to the bottom calibration frame piece.

The method for calibration is to transversely displace the top anchor by a known amount while measuring the wavelength change using the interrogator (Figure 2.17 and Figure 2.18). Two threaded rods and two micrometers on one side of the cylinder are adjusted to translate the top anchor and prevent it from rotating. The top threaded rod is tightened approximately one quarter turn on one side followed by one quarter turn on the opposing rod. The resulting displacement is measured using the micrometer. The bottom threaded rod is turned approximately one quarter turn to achieve the same displacement. By displacing the bottom rod, the top one is also displaced so it is necessary to measure this and adjust accordingly. This step is repeated until both micrometers are the same. The displacement and wavelength are then recorded. This process is repeated until gauges approach their measuring threshold.

39
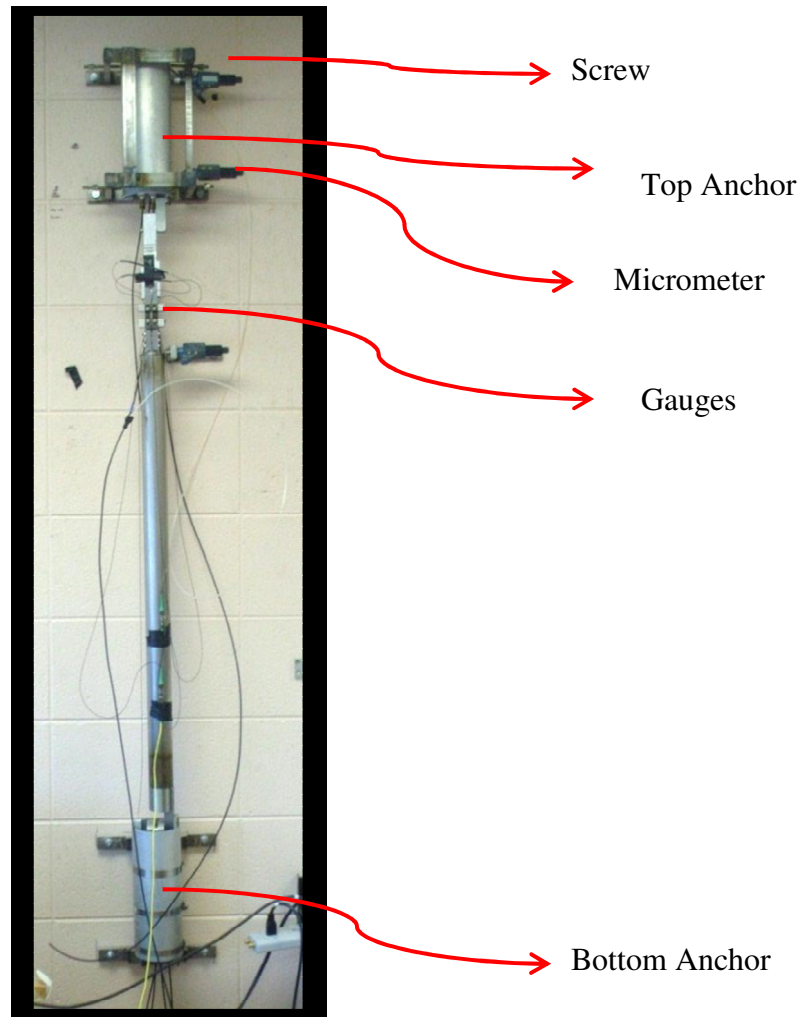
Figure 2.16: 3DX in the calibration frame used to transversely displace the top anchor.
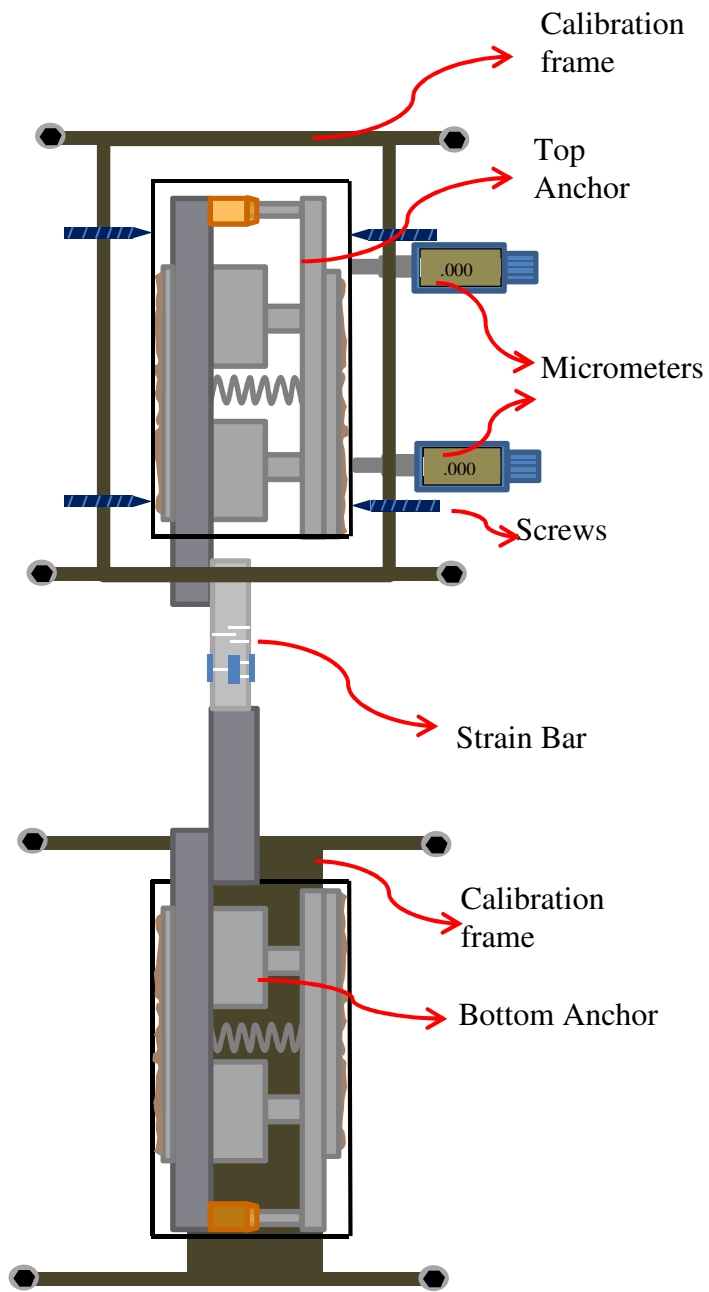
Figure 2.17: The 3DX in the calibration frame before the top anchor is transversely displaced by the screws.
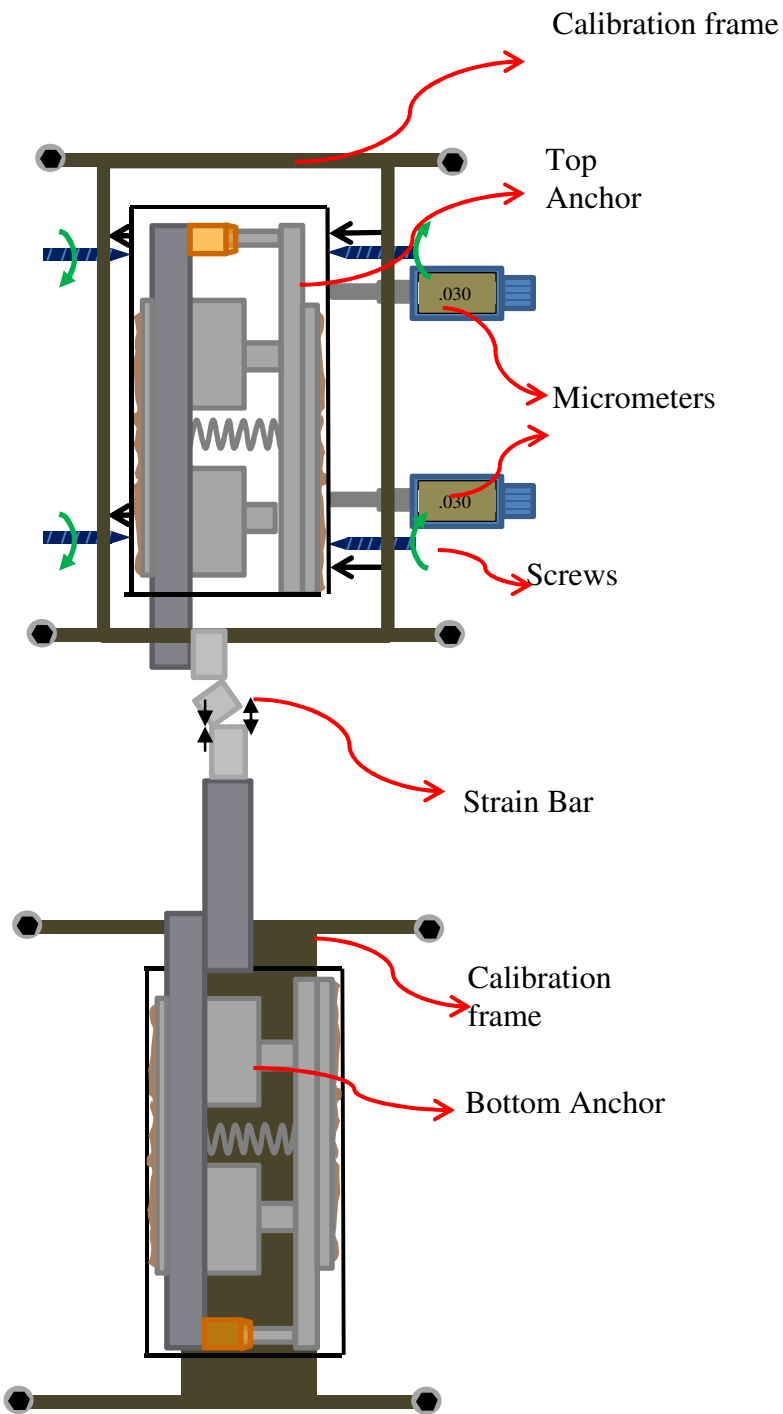
Figure 2.18: The 3DX in the calibration frame after the top anchor is transversely displaced by the screws.

During the test the two gauges parallel to the direction of motion reacted as expected. One of the gauges compressed while the other extended. The other two gauges perpendicular to the plane of motion displayed a Bragg wavelength that was relatively unchanged. Data from the test is plotted and the (Figure 2.18). The slope is

$$S_t = \frac{\delta_t}{\Delta\lambda_1 - \Delta\lambda_2}$$
(2.5)

where δ_t is the transverse displacement. The results from calibration tests gives $S_t=229$ µm/nm +/- 27 µm/nm (Fig. 2.19), where the uncertainty is the 95% confidence interval on the slope.

The transverse displacement can be calculated as a function of the wavelength shift to within a calibration constant, C_r, using the geometry of the strain bar

$$\delta_t = \frac{L_2}{L_1} C_g C_r (\Delta\lambda_1 - \Delta\lambda_2)$$
(2.6)

where L_2 is the distance between the cuts on the two strain bar 14 cm (5.58 in.), L_1 is the width of the strain bar 2.54 cm (1 in.), C_g is the gauge constant $15.71 \frac{\mu m}{nm}$ and is a specification given by Micron Optics, $\Delta\lambda_1$ is the wavelength change of gauge 1, $\Delta\lambda_2$ is the wavelength change of gauge 2. C_r is found by substituting Equation (2.6) into Equation (2.5).

$$C_r = \frac{S_t}{C_g} \frac{L_1}{L_2}$$

(2.6.1)

The result is that $C_r = 2.72 +/- 0.3$ using data for S_t in Figure 2.18.

The interpretation is that C_r is the ratio of the measured displacement to the displacement that would occur only due to the flexure of the strain bar. A value of 2.72 indicates that the observed displacement is 2.72 times greater than would be expected based on the strain bar alone. The additional displacement is interpreted to result from flexure of the reference rod.
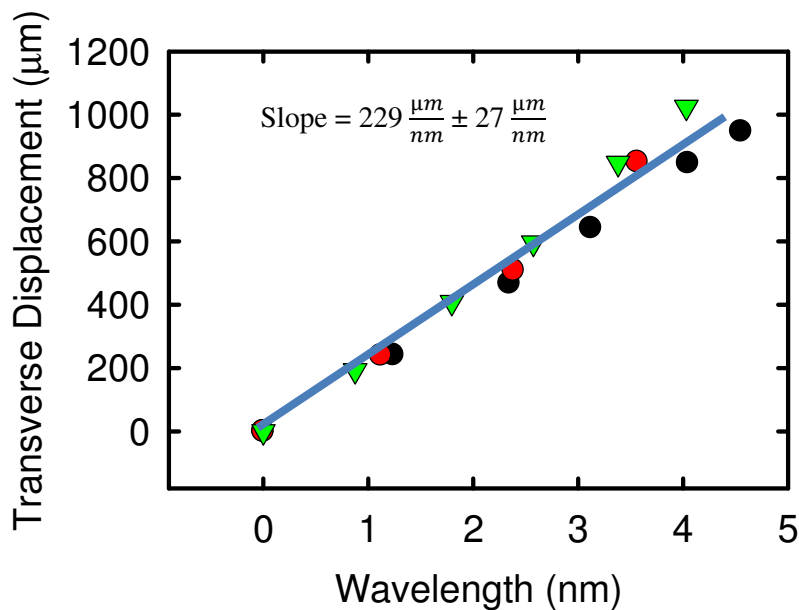
Figure 2.19: Transverse displacement measured by the micrometers as a function of the wavelength change ($\Delta\lambda_1$-$\Delta\lambda_2$) for three different tests. The black points is test 1, the red points is test 2, and the green points is test 3.

3DX Stiffness

The 3DX was modified based on the results of the transverse calibration test

(Figure 2.20). The reference rod constant of the initial 3DX design was approximately

C_r=13. This means that the components of the 3DX reduced the resolution by a factor of

13. The source of the problem was from the anchors, which were initially composed of

aluminum bars that were 1.25 x 2.5 cm thick. These were replaced with stainless steel

bars 1.9x2.5 cm thick. The reference rod constant from this was approximately $C_r = 4$,

and when the anchors were pressurized the reference rod constant was approximately $C_r =$

2.7. These results assume that the deformation of the testing frame could be ignored. It

is possible that some of the deformation attributed to the reference rod was associated

with the testing frame. The significance of this is that C_r would actually be less than 2.7.
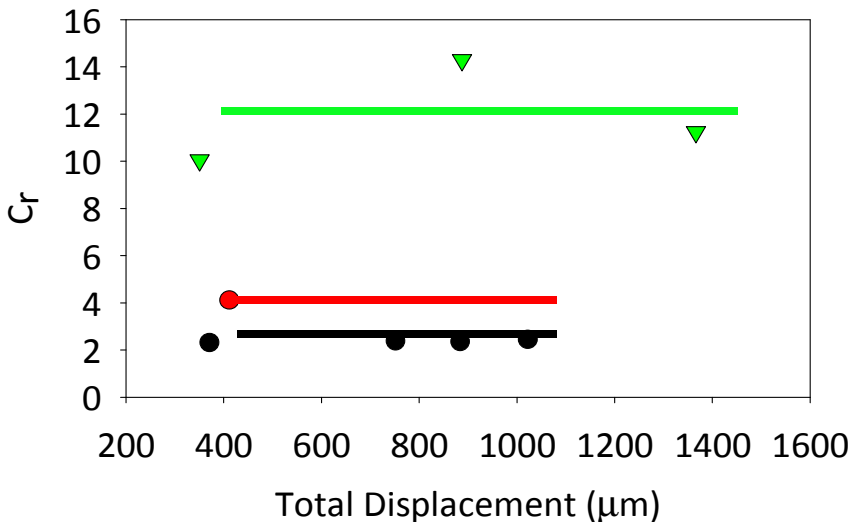
Figure 2.20: Reference rod constant, Cr as a function of total displacement for three
different designs. Aluminum anchor bar (green), stainless steel anchor bar (red) held
with springs, stainless steel anchor bar held with pressurized cylinders.

Axial Displacement Calibration

The axial displacement calibration involved determining how the Bragg wavelength from the gauges changes when the bottom anchor is axially extended relative to the top anchor. The same calibration frame used in the transverse test was used in the calibration test (Figure 2.21).

The method for determining the wavelength to axial displacement is to hang weights from the bottom anchor and measure the axial extension with a micrometer while measuring the wavelength change using the interrogator (Figure 2.22). The bottom anchor is detached from the bottom of the calibration frame and hangs freely.. This process is repeated until gauges approach their measuring threshold.
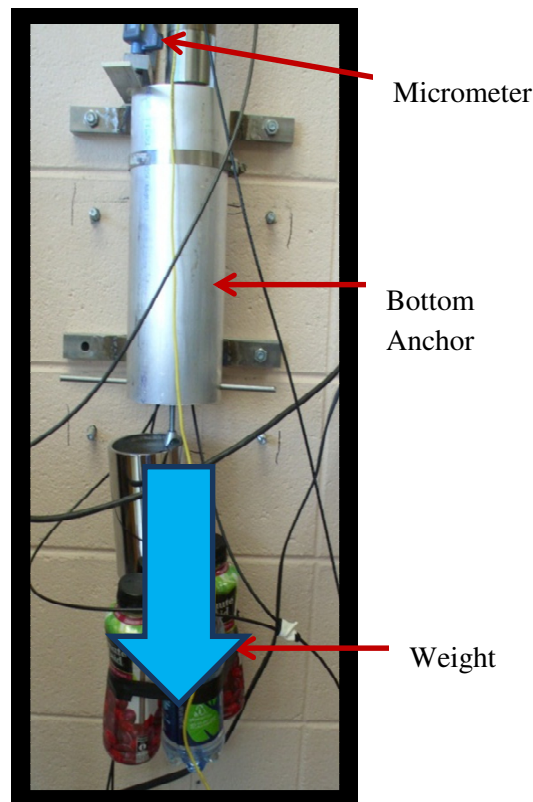
Figure 2.21: Picture of the 3DX in the calibration frame with the weights attached. The micrometer at the top of the figure measures the change in displacement.
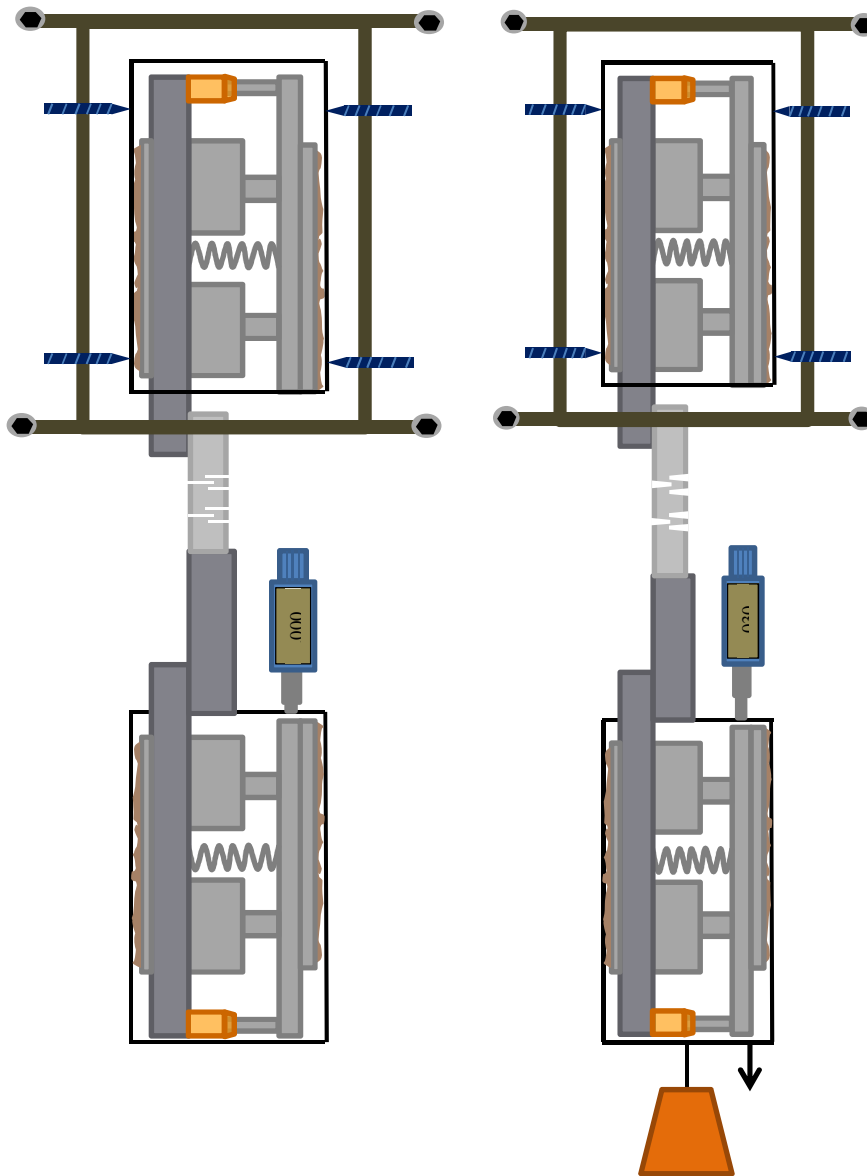
Figure 2.22: Idealized picture of the 3DX in the calibration frame during an axial test. The top anchor of the 3DX is secured in the calibration frame and the bottom anchor is left to hang. Weights are attached to the bottom anchor, and the displacement from the weight is measured.

The gauges responded similarly during the axial extension test, implying the total axial extension is the average displacement of the gauges. The purpose of the test is to plot the total axial displacement measured by the micrometers and the Bragg wavelength shift from the gauges during the displacement (Figure 2.23). The slope of the plot is used to determine the reference rod constant represented by C_A. The known values in the equation are: C_g is $15.71 \frac{\mu m}{nm}$, $\Delta \lambda_i$ is the wavelength change of gauge is

$$S_A = \frac{\delta_a}{\frac{\Delta \lambda_1 + \Delta \lambda_2 + \Delta \lambda_3 + \Delta \lambda_4}{4}}$$

(2.7)

where S_A is the slope from the axial calibration test, and δ_a is

$$\delta_a = C_g C_A \frac{\Delta \lambda_1 + \Delta \lambda_2 + \Delta \lambda_3 + \Delta \lambda_4}{4}$$

(2.8)

C_A is found by substituting in Equation (2.6) into Equation (2.5).

$$C_A = \frac{S_A}{C_g}$$

(2.9)

The result for C_A is 10.
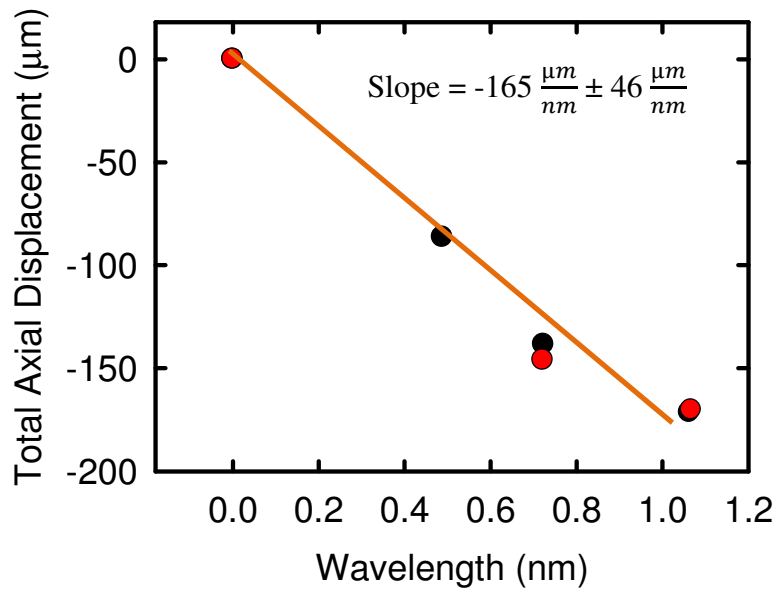
Figure 2.23: Axial displacement as a function of wavelength difference.

Combined Error Calculations

  The factors used to determine the transverse and axial displacement have error associated with them. In order to determine the displacement error, the error of each individual factor needs to be combined. When two values with errors are added or subtracted, the total error is (Baird 1962)

$$C = A + B \tag{3.4}$$

where A has error $\pm E_A$ and B has error $\pm E_B$. The error of C is found with

$$E_C = \sqrt{E_A{}^2 + E_B{}^2} \tag{3.5}$$

When two values with errors are multiplied or divided then the combined error is the

relative error. Consider

$$C = AB$$

(3.6)

The error of C is (Baird 1962)

$$E_C = C \sqrt{\left(\frac{E_A}{A}\right)^2 + \left(\frac{E_B}{B}\right)^2}$$

(3.7)

Transverse Error

The 3DX was calibrated to determine how the Bragg wavelength of the gauges

changed during transverse displacement. The result of the calibration is the reference rod

constant (C_r), which is used to determine the displacement when the 3DX is deployed.

The equation used to find C_r is

$$C_r = S_t \frac{L_1}{L_2} C_g$$

(3.8)

where L_2 is 14 ± 2.54 cm, S_t is the slope from the transverse calibration test. It is $229 \frac{\mu m}{nm}$

$\pm 29 \frac{\mu m}{nm}$. C_r will have error associated (C_{rerr}) with it from the other terms in Equation

3.8, so this error is found using

$$C_{rerr} = C_r \sqrt{\left(\frac{S_{terr}}{S_t}\right)^2 + \left(\frac{L_{2err}}{L_2}\right)^2}$$

(3.9)

50

from equation (3.11) C_{rerr} is ±0.485.

Now that C_{rerr} is known the relative transverse displacement error can be found. Recall that the equation to find transverse displacement is

$$\delta_T = \frac{L_2}{L_1} C_g C_r \left(\Delta\lambda_1 - \Delta\lambda_2 \right)$$

$$(3.10)$$

The first step is to find the actual error from finding the difference between the Bragg wavelengths. The error from the gauges is the 5 min RMS error of the Bragg Wavelength from the gauges.
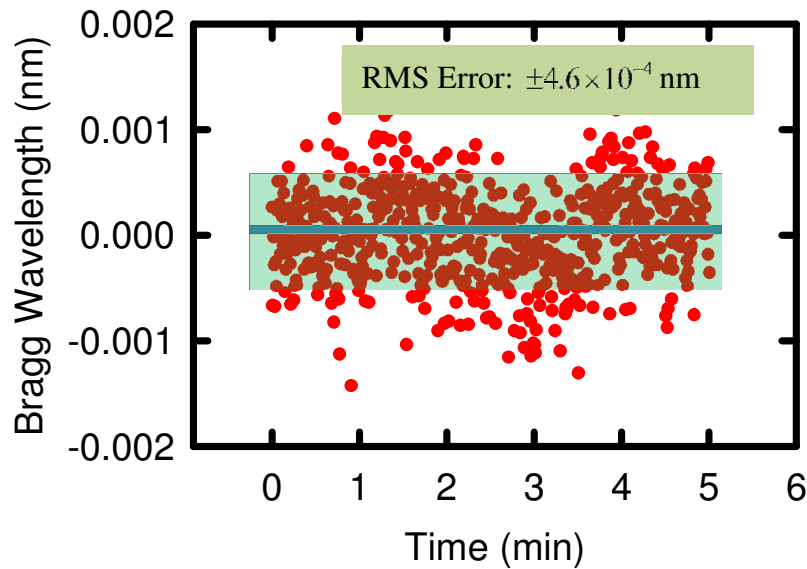
Figure 2.24: The residuals used to calculate the 5 min RMS noise for the gauges

The gauges have an error (λ_{ierr}) of ±4.6×10⁻⁴ nm (Figure 2.24). The actual error from the difference between the Bragg wavelengths of the gauges from Equation 3.10 is

$$\lambda_{err} = \sqrt{4(\lambda_{ierr})^2}$$

(3.11)

where λ_{err} is the actual gauge error, and λ_{ierr} is the individual bragg wavelength error.

so the transverse relative error (δ_{Terr}) is

$$\delta_{Terr} = \sqrt{\left(\frac{\lambda_{err}}{\lambda_i}\right)^2 + \left(\frac{C_{rerr}}{C_r}\right)^2 + \left(\frac{L_{2err}}{L_2}\right)^2}$$

(3.12)

where λ_{err} is the gauge error (0.00182 nm), λ_i is the bragg wavelength from the gauges (1550 nm), C_{rerr} is the rod constant error (0.485), C_r is the rod constant (2.72), L_{2err} is the error associated with establishing L_2 (2.54 cm), and L_2 is the length between the flexures (14 cm). Inserting these values into equation 3.13 yields a relative transverse displacement error of 30%. The magnitude of the transverse displacement error is from the error associated with the C_R constant and L_2. They each compose approximately 15% of the total error, and the gauge error is less than 1% of the total error.

Axial Error

The 3DX was calibrated to determine how the Bragg wavelength of the gauges changed during axial displacement. The result of the calibration is the axial constant (C_A), which is used to determine the displacement when the 3DX is deployed. The equation used to find C_A is

$$C_A = \frac{S_A}{C_g}$$

(3.13)

52

where S_A is the slope from the transverse calibration test. It is $165 \frac{\mu m}{nm} \pm 46 \frac{\mu m}{nm}$. C_A

will have error associated (C_{Aerr}) with it from the other terms in Equation 3.13, so this

error is found using

$$C_{Aerr} = C_A \sqrt{\left(\frac{S_{Aerr}}{S_A}\right)^2}$$

(3.14)

from equation (3.11) C_{Aerr} is ± 2.8.

Now that C_{Aerr} is known the relative transverse displacement error can be found.

Recall that the equation to find axial displacement is

$$\delta_a = C_g C_A \frac{\Delta\lambda_1 + \Delta\lambda_2 + \Delta\lambda_3 + \Delta\lambda_4}{4}$$

(3.15)

The first step is to find the actual error (λ_{err}) from finding the difference between the

Bragg wavelengths. The error from the gauges is the 5 min RMS error of the Bragg

wavelength from the gauges. The gauges have an error (λ_{ierr}) of $\pm 4.6 \times 10^{-4}$ nm (Figure

24). The actual error from the difference between the Bragg wavelengths of the gauges

from Equation 3.10 is

$$\lambda_{err} = \sqrt{8(\lambda_{ierr})^2}$$

(3.16)

where λ_{err} is the actual gauge error, and λ_{ierr} is the individual bragg wavelength error.

so the axial relative error (δ_{Aerr}) is

$$\delta_{Aerr} = \delta_A \sqrt{\left(\frac{\lambda_{err}}{\lambda_i}\right)^2 + \left(\frac{C_{Aerr}}{C_A}\right)^2}$$

(3.17)

where λ_{err} is the actual gauge error (0.00368 nm), λ_i is the bragg wavelength from the gauges (1550 nm), C_{Aerr} is the rod constant error (2.8), C_r is the axial constant (10), Inserting these values into equation 3.17 yields a relative transverse displacement error of 28%. The magnitude of the transverse displacement error is from the error associated with the C_A constant. It comprises approximately 27% of the total error. The error from the gauges is less than 1% of the total error.

Evaluation of Fiber Optic Strain gauges in Supercritical CO2

The 3DX could be used to monitor well casing deformation during injection of supercritical CO2. Monitoring the casing could be a preventative measure taken to avoid damaging the well. It could also be used to further characterize the storage capacity of the formation outside of the well. To evaluate the possibility of using the 3DX during CO2 injection we conducted a test to measure the effects of a supercritical CO2 environment on the strain gauges. It is possible that the supercritical CO2 could act as a solvent that deteriorates the glue used in the gauge.

During the test a strain gauge was inserted into a pressure vessel and filled with supercritical CO2 for the duration of one week (Figure 2.25). The vessel was pressurized to 200 bars and heated to 50 degrees Celsius.

To quantitatively determine how the supercritical CO_2 affects the strain gauges a bending test was done before and after it was subjected to the supercritical CO_2 (Figure 2.26). The bending test involves displacing one end of the strain bar by a known amount while the interrogator is measuring the wavelength change from the gauge. With this information we can compare the sensitivity of the gauges to displacement before and after the test. If the supercritical CO_2 affects the gauge then the displacement as a function of wavelength will be different before and after test. Another quantitative comparison test involved leaving the gauge alone for five minutes while the interrogator collected power level data. This information will be used to determine how the supercritical test affects signal strength. If the heat or CO_2 damages the fiber core then the signal strength will be different for both before and after.
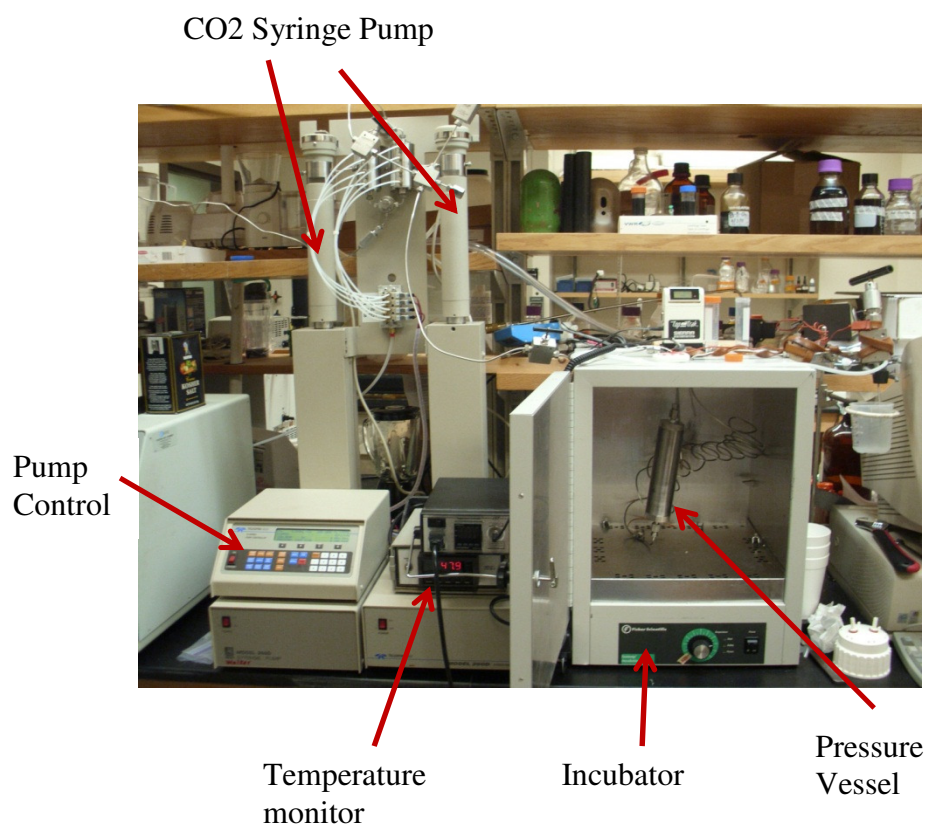
Figure 2.25: Apparatus used to test strain gauge in supercritical CO2, and two syringe pumps used to create and maintain a constant pressure.
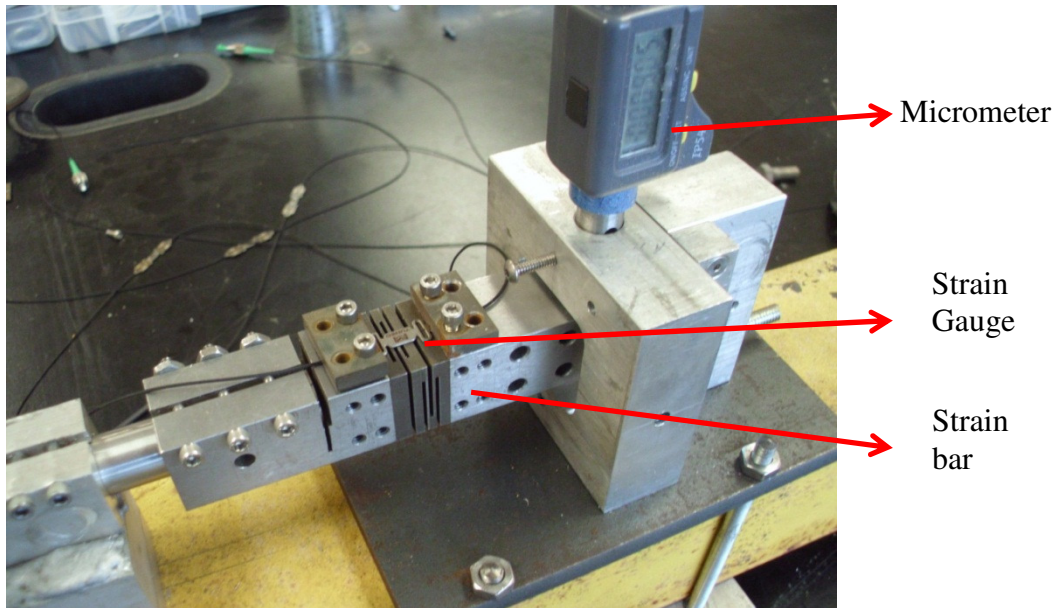
Figure 2.26: The transverse displacement test done to compare performance of the gauge before and after being exposed to supercritical CO2. The micrometer is used to push down on the strain bar. The gauge is secured to the strain bar and extends during the test.

Results

The results of the signal strength test were fit with a line to characterize their variability (Figure 2.27). The average value of the signal strength before the supercritical test was -10.98dBm and the average value of the signal strength after the test was -11.52dBm. The power units for these sensors are expressed by the ratio of decibels per one milliwatt. One milliwatt equals zero dBm, so if the signal strength decreases below this it becomes negative. The interrogator can detect peaks with a signal strength as low as -40 dBm, so a decrease of 0.54 has no effect on the performance.

The bending test results were fit with a line to determine the slope (Figure 2.28).

Both before and after tests have the same slope during the test of $-.012\frac{\mu m}{nm}$. The shift in

the plot is due to the induced strain caused by the attachment method used on the strain

bar. This does not affect the sensitivity of displacement as a function of wavelength.
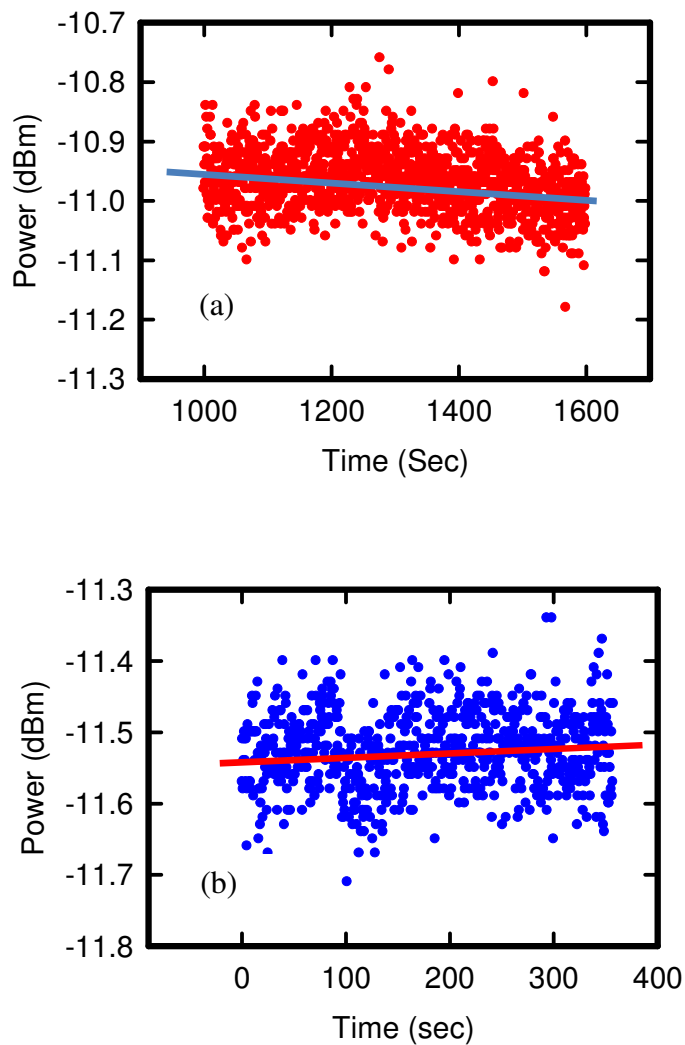
Figure 2.27: Power level of the signal as a function of time for (a) before the test and (b) after the test.
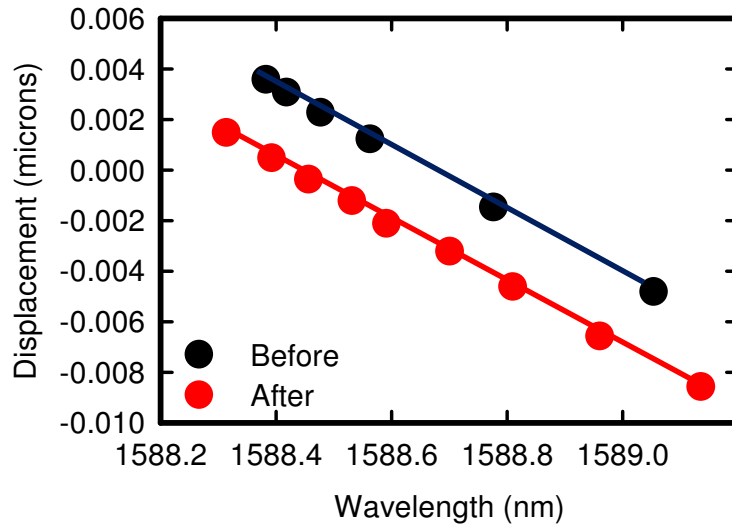
Figure 2.28: Displacement as a function of wavelength during a transverse displacement test. The black points are from before the test and the red points are from after the test.

Based on the comparison of the signal strength data and the transverse displacement test we conclude that the strain gauges we are using can function properly in a supercritical CO2 environment.

2 Hz RMS Noise of the Micron Optics sm125

The root mean squared of the noise for the 3DX will give the spread of the axial and transverse displacement around a linear trend line. This section focuses on the RMS for a frequency of 2 Hz. This is important because RMS noise will be different for different frequencies and averaging methods. Averaging decreases the RMS noise according to

$$R_{avg} = R \frac{1}{\sqrt{n}}$$

()

59

where *n* is the number of points averaged per amount of time (frequency), *R* is the RMS

noise without averaging. The RMS noise is calculated at 2 Hz because the field tests use

the Micron Optics sm125, which has a scan frequency of 2 Hz.

The data used to determine the 2 Hz RMS noise is from the 3DX when it was

deployed in a borehole at the Clemson well field at a depth of 24.3 meters. At this depth

the 3DX was straddling 2 fractures. The device was left to equilibrate for one day. After

it equilibrated, the device was left for five days while it collected Bragg wavelength

changes from the four gauges at a frequency of 2 Hz. The Bragg wavelength results were

then converted to axial and transverse displacement using Equation (2.6) and Equation

(2.8) respectively. Five minutes of data was used to characterize the 2 Hz RMS by fitting

with a regression line. The linear trend accounts for longer term variability, such as that

caused by temperature or deformation in the well bore. Then the residuals are found

$$residuals = y_p - y_a \tag{2.9}$$

The fitted regression line and the residuals were found using the software package,

TableCurve.

The RMS noise is found using (Baird 1962)

$$RMSError = \sqrt{\frac{\sum_{i=1}^{n}(residuals_i)^2}{n}} \tag{2.10}$$

Transverse Displacement

 The 3DX can measure transverse displacement in two planes, so the RMS noise

of both planes can be calculated and compared. Using the method described above the

RMS noise of the transverse displacement for both planes is ±188 nm and ±193 nm

(Figure 2.29).
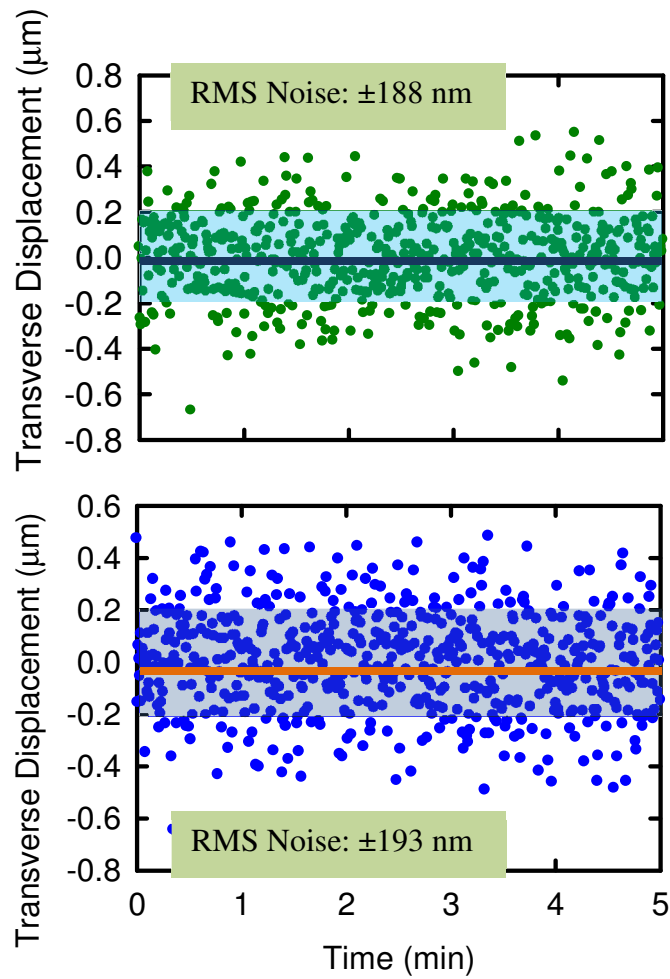
Figure 2.29: The residuals used to calculate the 5 min RMS noise for transverse
displacement in both planes

Axial Displacement

Using the method described above the RMS noise of the axial displacement is ±31 nm (Figure 2.30).
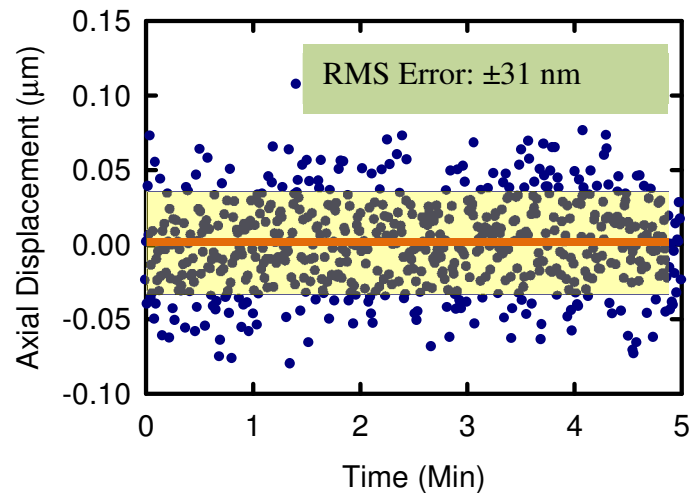
Figure 2.30: The residuals used to calculate the 5 min RMS noise for axial displacement

1 kHz RMS noise of Anritsu AR4011A

Evaluating the RMS noise of the Anritsu Interrogator from field measurements, and comparing it to the RMS noise of the Micron Optics sm125 illustrates the resolution improvement from two different scan frequencies. To obtain this data, the 3DX was deployed in a well bore in Japan. The interrogator used to measure the Bragg wavelength of the four gauges attached to the 3DX was the Anritsu AR4011A. The signal used for the analysis had an associated drift to it. The drift may be due to temperature changes, presumably. The signal from the Micron optics interrogator did not have a noticeable drift. This may be due to equilibration times. The 3DX had more time to equilibrate for the signal used for the Micron optics analysis as compared to the Anritsu signal.

The Anritsu Interrogator obtains data at 1 kHz and performs a 1 kHz forward average of the data internally, where each displacement value is the average of the 1000 forward displacement values (Figure 2.31). The 5 min 1 kHz RMS noise for the axial displacement is 19.8 nm, which is two thirds the noise when using the Micron Optics interrogator (Figure 2.31). The 5 min 1 kHz RMS for the transverse displacement is 64 nm, which is one third of the noise when using the Micron Optics interrogator.
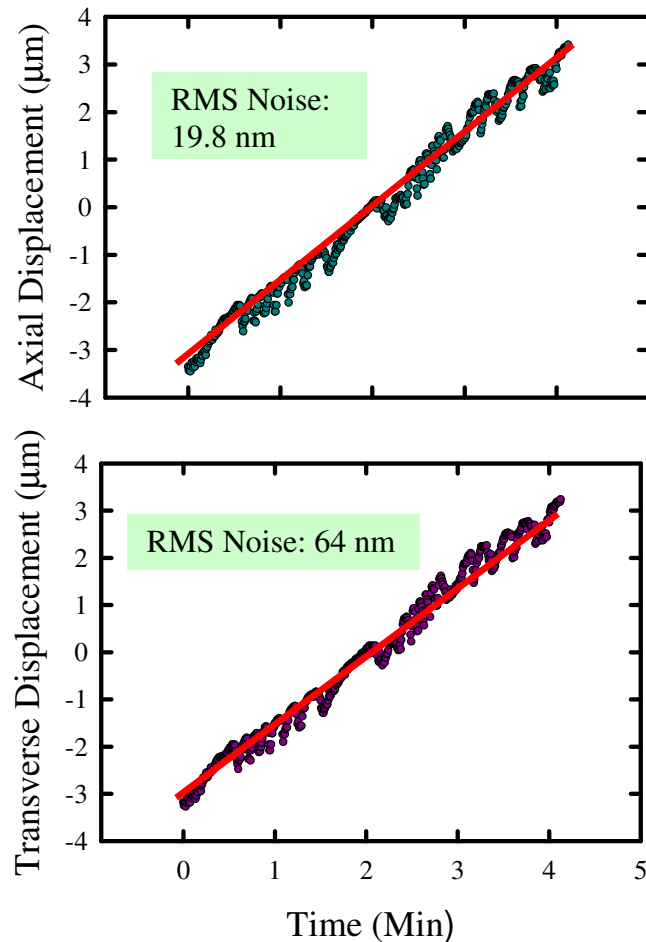
Figure 2.31: Displacement as a function of time using the Anritsu AR4011A. Data fit with a line and used to calculate 1KHz 5 min RMS noise of the Anritsu AR4011A.

CHAPTER DISCUSSION AND SUMMARY

The design of the 3DX is based on previous extensometers used at Clemson, but it has been modified to include fiber optic sensors. It includes two anchors separated by a reference rod and two strain bars. The dual anchor separated by a reference rod has been implemented in other extensometers, so we are confident in the performance of these components. When the anchors are secured against the walls of the borehole, the two strain bars can extend, compress, and rotate allowing the anchors to move relative to each other. This motion can be resolved by knowing the compressive and extensive displacement on each side of the strain bar. The strain bar compression or extension can be determined by attaching a FBG gauges to each of the four sides of the strain bar.

Each gauge reflects a Bragg wavelength and the shift in the Bragg wavelength is proportional to the compression and extension of the strain gauge. The conceptualization of detecting axial displacement is that as the anchors move towards each other axially, the induced displacement is concentrated within the strain bar flexure. The four gauges will compress, so the axial displacement is calculated by taking the average change in wavelength of the four gauges. The conceptualization for measuring transverse displacement is as the anchors displace transversely relative to each other, the strain bar bends. The two gauges in the plane of the transverse displacement react; one compresses and the other extends. The transverse displacement is determined by calculating the difference in the wavelength change of the two gauges.

Calibration

The calibration tests show how the 3DX can measure 3D displacements. The methodology of the tests was to suspend the 3DX vertically, and displace the top anchor

relative to the bottom anchor in three dimensions. The gauges are attached to the strain bar, and the displacement of the anchors is measured as a function of the Bragg wavelength. The results of the test suggest that the 3DX can detect axial and transverse displacement. We confirmed that the transverse and axial displacement of the anchors can be measured by coupling a geometrical analysis with the gauge measurements. During transverse displacement the two gauges facing the direction motion acted equally but opposite; one compressed and one extended. The strain bar extended during the axial displacement test. This in turn extended all the gauges. The average displacement of all the gauges is the axial displacement.

The compressibility of fractured rock aquifer is approximately 1 micron per meter head axially, and from previous tests 10s of microns transversely. The 2 Hz RMS noise of the 3DX should be at least an order of magnitude less than these signals. For axial displacement the resolution was found to be 31 nm and the transverse resolution was 190 nm. This is within the bounds needed to detect the three dimensional displacements that might occur during a hydromechanical well test.

RMS noise

We found that the RMS noise of the 3DX is within the limits needed to detect 3D displacement during hydromechanical well tests. The RMS noise of the 3DX can be improved by modifications to the device, interrogators, or fiber optic gauges.

The strain gauges are composed of steel carriers that resist displacement. Removing the steel carriers has the possibility to reduce the RMS noise of the 3DX. The drawback of this is that the strain bar would need to be redesigned to protect the gauges

during deployment. There would need to be a system that would allow the user to attach the gauges when the 3DX is in the borehole.

The stiffer the reference rod the less it will move during transverse displacement. This can be done by increasing the wall thickness or its total diameter. The resolution improvement from this effect might be offset by an increase in weight, which could increase the chances of damaging the gauges.

The strain bar can be modified by increasing the compliance of the flexure that the gauges attach to, and decreasing the compliance of the second flexure. This will concentrate more of the displacement on the gauges.

The anchors can be modified by using a stiffer spring. The resolution of the 3DX was improved by pressurizing the air cylinders during calibration tests. This occurred because it increased the force on the anchors. The gauges are sensitive to small changes in pressure in the cylinders, so using a stiffer spring is preferred to pressurizing the cylinders.

3. FIELD APPLICATION

The chapter includes the description of the field sites and wells where the 3DX was deployed during hydromechanical well testing in Tsukuba, Japan, Clemson, SC, and Trenton, NJ. The methodology and materials for the tests, and the results from the wells tests and ambient monitoring are also included.

PROOF OF CONCEPT: TSUKUBA, JAPAN

A 3DX prototype was deployed at a site in Japan, where it was used for initial development and proof of concept.   .

Tsukuba, Japan Field Site

The field site is located in an abandoned granite quarry near Tsukuba, Japan at the base of Tskuba Mountain (Figure 3.1). The granite is fractured between the surface and 20 meters depth, with decreasing fracture density below this. The water table is approximately 2 meters below the surface. A hydromechanical well test was performed in borehole 3 at a depth of 10.5 meters (Figure 3.2). The 3DX was straddling multiple fractures at this location. The borehole is cased down to 3 meters, and the borehole diameter is 95 mm.
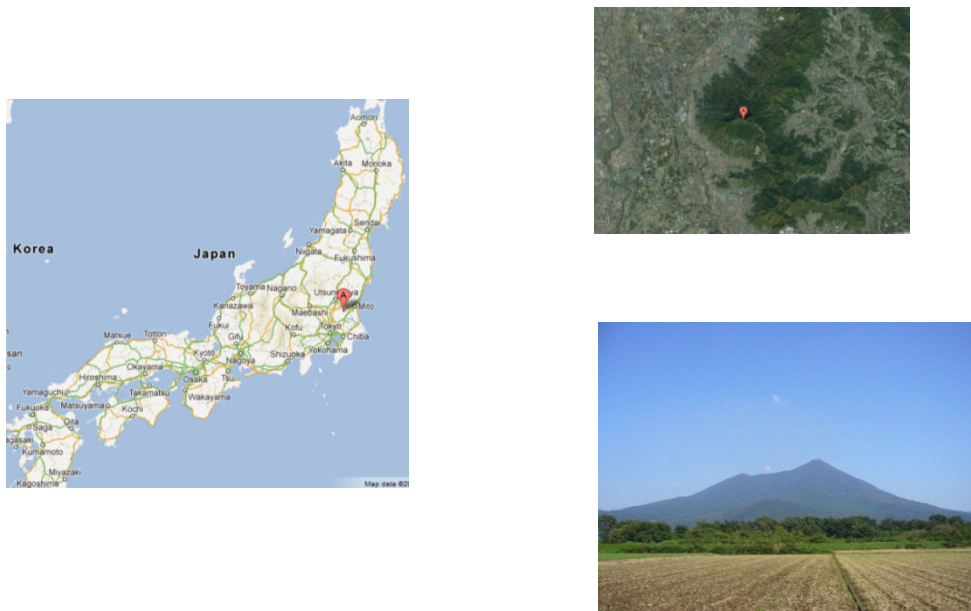
Figure 3.1: Location of field site in Tsukuba, Japan. The field site was located at the base of Tsukuba Mountain (bottom right).
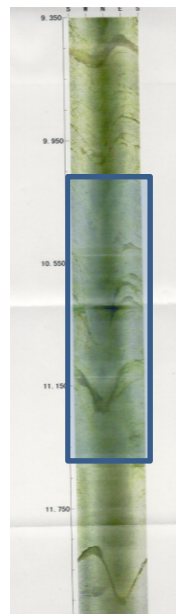
Figure 3.2: The section of borehole straddled by the 3DX during the well tests in Tskuba, Japan.

Test

The procedure to carry out a hydromechanical well test is to first deploy the 3DX. The device is hung from a tripod and the FBG gauges are secured. The locations of the gauges are then recorded relative to the top of the 3DX. A pressure transducer is attached to the bottom of the frame. At this point the top anchor is retracted and the bottom anchor is expanded. When the gauges are set the bottom anchor is retracted, and it is lowered to a predefined depth. The 3DX is lowered past the desired depth and then pulled back up to prevent offset in the anchors. The air pressure used to retract the anchors is 60 psi. The procedure to set the anchors is to extend the bottom anchor and then extend the top anchor in sequence.

After the 3DX was deployed, water was pumped from the borehole at a varying rate. This rate decreased with time. The water level was measured with water level tape and the pressure transducer. During pumping the interrogator is recording the Bragg wavelength from the active gauges on the 3DX.

A total of five field tests were conducted, with modifications in the equipment and procedures made after each test. An unknown factor was how long the device needed to equilibrate with the borehole surroundings, so the time between deployment and the start of the hydraulic well test varied. The differences in equilibration times were between an hour and approximately half a day. The first two tests had only one active gauge, the next two tests had two active gauges opposite of each other, and the fifth test had all four gauges attached to the strain bar. The fifth test was in a different borehole then the first four tests.

Results

The most insightful results occurred during the fifth test. The 3DX was left in the borehole overnight, which allowed it to equilibrate with the surroundings. First a slug was inserted into the borehole, which raised the head by a meter and expanded the fracture by about 0.2 microns (Figure 3.3). After this the head was dropped four meters during pumping and 0.8 microns of compression occurred (Fig. 3.3). The experiment ran until the aquifer recovered and the displacement returned to its initial value.

Test 5 showed a compression of 1 micron during a head drop of 5.5 meters (Figure 3.4). This was found by averaging the displacement of the four gauges. The transverse displacement was determined using Equation 2.6. This resulted in 12 microns across gauges A3 and A4, and less than 1 micron of transverse displacement occurred across gauges A1 and A2 (Figure 3.5).
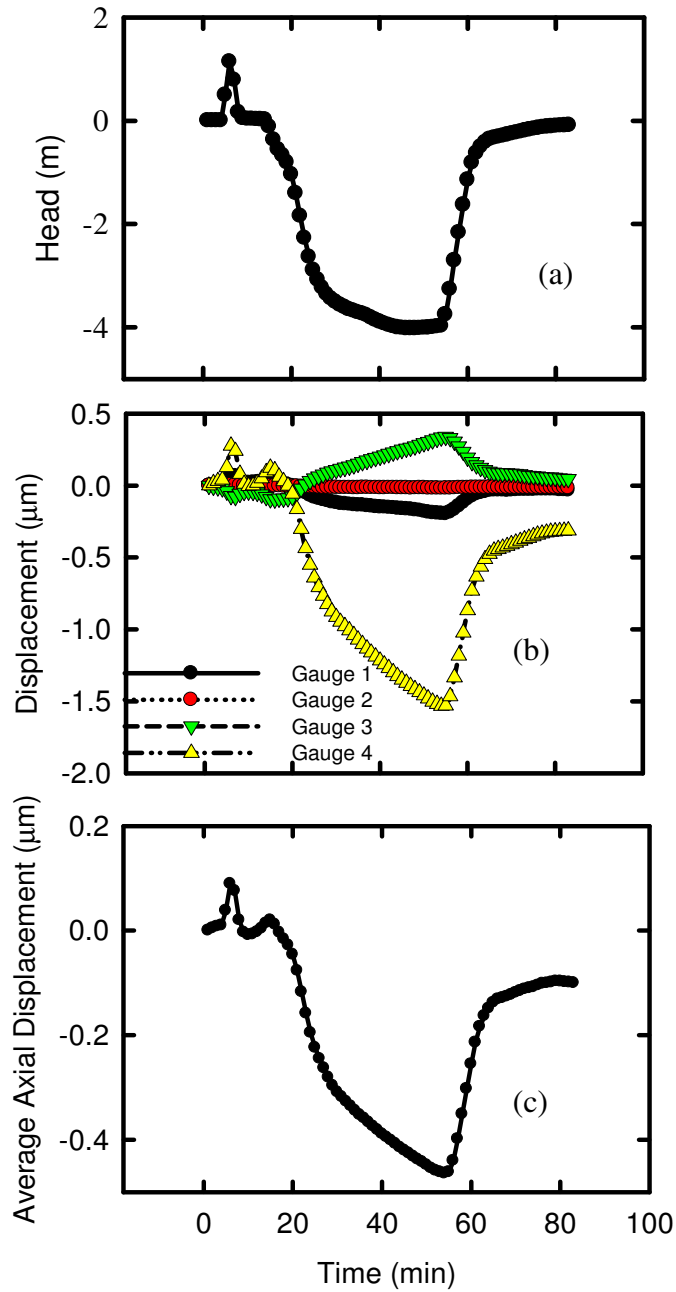
Figure 3.3: (a) Pressure head during a well test as a function of time (b) Axial displacement of each individual gauge as a function of time (c) Average axial displacement of the four gauges as a function of time
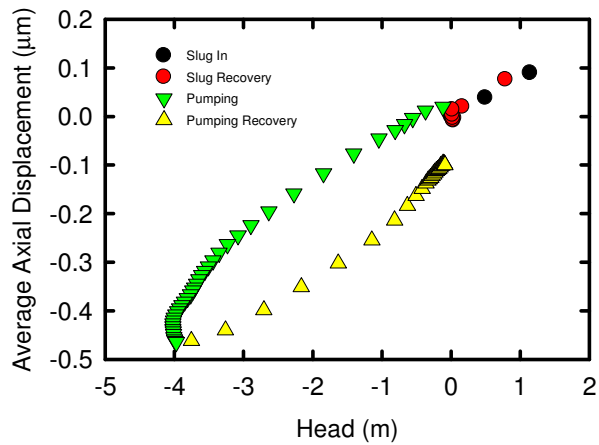
Figure 3.4: Average axial displacement during slug and pumping well tests as a function of head.
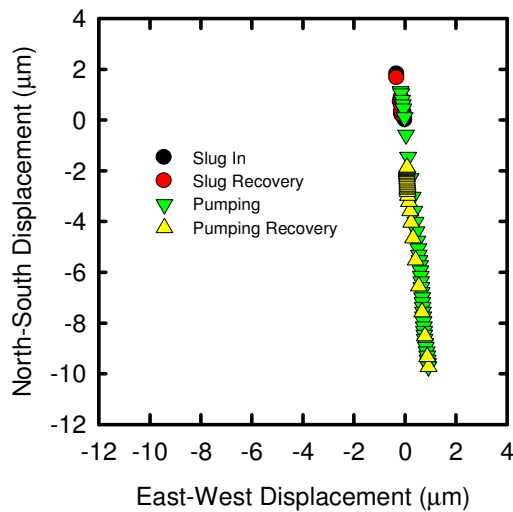
Figure 3.5: Transverse displacement in cardinal directions during slug and pumping well tests.

The displacement data from the fiber optic sensors were averaged to match the measuring rate of the pressure transducer. For instance, the pressure transducer took a measurement every 5 minutes during the hydromechanical well tests at Clemson. The Interrogator was measuring the Bragg wavelength every half second. To match the

displacement data with the pressure data a midpoint average was done for every 600 displacement values. The time corresponding to the middle of every 600 displacement value was equal to the time that the pressure was measured every 5 minutes.

Conclusions

The tests at the field site demonstrated proof of concept of measuring 3D deformation in a well during pumping using fiber optic gauges. The experimental data are similar in magnitude and trend to previous findings (Svenson et al. 2007; Schweisinger, 2008, Hisz et al. 2012).

CLEMSON FIELD SITE

Field tests were conducted in two wells located within fracture biotite gneiss (Nelson et al. 1998) at the South Carolina Botanical Garden in Clemson, South Carolina, USA (Figure 3.6). Overlying the bedrock is approximately 20m of saprolite, which consists of kaolinite, quartz, and iron oxide (Svenson, 2006). The saprolite grades downward through a transition zone into fractured gneiss bedrock.
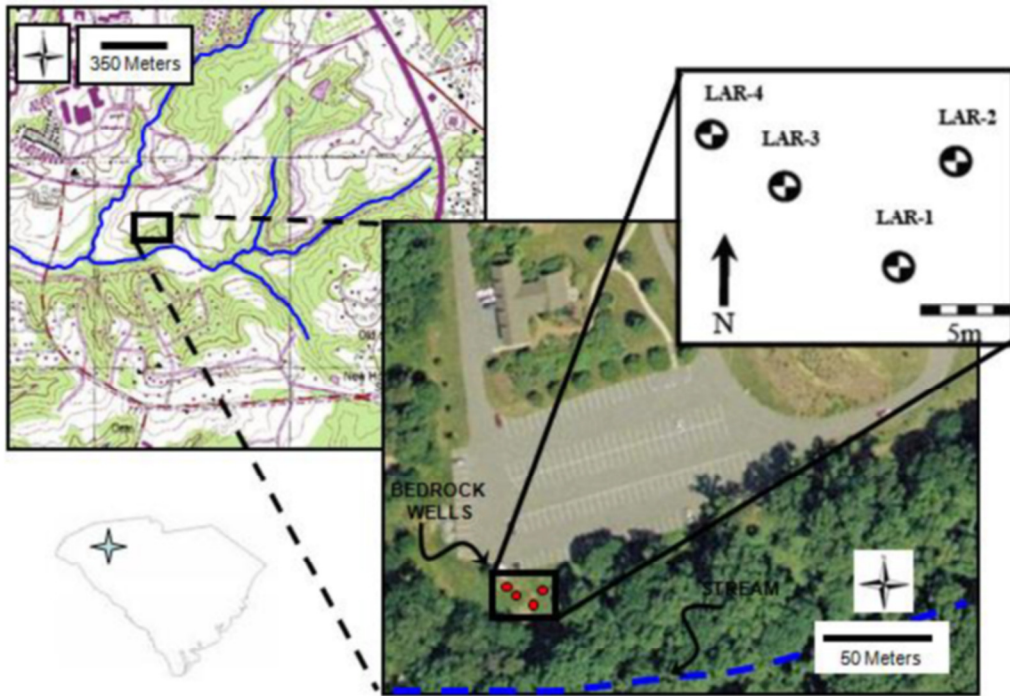
Figure 3.6: The location of the wells at the Botanical Gardens in Clemson, South Carolina, USA (Slack, 2010). The pump was located in LAR-3 for all the tests, and the 3DX was deployed in LAR-2 and LAR-4.

A borehole survey was done by Svenson (2006) to identify the fractures at Clemson well field (Figure 3.7). The distances between fractured zones and single fractures range from a few tenths of a meter to several meters. Most of the fractures occur between 20 meters and 40 meters depth. There are three fracture zones at approximately 25 m, 36 m, and 50 m depth. Tests to determine the hydraulic connection between LAR-4 and LAR-3 were done by Slack (2010). Straddle packers were deployed in the boreholes to separate the zones from the rest of the well during pumping tests. The results determined that the three fractured zones in LAR-3 and LAR-4 are hydraulically connected (Slack, 2010).

74
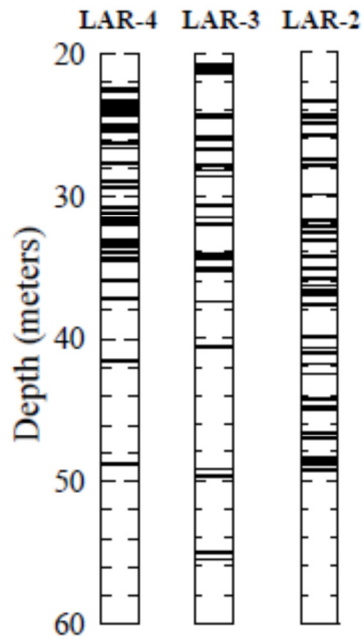
Figure 3.7: Fracture locations from camera survey (Slack 2010).

The strike and dip of the fractures in LAR-2 and LAR-4 was plotted on polar coordinates (Figure 3.8). The lines on the plots indicate the strike direction and the length of the lines indicate the magnitude of the dip angle. The main fracture set in LAR-2 strikes North West to South East and dips on average 60 degrees. The upper fracture strikes north to South and dips approximately 20 degrees. In LAR-4 the upper fractures strike north east to south west and dips 70 degrees. The lower zone strikes north west to south east and dips 50 degrees.
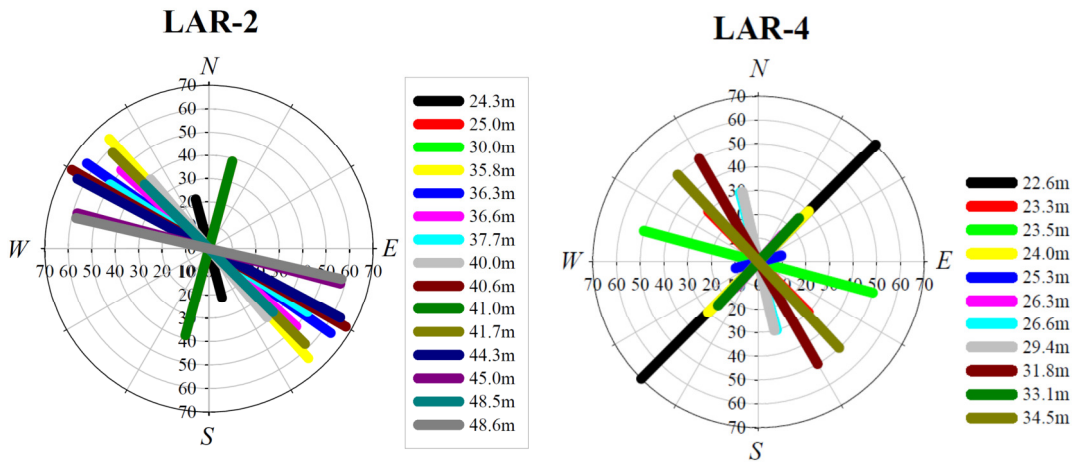
Figure 3.8: Polar coordinates showing the strike and the dip angles of intersecting fractures in LAR-2 and LAR-4 (Svenson, 2006).

A study by Slack (2010) sought to identify hydraulically active connections between wellbores at the Clemson well field (Figure 3.9). The results can be used to determine the dip of the fractures based on their corresponding depths. The results of the study are that the fracture at 25m in LAR-4 and LAR-3 are connected to each other, but are poorly connected to the other wells. The fracture zones at 36m and 50m are intersected by all four wells. The strike of the fracture zone at 36m is approximately EW and it dips to the south roughly 20 to 40 degrees. This permeable zone consists of several fractures spaced a few m apart. The spacing between the wells is 5m, which results in uncertainty in estimates of dip angle. .
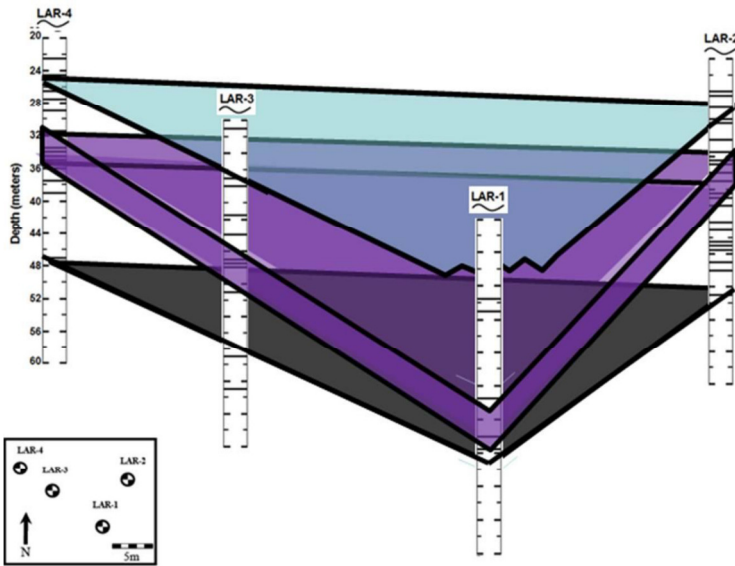
Figure 3.9: Interpretation from Slack (2010) of the permeable zones using straddle packer and MLS methods. The colored triangles represent the hydraulically dominant fractures or fracture zones identified at the Clemson well field.

DESCRIPTION OF CLEMSON FIELD TESTING

Initial testing of the 3DX was in the LAR-2 borehole (Figure 3.10). The 3DX was deployed so the center of the reference rod was at a depth of 23.4 meters. There were two fractures between the anchors of the 3DX at this depth. The pumping well is LAR-3, which is located approximately 6m due west from LAR-2.

The 3DX was deployed in a borehole for a week while displacement, barometric pressure, and pressure were monitored. A series of hydromechanical well tests were be used to stress and cause 3D displacement within the fractures. The hydromechanical well tests involve pumping water from the aquifer while measuring the pressure change and the 3D displacement in the borehole where the 3DX is located.

77

The materials needed to conduct a hydromechanical well test are the 3DX, a pressure transducer, well pump, fiber optic interrogator, computer, and air compressor.

Test Procedure

The initial steps for carrying out the hydromechanical well at the Clemson site are similar to the tests done in Tsukuba, Japan. The 3DX was equilibrated for at least one day, prior to testing. A pressure transducer is set in the well above the 3DX to record the head change. A borehole camera is then used to determine the orientation of the 3DX. The camera has a compass attached to it, and the top of the 3DX was sighted with the compass using the camera (Figure 3.10). The hydromechanical well test involves pumping water from another well nearby at a constant rate of 7 Gal/min for duration of four hours. The recovery takes approximately eight hours to complete.

Figure 3.10: The compass used to determine the orientation of the 3DX in the borehole before a well test. The resolution that can be seen using the camera and compass set up is approximately ±20 degrees.

The results include data from six hydromechanical well tests performed in two different wells, an ambient monitoring analysis, and a test from Trenton, NJ. The data include the pressure change, the axial displacement, and the transverse direction and magnitude. We had already shown from the tests in Japan that the 3DX concept has the capability to detect 3D deformation of a fracture during pumping. The next step is to use the 3DX to do multiple tests from the same fracture, and show that the results are consistent. The reproducibility of the 3DX will come from a comparison of all the tests performed by the 3DX, and by comparing the 3DX results with results from the Tilt-X which has done extensive work at the well field.

Hydromechanical Well Testing

Hydromechanical Well Test 1was done with the 3DX at a depth of 24.3 meters straddling 2 fractures in LAR-2. Hydromechanical Well Test 2 was done with the 3DX at a depth of 24.3 meters straddling 2 fractures in LAR-2. The time between this Test and Test 1 was approximately 24 hours. Hydromechanical Well Test 3 involved retracting the 3DX anchors, raising it by 5 m, and then deploying it back to its original location. The purpose of the test is to evaluate the effects of moving the device. Hydromechanical Well Test 4 was done approximately 48 hours after the device was moved. This test involved removing the 3DX from the borehole, rotating it, and then deploying it at the same location with a different orientation. The 3DX was rotated 135 degrees counter clockwise. Hydromechanical Well Test 5 involved rotating the 3DX by

an unknown amount. The orientation was found by comparing the results to the other three tests to determine the orientation.

The drawdown for all the tests is 1.2 meters (Figure 3.11). The individual gauges all compressed during pumping and extended during recovery for all the tests (Figure 3.11). Individual gauges compressed by different amounts based on the orientation of the device. The average axial displacement of the gauges was ~3.4 microns (Figure 3.11). The average axial displacement compressed during pumping and then extended during recovery to approximately its original displacement (Figure 3.12). The axial displacement decreased slightly at the end of pumping. The late-time slope during recovery of the pressure displacement graph is interpreted as the compliance of the fracture. The compliance of all tests is approximately 4μm/m.

The direction of the transverse displacement is generally the same for all the tests. The 3DX displaces towards the southeast (top anchor displaced relative to bottom anchor) in the first 15 minutes (Figure 3.12). The transverse direction switches directions suddenly to the north east for approximately 35 minutes. It then begins a gradual direction change towards the south east for the remainder of pumping (Figure 3.12). The transverse displacement during recovery changes signs, and displaces back to its original position during pumping. The sudden changes in the transverse direction correlated to times when the pump was turned on and then off again. The magnitude of the transverse displacement is between 8.5 μm and 11.2 μm for all the tests.

Test 4 had a slightly different axial and transverse displacement response. There were two other signals in the axial displacement that caused displacement jumps for

80

Hydromechanical Well Test 4 (Figure 3.12). The axial displacement decreased 1.5 μm before the pump was turned on, and increased 1.5 μm at the end of pumping. There were jumps in the displacement data when the pump was turned on and then off (Figure 3.12). These signals distort the transverse displacement graph and the axial displacement as a function of pressure graph. These signals are the same signals affecting the axial displacement. It could be due to the formation slipping, or the aquifer could be pumped at another location that we are unaware of.

There was a jump in the transverse displacement to the east when the pump was turned on for Test 4. After the jump the transverse displacement is towards the south in the first 15 minutes, and then for approximately 35 minutes the displacement is south east to east, and then to the south east (Figure 3.12). This is similar in trend to the other tests. The path of the transverse displacement during recovery is opposite of the one during pumping.

The relative error is used to calculate the total axial and transverse displacement error. The axial displacement error is approximately 27% of the total displacement. The maximum error is approximately 0.9 μm (Figure 3.14). The relative error of the transverse displacement for all tests is 30% in both directions, and the maximum error is 1.3 μm (Figure 3.13). The relative error for transverse and axial displacement is a fraction of the total displacement measured, so we can assume it is real.
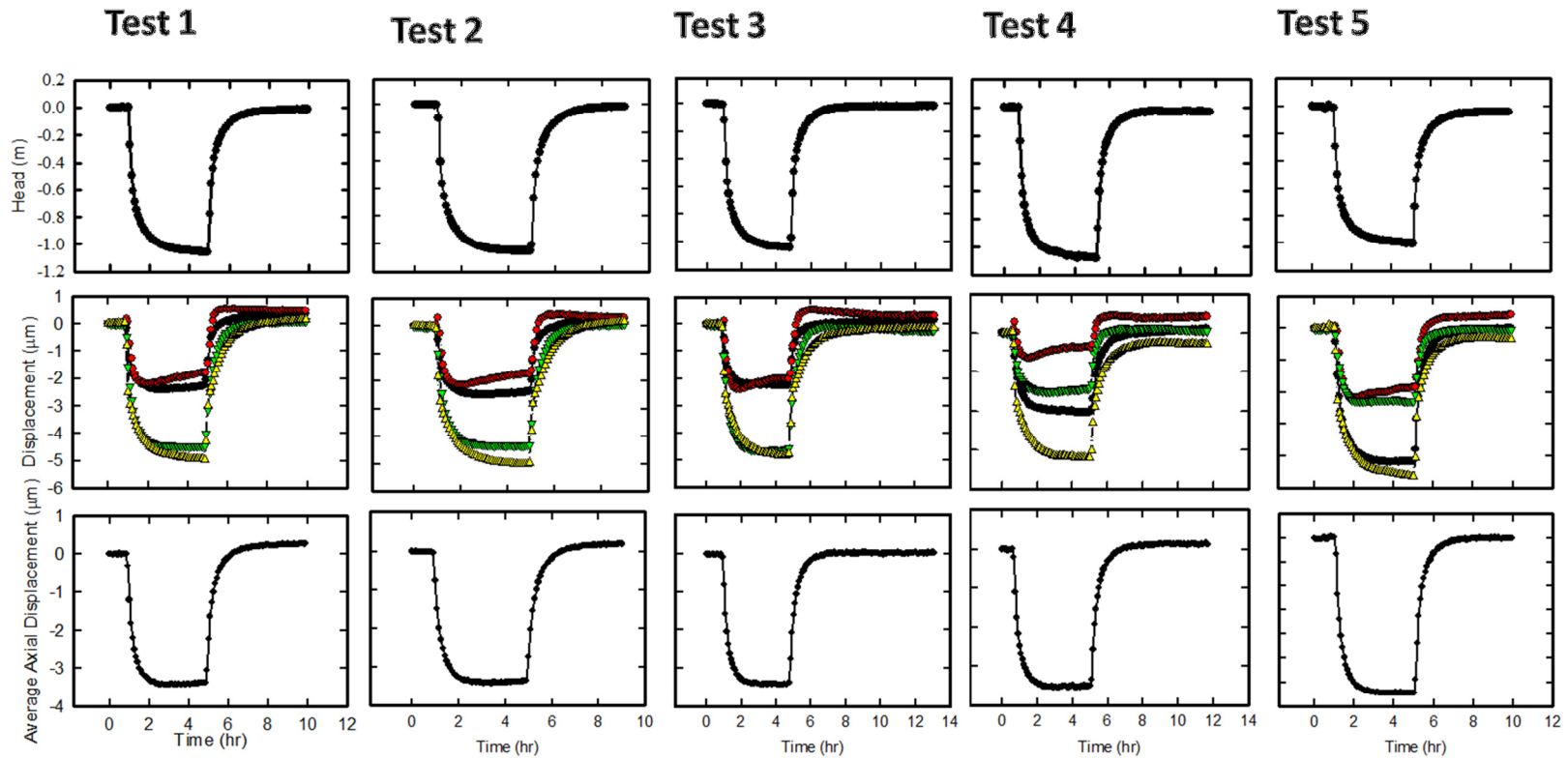
Figure 3.11: Top plot is the pressure head during a well test as a function of time for all the tests. The middle graph is the axial displacement of each individual gauge as a function of time for all the tests. The bottom graph is the average axial displacement as a function of time for all the tests.
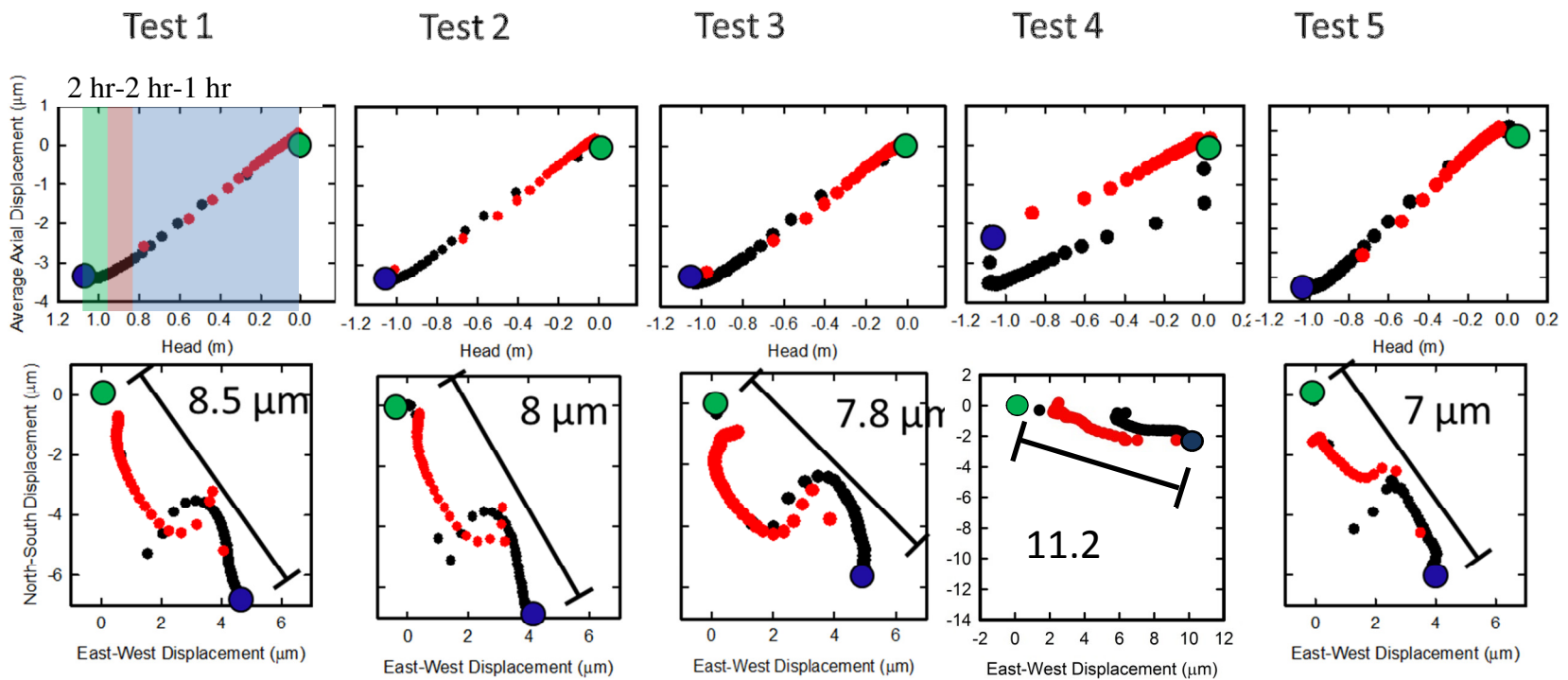
Figure 3.12: The axial displacement as a function of head for five well tests (upper row). Transverse displacement in the cardinal directions (bottom row). The green dot is when the pump is turned on; the blue dot is when the pump is turned off. The black points are during pumping and the red points are during recovery. The blue shaded area represents one hour into pumping. The red shaded area represents two hours into pumping. The green shaded area represents two hours into pumping.
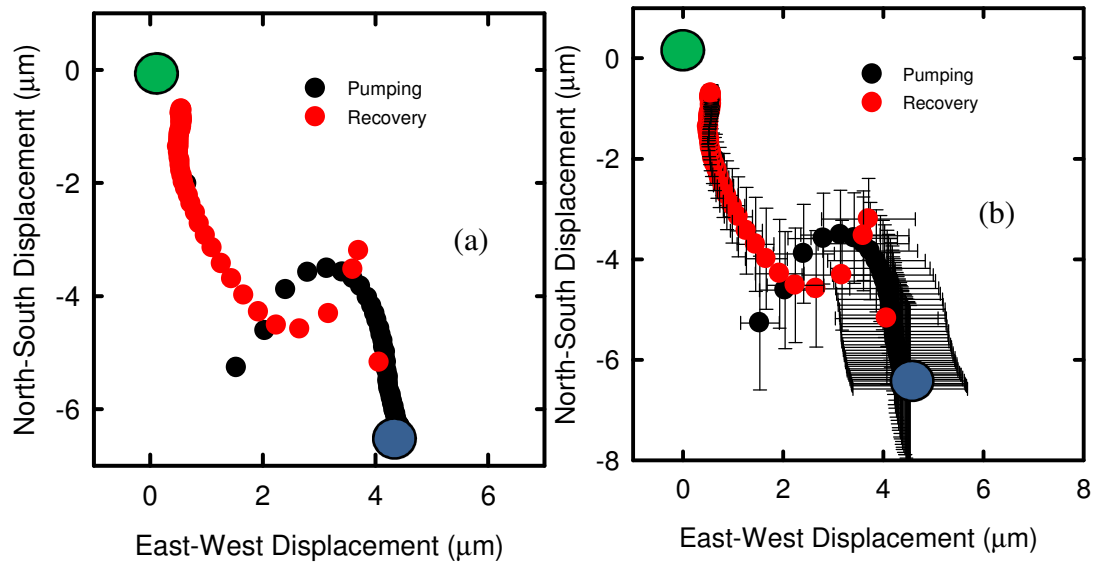
Figure 3.13: (a) Transverse displacement relative to the cardinal directions during well test 1. (b) Transverse displacement plotted with error bars. The green points are the start of pumping the blue point is when the pump is turned off.
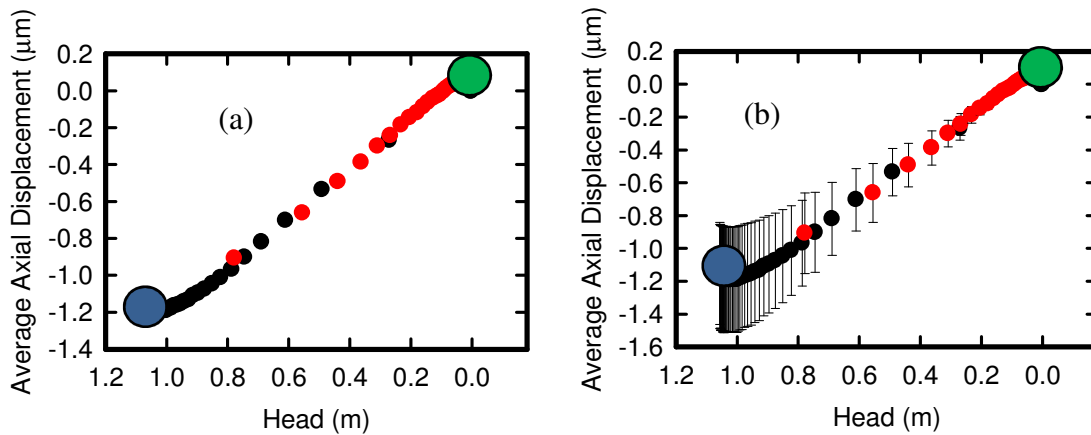
Figure 3.14: (a) Axial displacement as a function of pressure during well test 1. (b) Axial displacement plotted with error bars. The green points are the start of pumping the blue point is when the pump is turned off.

Hydromechanical Well Test 6

The 3DX was moved to LAR-4 to a depth of 24 meters where a hydromechanical test was done. The results of this test can be compared to the results of the Tilt-X which is a device that measures axial extension and tilt in a borehole. The Tilt-X has been used extensively in LAR-4, so the direction of tilt in the borehole during hydromechanical well tests is known.

The head dropped approximately 1.6 meters (Figure 3.15). The axial displacement was 6 µm. The transverse displacement was approximately 12 µm to the west. The compliance of the fracture is approximately 4µm/m (Figure 3.16).

The transverse displacement is to the south initially and then to the southwest for approximately 30 minutes. Displacement then trends to the westnorthwest for approximately an hour, and it trends to the southwest for the remainder of pumping (Figure 3.17, Figure 3.18).
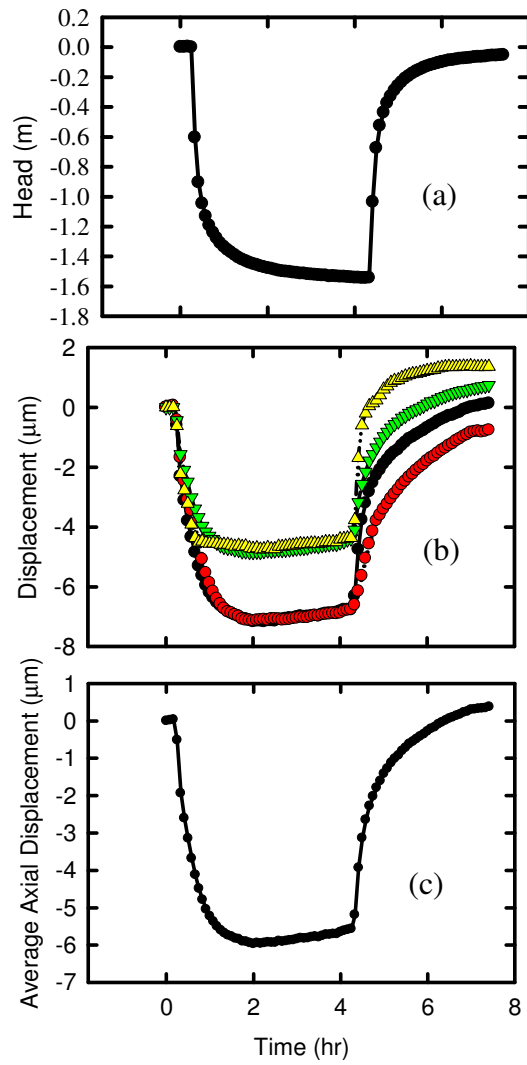
Figure 3.15: (a) Pressure head during a well test as a function of time (b) Axial displacement of each strain gauge as a function of time (c) Average axial displacement of the four gauges as a function of time
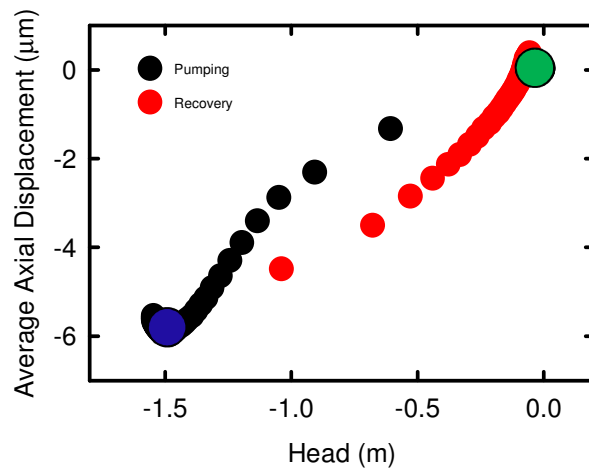
Figure 3.16: Average axial displacement during a well test as a function of head during hydromechanical well test 6.
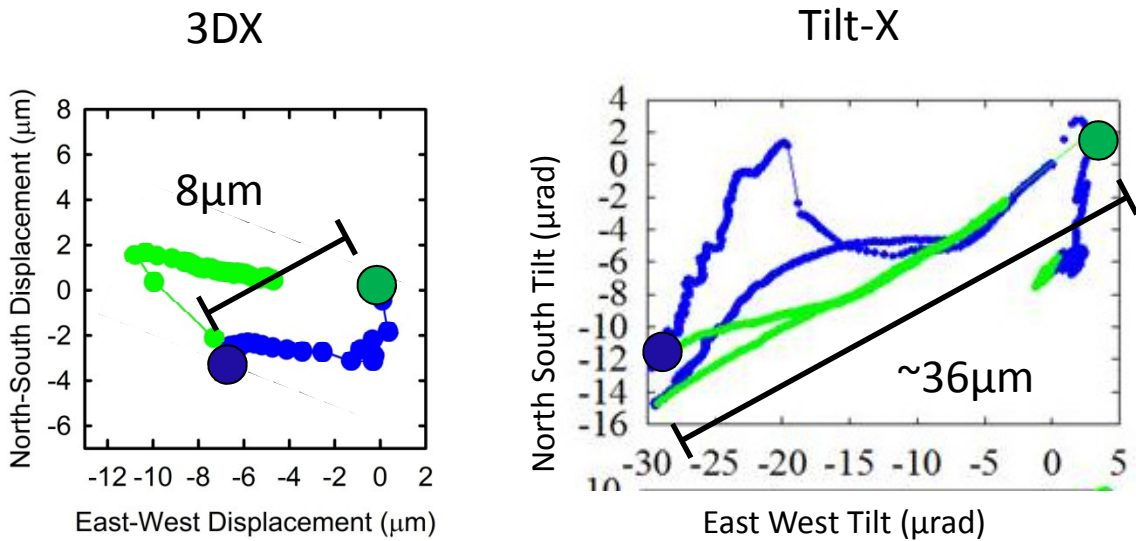
Figure 3.17: Transverse displacement in the cardinal directions for both the 3DX and Tilt-X from the same depth of 24 meters in LAR-2. Green points are recovery, blue points are pumping. The green dot is the start of pumping the blue dot is the beginning of recovery.
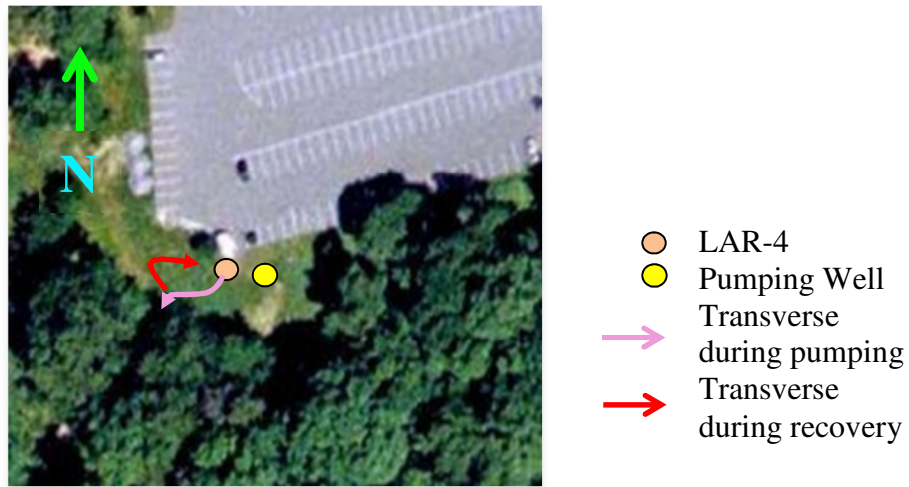
Figure 3.18: The transverse displacement directions during hydromechanical well test 6.

Ambient Monitoring

The 3DX was deployed in LAR-2 at a depth of 24.3 meters for 5 days. This is the same depth used during hydromechanical well test 6. The barometric pressure and the total pressure in the borehole were monitored. The water level is the difference between total pressure and the barometric pressure. The Tilt-X was measuring the axial displacement and tilt in LAR-4 at the same time. The orientation of the gauges is based on the orientation found during hydromechanical well test 5.

Results

The results of the axial displacement and water level vary with a period of 1 day. In the morning the water level reaches a minimum while the displacement is at a maximum opening, and both signals switch in the afternoon (Figure 3.19). The magnitude of the displacement is approximately 0.15 microns. The transverse displacement is also diurnal. The displacement occurs over a 6 hour period in the middle of the day. The rest of the

time the transverse displacement increases steadily on a long-term trend of approximately 2.4 micron/day.

The 3DX and the Tilt-X have a similar response to the diurnal water level change (Figure 3.20). They both indicate axial extension when the water level drops and compression when the water level rises. There is also a long-term trend in the Tilt-X signal, where the axial displacement increases with time. The magnitudes of the signals are different by approximately a factor of 5, where the Tilt-X signal is smaller than that from the 5DX.

The transverse displacement is approximately 2 microns in the north and south direction and submicron in the east and west direction (Figure 3.21). There is a long-term transverse displacement signal trending downward and diurnal transverse displacement signal that occurs in response to the water level change. When the fracture is closing, the top anchor of the 3DX tilts to the north, and when it is opening the tilts is to the south (Figure 3.22, Figure 3.23).
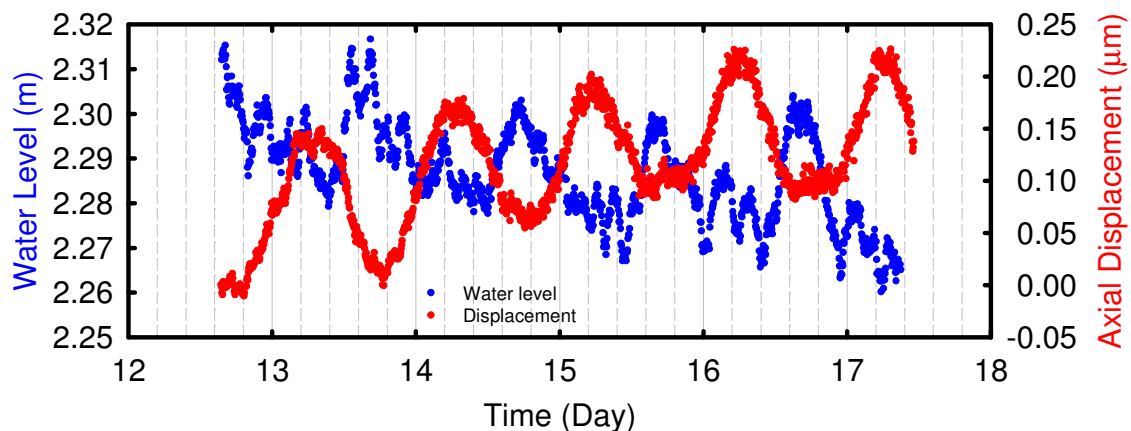
Figure 3.19: The average axial displacement and the water level as functions of time during ambient conditions.
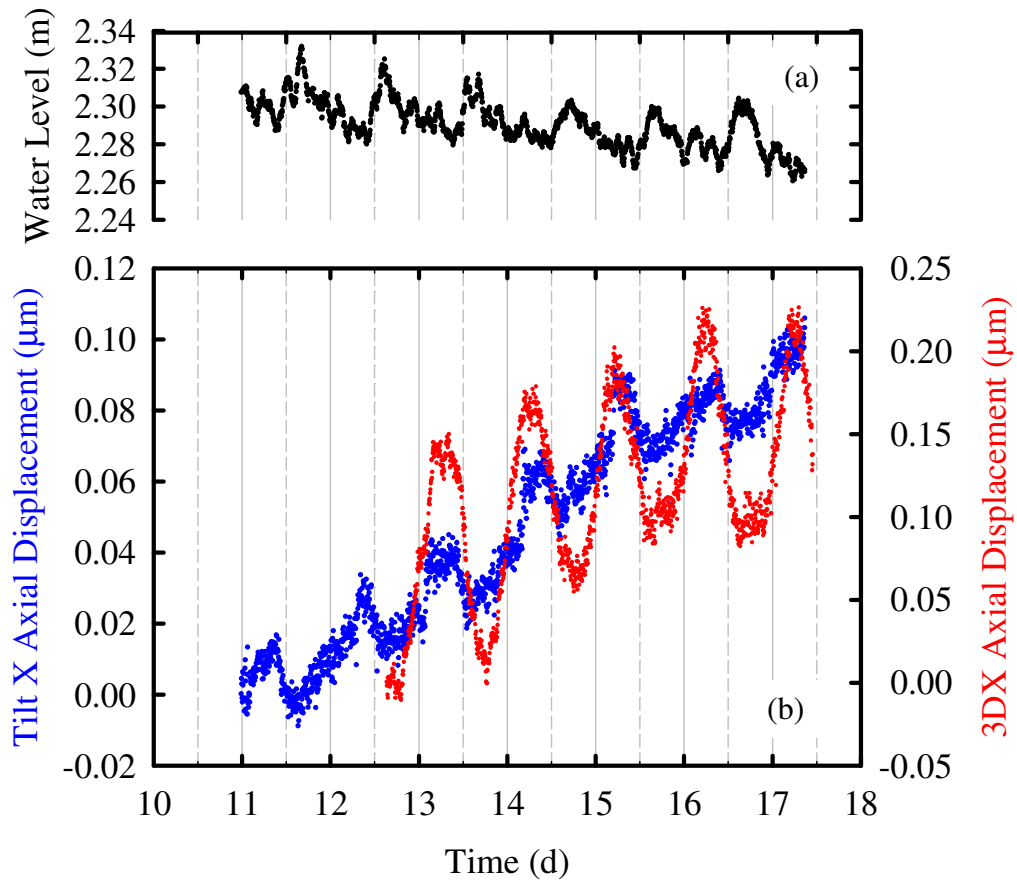
Figure 3.20: (a) Water level as a function of time. (b) Axial displacement measured by both the Tilt-X and the 3DX as functions of time during ambient conditions.
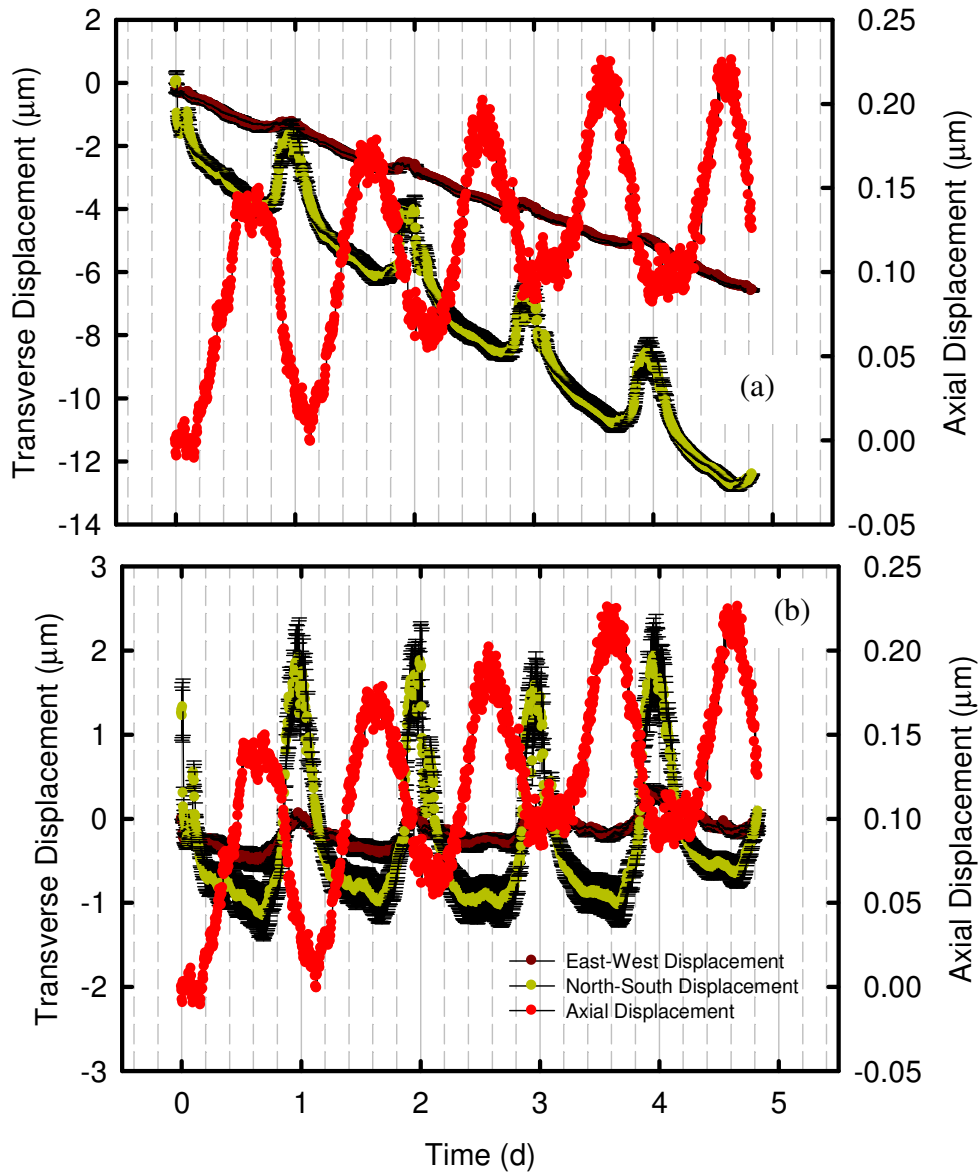
Figure 3.21: (a) Transverse displacement in cardinal directions as functions of time. (b) The transverse displacement after the long-term trend is removed.
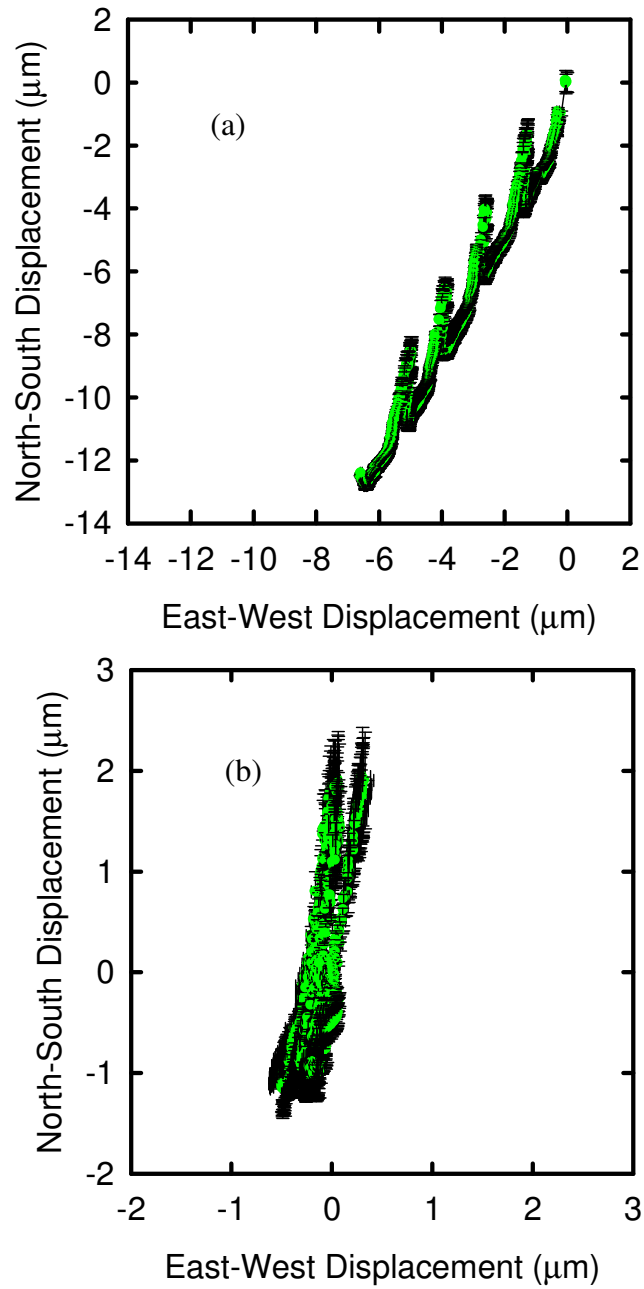
Figure 3.22: (a) The transverse direction of the 3DX during ambient conditions. (b) The transverse direction with the southwest long-term trend taken out during ambient monitoring.
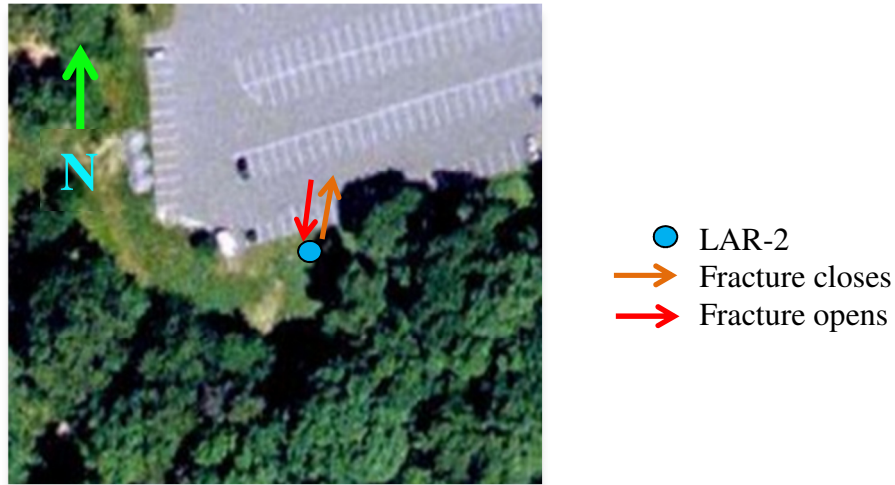
Figure 3.23: The transverse displacement directions during pumping drawn relative to the well field during ambient monitoring

Temperature Effects

A test was done when displacements were measured while the anchors of the 3DX were retracted. LAR-1 was pumped for approximately one hour with the 3DX in LAR-2. The resolution of the temperature monitoring device is ±.001 ℃. The temperature was at a consistent temperature of 18.711 ℃ for the duration of the test. There was a brief temperature change to 18.616 ℃ that occurred for approximately 5 minutes during the test, and then was back to 18.711 ℃ for the remainder of the test. The displacement of the 3DX during this time did not indicate that there would be signals caused by temperature change that might skew the well bore displacement results when the 3DX is anchored.

CHAPTER SUMMARY AND DISCUSSION

There were 6 hydromechanical well tests and an ambient monitoring test at Clemson well field (Table 2). The first five tests were all done in LAR-2. The sixth one

was a hydromechanical well test when the 3DX was in LAR-4.The tests were designed to

evaluate the repeatability of the 3DX, formulate a conceptualization of the subsurface,

and evaluate the ability to perform during characterization efforts for CO2 sequestration.

			3DX straddling permeable zone 1	
Well Test #	Well	Specifications of Test	Axial (µm)	Transverse direction: Transverse Magnitude when fracture is closing (µm)
1	LAR-2	Depth: 24.3 meters	3.4	Southeast: 5 Northeast: 2 Southeast: 3
2	LAR-2	Performed 24 hours after first test	3.4	Southeast: 5 Northeast: 2 Southeast: 3
3	LAR-2	Anchors retracted; moved 3DX up and down; set anchors again to same depth	3.4	Southeast: 5 Northeast: 2 Southeast: 3
4	LAR-2	3DX rotated and set at same depth	3.4	Southeast: 1 Southeast/east: 4 Southeast: 0.5
5	LAR-2	Unknown orientation	3.4	Southeast: 5 Northeast: 2 Southeast: 3
6	LAR-4	Compared to results from Tilt-X Depth: 24 meters	6	Southwest: 5 West: 7 South west: 0.2
Ambient	LAR-2	5 day test Compared to results from Tilt-X	0.15	North: 3
Table 2: Results from the hydromechanical well tests done at Clemson's well field with the 3DX				

<u>Reproducibility</u>

The five hydromechanical well tests from LAR-2 are used evaluate the

repeatability of the 3DX when it is deployed at the same depth.   The axial displacement

trend for all five tests was similar. The maximum axial displacement as a function of pressure was 3.4 μm for all the tests with a drop in head of approximately 1.2 meter (Figure 3.24). The axial displacement decreased during pumping and increased during recovery for all the hydromechanical well tests. The late time slope of the axial displacement as a function of pressure is 4 $\mu m/m$ for all the tests. The shape of the axial displacement as a function of pressure for most of the tests is the axial displacement is less during pumping then at the same head during recovery. This creates a hysteretic shape in the graphs.

The general transverse displacement trend is similar for all five tests (Figure 3.24, Figure 3.25). The transverse displacement follows sigmoidal pattern. It is initially to the southeast, then to the northeast, finally to the southeast for the remainder of pumping. The magnitude of the transverse displacement in the east and west direction during pumping is between 4 and 5 μm. The magnitude of the transverse displacement in the north south direction during pumping is 2 and 7 μm. The transverse displacement graph shows that the 3DX returns to within a few tenths of a micron from its initial location during recovery.

The results from Test 4 are slightly different than the other tests. There were abrupt displacements when the pump was turned on and off, which were absent from the other tests the origin of the abrupt displacements is unclear but this was the only test where they occurred, so they were removed to compare the results to the other tests. The transverse displacement during Well Test 4 is to the east-southeast. This trend is similar to the other tests, although the transverse displacement is to the south when the pump is

turned on, then to the east, and then to the south east for the rest of pumping. The fifth

well test which had an unknown orientation had the same transverse displacement trend

as tests 1 through 3, which is how its orientation was determined.
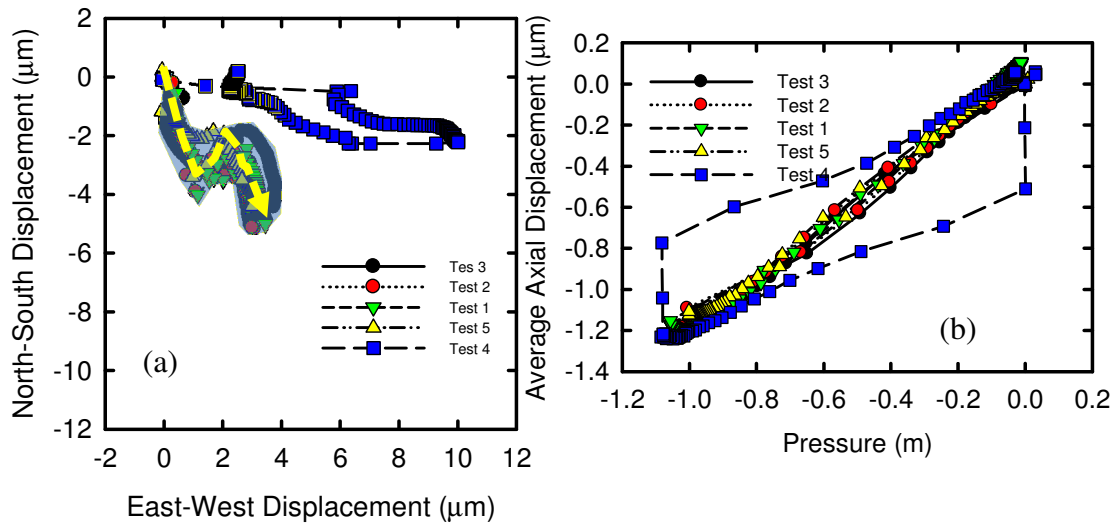
Figure 3.24: (a) Transverse displacement for the 5 tests in LAR-2 (b) Axial displacement as a function of pressure graphs for all 5 tests in LAR-2. The yellow dashed line is the general transverse direction for four of the tests, and the blue shadow the range that these tests cover.

LAR-2
Pumping Well
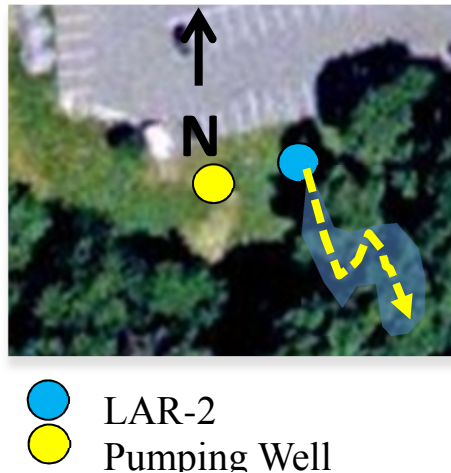
Figure 3.25: The general transverse displacement direction for five hydromechanical well tests.

96

3D displacement during ambient monitoring

The 3D displacements during ambient conditions follow diurnal fluctuations in water level. When the water level drops the fracture opens and when the water level rises the fracture closes. The signal observed by the 3DX was confirmed by data from the Tilt-X, which was similar in orientation and timing, but different in magnitude. The Tilt-X was deployed in a neighboring well, so the difference in magnitude may result from local differences in aquifer properties. Nevertheless, the general similarity of the Tilt-X signal (e.g. Figure 3.19) is taken as a confirmation of the 3DX data.

The observed displacements apparently occur as a result of the interaction between barometric pressure changes and the water in the well. Water level changes in response to barometric pressure. Water level in the well drops with an increase in barometric pressure, which is the typical response of wells to barometric pressure changes (NGWA, 1999). A water level drop in the well casing means that water must flow from the casing into the formation this causes the fracture to open, just as injection using a pump or slug opens fractures.

The transverse displacement direction during ambient monitoring is to the north when the fracture is closing and to the south when the fracture is opening. It appears that the transverse displacement direction follows the southward dip direction of the fracture zone at approximately 35 m. When a dipping fracture closes, the displacement of rock on the hanging wall of the fracture will occur in the up-dip direction relative to the foot wall (Figure 26 and Figure 27). This is similar to the effect seen by Burbey et al. (2012), who

characterized the dip direction of a fracture based on the tilt direction. (Figure 26 and

Figure 27).
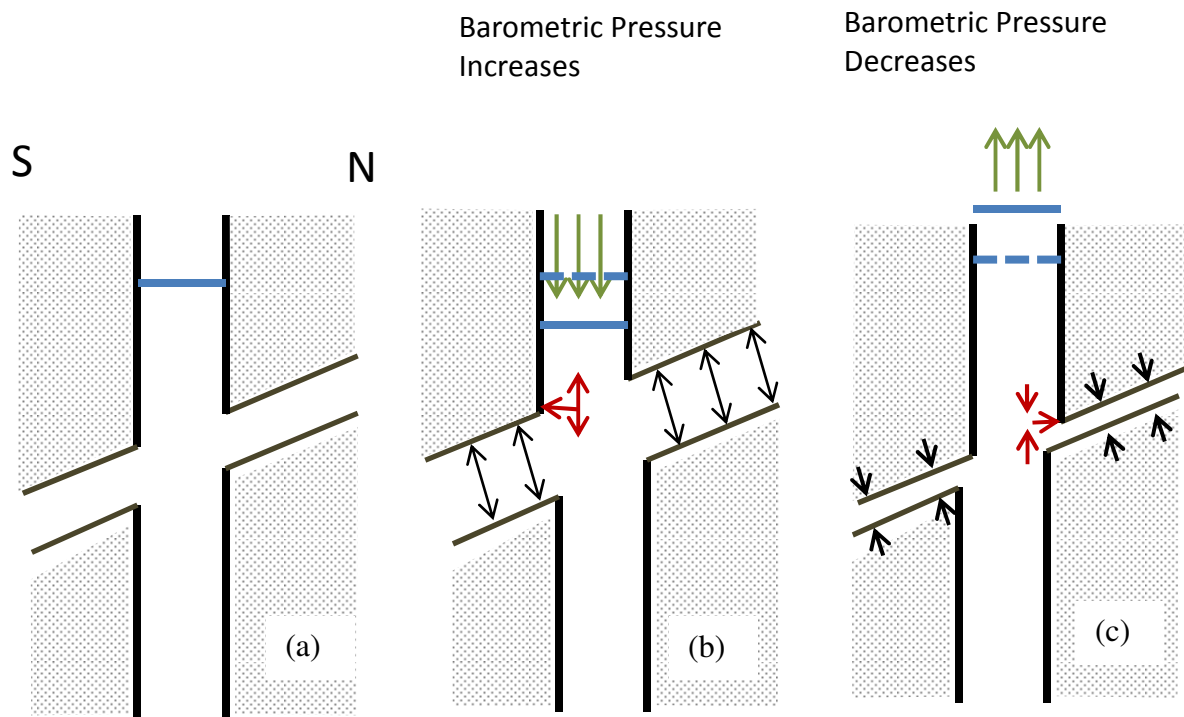
Figure 3.26: (a) Conceptualization of fracture intersecting a borehole. (b) When barometric pressure increases fracture opens and transversely displaces down dip. (c) When barometric pressure decreases fracture closes and transversely displaces up dip.
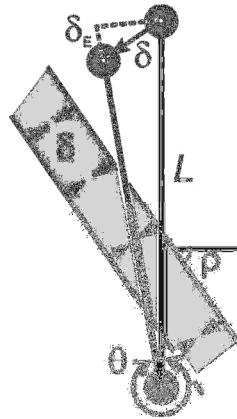
Figure 3.27: Displacements during closing of a dipping fracture showing tilt, θ, displacement measured by the extensometer, δ_E, and the normal displacement of the fracture, δ. Dip of the fracture is ρ. L is gauge length (Burbey et al. 2012).

Axial displacement during hydromechanical Well Tests

The results from previous hydromechanical well tests indicate that the axial displacement as a function of pressure is a hysteretic function (Svenson et al. 2008; Schweisinger and Murdoch 2011; Burbey et al. 2012). This means that the axial displacement is larger after the pump is turned off compared to when the pump is on for the same head level. The reason for this is when the pump is first turned on the pressure wave is spread over a small area. The fracture is responding elastically to these local pressure changes by deforming within the vicinity of the drop in pressure (Murdoch and Germanovich 2006). When the pump is turned off the induced pressure change has spread out, affecting a larger area. Due to the differences in the sizes of the pressure fronts when the pump is turned on and off, there is more leverage to cause the fracture to deform. This in turn causes the axial displacement to be larger during recovery compared to during pumping.

100

Axial displacement as a function of pressure occurs in the 3DX data. The axial displacement as a function of pressure during the tests in Japan, LAR-2, and LAR-4 is greater during recovery than at the same head during pumping (Figure 3.4, Figure 3.11). The axial displacement of the fracture is closing during pumping, and opening after the pump is turned off. There is an unexpected axial displacement response in all the tests done at the Clemson well field where the fracture opens slightly after pumping for 3 hours (Fig 3.12). The increasing axial displacement lasts for approximately an hour (Figure 3.12). The head continues to decrease during this time.

Axial Displacement magnitude

The magnitude of the axial displacement measured by the 3DX is larger than the measurements made by the Tilt-X. The displacements measured by the Tilt-X are approximately 1 $\mu m / m$, and the displacements measured by the 3DX are 3 $\mu m / m$ in LAR-2 and 6 $\mu m / m$ in LAR-4. One explanation for this difference is from the calibration of axial measurements of the 3DX. The 3DX was calibrated axially by first suspending the device vertically in a frame that was attached to the wall by concrete wedge anchors. Weights were then hung from the bottom of the device causing the strain bar and gauges to extend axially. There was a micrometer at the top of the bottom anchor that measures the axial displacement change when the weights were hung. A possible effect is when the weights were applied, the calibration frame moved and contributed to the total vertical movement. In this case, the axial constant would overestimate the total axial displacement in the field. This effects is currently being evaluated and will likely result in a revised calibration factor.

Another explanation is related to the calibration of the Tilt-X and the 3DX. The entire 3DX was used during calibration in order to account for compliance of the overall device. Only the DVRT sensor in the Tilt-X was calibrated, however. The Tilt-X is stiffer than the 3DX because it lacks the intrinsically compliant strain bar, so we assumed that the compliance of the Tilt-X could be ignored. However, it is possible that the compliance of the Tilt-X would cause the displacement of the anchors to be greater than that measured by the DVRT. This would contribute to an explanation of the difference between the results from the 3DX and the Tilt-X Nevertheless; it is possible that compliance in the Tilt-X frame and anchors would cause the actual displacement to be larger than that measured by the DVRT.

Transverse Displacements during Hydromechanical Well Tests

The results from LAR-2 are from the 3DX at a depth of 24.3 meters, and the results from LAR-4 are from the Tilt-X at a depth of 22 meters (Figure 3.28). These two zones were identified by Slack (2010) as being slightly hydraulically connected, and dipping to the south. The pumping well is in between both boreholes. The transverse displacement observed in both boreholes is in opposite directions during the beginning of pumping, after 1 hour it is in the same direction. The tilt in LAR-4, measured by the Tilt-X, is initially toward the southwest, and then it swings west, and rotates back to the south. Transverse displacement in LAR-2, measured by the 3DX, is roughly a mirror image of the tilt in LAR-4 on the opposite side of the pumping well (it goes to the southeast→east northeast→southeast.
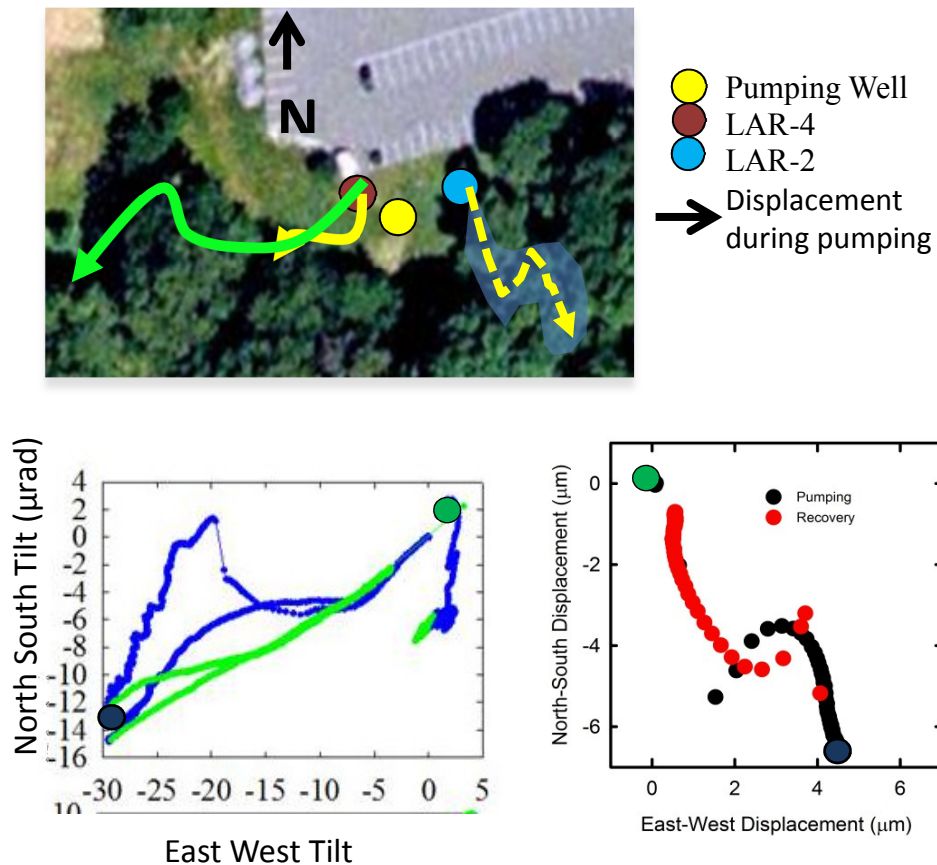
Figure 3.28: Transverse displacements from well testing at 24.3 m in LAR-2 and 22 meters in LAR-4. The green dot is the beginning of pumping. The blue dot is the beginning of recovery.

The results are surprising because under ideal conditions tilting is expected to occur on a radial path from the monitoring point to the pumping well. Analytical models of pumping in a homogeneous aquifer suggest that the tilt in porous media will be in the same direction a radial line through the pumping well (Kumpel, 1989; Lehmann, 2001, Wang and Kumpel 2003; Burbey and Helm 1999). In contrast, instead of being parallel

to a radial line from the pumping well, the tilt and transverse displacements are at high angles to the radial line.

One possible explanation for this discrepancy is that the tilt and transverse displacements are affected by a fracture that is dipping. An analytical analysis done by Hisz et al. (2012) evaluated the tilt field that would occur at 24 meters around a pumping well with a dipping fracture at 35 meters embedded in a uniform tight porous matrix (Figure 3.29). The results are that the tilt at 24 meters radiates from a point approximately 5 m up-dip from the well (Figure 3.30). The analytical results are similar to the results obtained in the field (Figure 3.30).
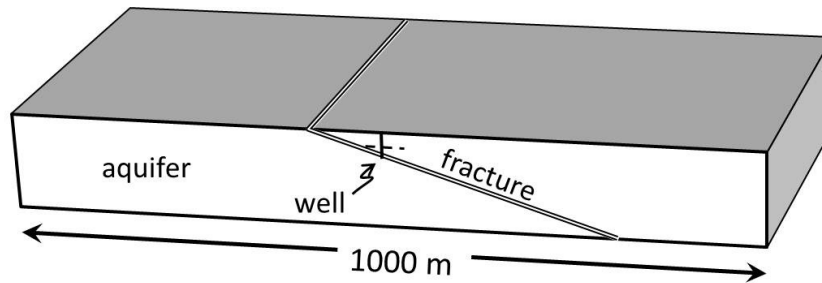
Parameter	aquifer	fracture
Young's Modulus, E	10^9 Pa	0.5×10^9 Pa
Poisson's ratio, μ	0.25	0.25
Permeability, k	10^{-15} m^2	10^{-11} m^2
Biot-Willis coef, α	0.7	0.7
Biot Modulus, M	3×10^9 Pa	1.5×10^9 Pa

Figure 3.29: Geometry and parameters used in Hisz et al. (2012) analysis of a dipping fracture embedded in a homogeneous aquifer.
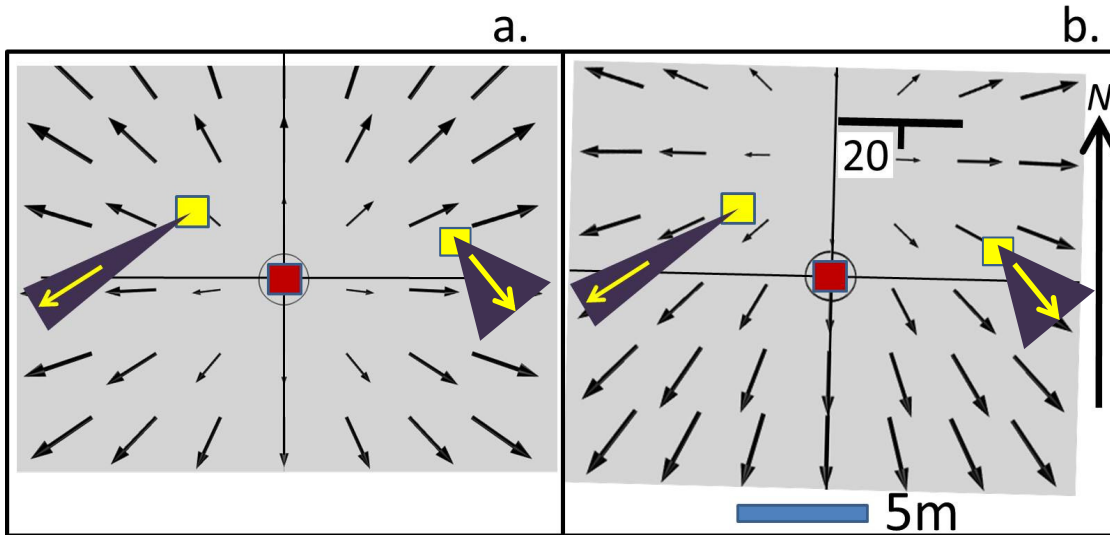
Figure 3.30: Tilt vectors (arrows) predicted at a depth of 25 m in the vicinity of the pumping well (red square). Observed azimuth of tilts (purple wedge and yellow arrow) at monitoring well (yellow square). (a) flat lying fracture. (b) fracture oriented as shown with strike and dip symbol (Modified graph from Hisz et al 2012)

Flow Dimension

We can support the further evaluate the pumping tests by evaluating the flow dimension. The flow dimension (n) describes the flow area as a function of radial distance from the borehole. Flow dimension reflects the deficit or excess of interconnected flow paths in fractured rocks compared to one-, two-, or three-dimensionally connected networks (Doe, 1991). It is how fluid fills space as it moves through fractures (Doe, 1991). It allows the basic geometry of the flow system to be estimated, and shows how that geometry changes in space (Beauheim and Roberts 2004). Flow dimension of a hydraulic test may reflect several characteristics of the hydrogeologic system, including heterogeneity, boundaries, and leakage. Flow dimension analysis can characterize the flow in three dimensional space; linear flow

105

(n=1), radial flow (n=2), spherical flow (n=3), fractional flow (when n is a non-integer)

(Figure 3.31).   A single planar fracture will have a flow dimension of 2.
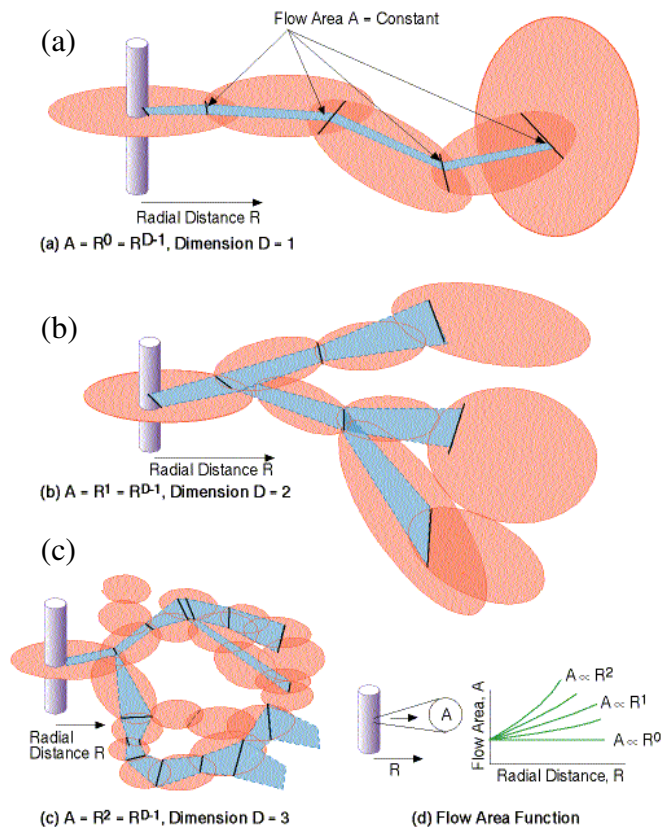
Figure 3.31: Conceptualization of (a) linear flow; (b) radial flow; and (c) spherical flow (Golder Associates 1998)

Barker (1988) found that the flow dimension was related to how the flow area changed with distance from the source, and *n* described the geometry of the system according to

$$Area(r) = b^{3-n} \frac{2\pi^{\frac{n}{2}}}{\Gamma\left(\dfrac{n}{2}\right)} r^{n-1}$$

(3.20)

where b is the extent of the flow zone, Γ is the gamma function, and r is the radial distance from the borehole. For example, when the flow dimension is radial (n=2) Equation 3.20 simplifies to

$$Area(r) = 2\pi rb$$

(3.21)

Barker's flow dimension analysis applied to a well pumping at constant rate

$$h(r,t) = \frac{Qr^{2v}}{4\pi^{1-v}Tb^{2-n}}\Gamma(-v,u)$$

(3.22)

$$v = 1 - \frac{n}{2}$$

(3.23)

$$u = \frac{S_s r^2}{4Kt}$$

(3.24)

where h is the drawdown, Q is the constant pumping rate, T is the transmissivity, b is the extent of the flow region, and $\Gamma(-v, u)$ is the incomplete gamma function. Equation 3.22 reduces to the Theis (1935) equation when $n=2$

$$h(r,t) = \frac{Q}{4\pi T} E_1(u)$$

(3.25)

107

Leveinen (2000) presents a simple way to calculate the flow dimension by determining the slope of the log-log plot of the drawdown as a function of time, and using the slope at each point to determine the flow dimension

$$n = 2*(1 - slope)$$

(3.26)

The analysis of the flow dimension was done using drawdown results from LAR-2 during hydromechanical well test 1 (Figure 3.32). The result of the analysis indicates that initially the flow dimension $n<1.0$, but it increases during pumping to reach $n=1.0$ after 30 minutes and $n=1.5$ after 50 minutes. The flow dimension is in the range of $1.8<n<2$ after 100 minutes and it stays in this range until pumping stops after 210 minutes (Fig 3.33).

Transverse displacement follows a sigmoidal pattern, and most of the variability occurs early in the pumping period when $n<1$. When $n>1$, the direction of transverse displacement is uniformly to the southeast with an azimuth of 150° (Fig. 3.32). Interestingly, both the tilt and the transverse displacement are away from the pumping well during the early stage when n<1, and then they rotate and are nearly perpendicular to a radial line from the pumping well (Fig. 3.32).

Flow dimension of unity early in a well test is typically associated with wellbore storage (Levienen 2000). The well bore was open during pumping, so water released from wellbore storage is a plausible process that could affect results from the well test. Flow dimension in a uniform, planar fracture is expected to be n=2, and preferential flow

108

paths within the fracture could reduce the dimension to the range $1.8 < n < 2$ (cite) (Figure 3.33).

The conclusion that emerges from the flow dimension analysis is that the early deformation (50 min $< t$) is affected by a process associated with wellbore storage, which causes tilt and transverse displacement toward the pumping well at early time. The importance of this process diminishes with time, and at later times ($t > 100$ min) tilt and transverse displacement are affected primarily by deformation of a dipping fracture.

Deformation associated with the wellbore storage stage could result from the changing pressure on the wellbore itself. The rapid drop in pressure early in the well test will cause the wellbore to contract, and the magnitude of the contraction will vary with the elastic modulus of the aquifer and casing. The elastic modulus of saprolite is expected to be roughly four orders of magnitude less than that of rock, so contraction inward toward the well is expected to be greater in the saprolite than in the underlying rock. This would cause tilting and transverse deformation toward the well.
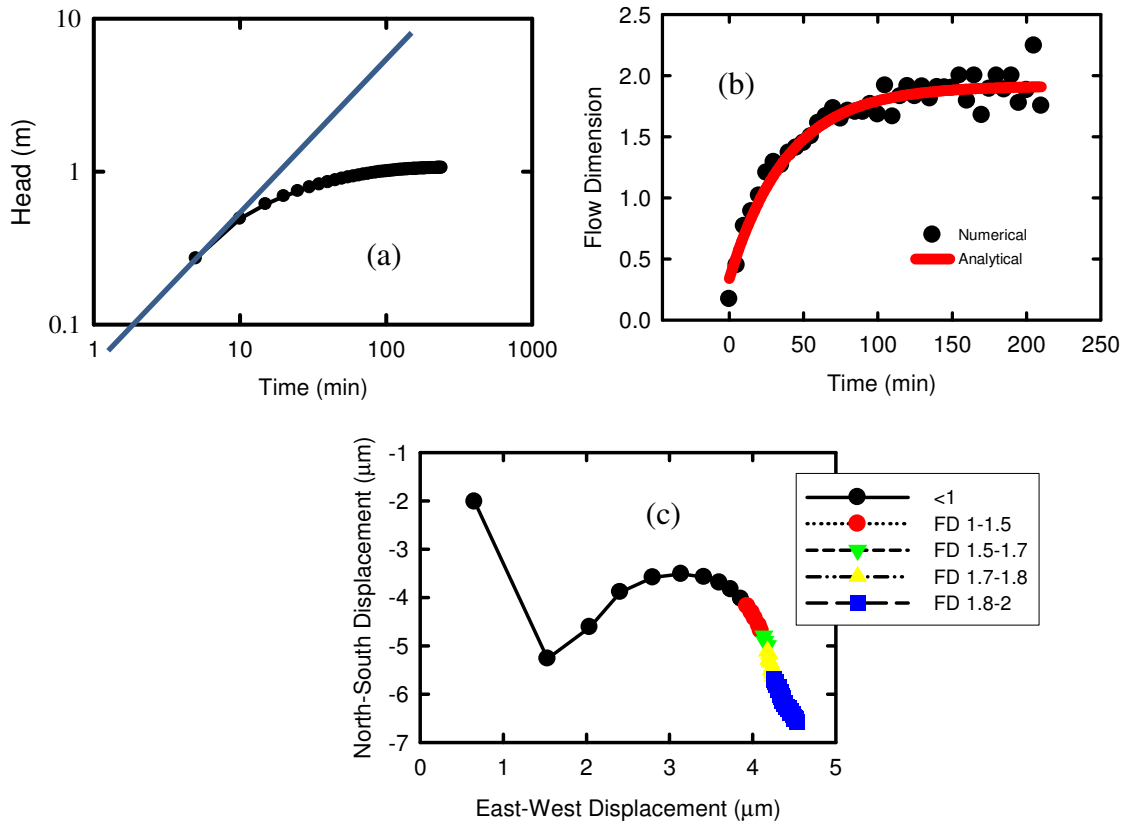
Figure 3.32Figure 3.33: (a) Drawdown as a function of time in well LAR-2 from a pumping test in LAR-1, (b) the flow dimension as a function of time during a pumping test in LAR-1, (c) the transverse displacement in LAR-2 during a pumping test
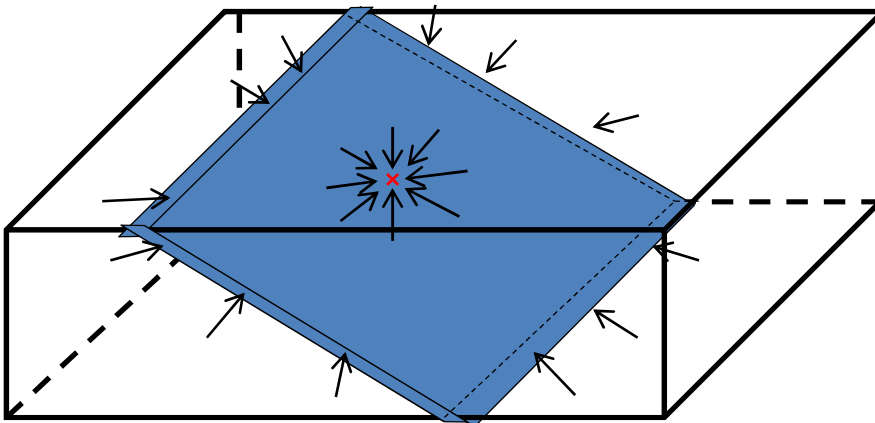
Figure 3.33: Conceptualization of the flow geometry for a dipping fracture

The transverse and axial displacement can be used to determine the dip of the fracture. It follows from Fig. 3.13 that

$$Dip = \arctan\left(\frac{\delta_T}{\delta_A}\right)$$

<div align="right">(3.27)</div>

where δ_T is the transverse displacement and δ_A is the axial displacement. The ratio of transverse to axial displacement from the field results is 2:1. The resulting dip angle is approximately 60°. This angle is greater than suggested by packer tests and camera surveys by Slack (2010), who indicates the dip of the fracture zone at 35 m is in the range of 25° to 40°. The fractures in the 35-m-zone extend over 1 to 2m and the wells are 5 m apart, so there is some uncertainty in the dip estimates from the field data. Nevertheless, it seems likely that the dip is less than 60°. It is possible that δ_T and δ_A from 3DX will change after additional refinement of the calibration and this may result in a shallower dip calculated using eq. 3.27.

Mobility of the 3DX

The 3DX has been used for hydromechanical well tests at three different locations: Tskuba, Japan; Clemson, SC; and Trenton, NJ. It has been transported by both plane and automobile. For transportation it can either be disassembled and assembled on site, or kept together and mobilized in a protective case. There has not been any damage during transportation, which is a testimony to the durability of the instrument.

<div align="center">111</div>

Limitations

Currently the major limitation of the 3DX is the durability of the strain gauges. When the 3DX is deployed the gauges are secured to the strain bar, so if the anchors transversely or axial displaces a few millimeters the gauges might be damaged. A damaged gauge may reflect a Bragg wavelength, but the calibration will be affected so the uncertainty in the measurement is larger than expected. A possible solution is to modify the strain bar to include a system that can secure the gauges until they are used for a measurement.

Signal Confidence

One drawback of using FBG gauges is that they are relatively unprotected from large displacements that occur during deployment. The gauges used for these tests have a strain limit of $2500\,\mu\varepsilon$, and the chance of the gauges breaking increases past this point. When the 3DX is being deployed the gauges are active, and are exposed to deformation that may occur until the anchors are set. The frame protects the gauges during deployment by restricting the relative movement between the anchors. The second sets of cuts are more compliant then the cuts the strain gauges are on, so they will deform more readily than the strain bar. Even so, there are events that could take place downhole that might break the gauges. Examples of these situations are the anchors being set on a section of the borehole that is rough, causing anchors to drastically displace or rotate relative to each other. Alternatively, pulling on the cable while either the anchors are engaged or the instrument is stuck may stretch the gauges past their elastic limit.

Stretching the gauges past their elastic limit can cause an operational problem because the gauge may still return a signal that change with the strain. The problem is

112

that damage to the gauge has significantly changed the calibration (typically by markedly reducing sensitivity). As a result, the signal can be analyzed to infer a deformation that is too small.

A method is needed that will quantitatively characterize the confidence of the measured displacements by the gauges. The functionality of the strain bar can give an idea as to the expected response of the gauges during deformation. When there is compression of the strain bar all the gauges will compress, and the average is the total compression. When there is transverse displacement the strain bar rotates, compressing one side and extending the other. The gauges will displace equally but in the opposite direction (Figure 3.34). When there is transverse displacement during a well test we can compare the two sets of gauges that are opposing each other. If one gauge is compressing more than the average displacement the opposing gauge should show less compression than the average. Then if the difference gauges from the average they would be approximately equal. If there is a set of gauges that is not displacing transversely then the average of those gauges would be similar to the average axial displacement.
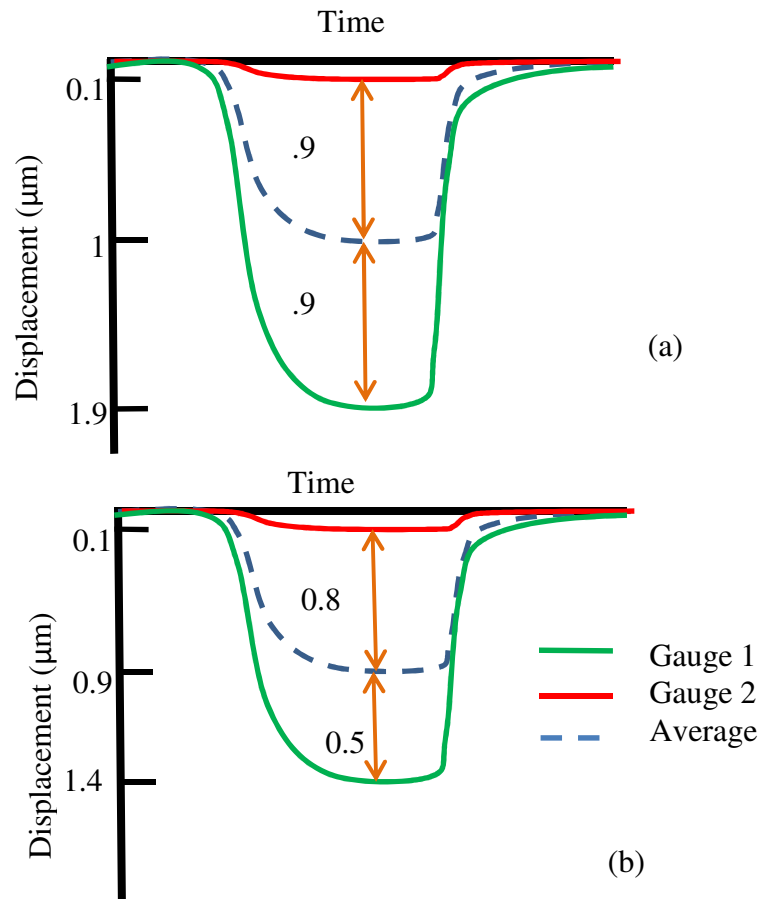
Figure 3.34: A possible method for interpreting whether gauges are damaged during a well test. The dashed blue line is the average of all four gauges. (a) shows that Gauge 2's response is small, but it is equal and opposite to the response of Gauge 1. This indicates that the gauges are all working properly. (b) shows the same response from Gauge 2, but it is not equal and opposite to Gauge 1. This indicates a broken gauge. The average displacement is from all four gauges so it will more likely reflect the actual displacement even though the broken gauge is included.

The difference between the average axial displacement and the bending of opposing gauges will differ. There needs to be a way to determine the range of accepted percent errors that would still qualify a gauge as working. The method used to calculate

the error is to determine the average wavelength change during transverse displacement
of all four gauges

$$\lambda_{Avg} = \frac{\lambda_1 + \lambda_2 + \lambda_3 + \lambda_4}{4}$$

(3.1)

then find the absolute difference between the individual gauges and the average
displacement by inserting Equation (3.1) into

$$\Delta\lambda_i = \left|\lambda_{Avg} - \lambda_i\right|$$

(3.2)

compare opposing gauges by finding the relative error between them for each data point

$$\%Error = \left|\frac{\lambda_{1,j} - \lambda_{2,j}}{\lambda_{1,j}}\right|$$

(3.3)

then the percent error of all the data points can be averaged to determine the threshold
error to determine whether a gauge is broken.

The calibration tests can be used to determine average error between opposing
gauges during transverse displacement. The transverse displacement was controlled
during these tests, and which gauges were being displaced was known. The method
described above was done for the gauges that compressed and extended during the
calibration tests, and compared to the average displacement of all four gauges. The result
from the analysis of the calibration tests indicates approximately 8% error difference
between two functioning and opposing gauges.

Application to CO2 Sequestration

An objective of the research was to evaluate the feasibility of using the 3DX for applications during CO2 sequestration. This includes aquifer characterization in deep formations, and well casing monitoring during CO2 injection. In order to accomplish this we needed a device that could measure 3D displacements to improve aquifer characterization techniques. The results and interpretations from the field tests demonstrate that the 3DX can be used for aquifer characterization during hydromechanical well tests. The same methods could be applied to characterizing deep formations.

CONCLUSIONS

The 3DX is an instrument that has the capability of measuring 3D displacements in wells using multiple fiber optic strain gauges. These sensors are not affected by electronic interference so multiple devices can be used in or near the well, or a pump can also be used in the same well. The 3DX underwent calibration tests by inserting the device into frames that transversely and axially displacing the anchors. The device was displaced by a known amount to analyzing how the gauges reacted, and correlate the results from the gauges to 3D displacement that occurs relative to the two anchors. The axial displacement test involved hanging weights from the 3DX and measuring the induced axial displacement, and measuring the response from the gauges. The transverse displacement involved moving the top anchor horizontally, and measuring the response from the gauges. The tests correlate the measurements from the gauges to the displacement through the rod constant (C_r) which is used to determine transverse displacement and the axial constant (C_A) used to determine axial displacement. Multiple calibration tests were done, and the results were similar in magnitude and trend. The 5 minute RMS noise for axial displacement is 30 nm, and for transverse displacement 5 min RMS noise is 180 nm.

The 3DX was used in Tsukuba, Japan during hydromechanical well tests as a proof of concept for the device. The performance of the device was confirmed during a test when a slug was introduced, followed by recovery, then the well was pumped and allowed to recover. The well bore extended axially when the slug was introduced, closed during recovery, closed when the formation was pumped, and opened during recovery

117

from pumping. The axial displacement as a function of pressure was hysteretic loop and the magnitude was similar to previous findings (Svenson et al. 2007; Schweisinger, 2008, Hisz et al. 2012).

A series of tests was of hydromechanical well tests were done in LAR-2 at a depth of 24.3 meters at the Clemson well field using the 3DX. A permeable fracture zone in LAR-2 strikes east to east, and dips to the south. The axial displacement decreased 3.4 μm during pumping and increased during recovery as a hysteric function. The transverse displacement during pumping was generally towards the southeast for all the tests. The magnitude of the transverse displacement was between 6 *μm* and 8.5 *μm*. Another test was done in LAR-4 and the results were compared with findings from the Tilt-X. In this case the transverse displacement was to the southwest for both the 3DX and the Tilt-X.

The 3DX was monitored in LAR-2 for 5 days, and measured displacement in response to barometric pressure changes and other ambient effects. The well bore opened when the barometric pressure increased, and closed when the barometric pressure decreased. This Tilt-X was measuring well bore displacement in LAR-4 at the same time, and showed a similar response. The transverse displacement during ambient conditions was to the north when the fracture closed and to the south when the fracture opened.

The 3D displacement responses during pumping and during ambient monitoring are both affected by the dip of fractures. The fracture transversely displaces up dip when the fracture closes and down dip when the fracture opens during ambient conditions. The dip causes the tilt field to radiate from a point approximately 5 m up-dip from the well

during pumping, according to theoretical analyses. The dip estimated from the axial and

transverse displacement is steeper than expected from other field measurements. The

current results show that the 3DX data predicts the correct strike and dip direction, but

over-predicts the dip of the fracture.

REFERENCES

Alm, P. 1999. Hydro-mechanical behaviour of a pressurized single fracture: An in-situ experiment. Ph.D. Dissertation, Geology, Chalmers University of Technology, Goteborg.

Bai, M. and D. Elsworth (2000). Coupled Processes in Subsurface Deformation, Flow and Transport. Reston, Va, ASCE.

Bachu, S. (2000). Sequestration of CO2 in geological media: Criteria and approach for site selection in response to climate change. Energy Conversion and Management, 41(9), 953-970. doi:10.1016/S0196-8904(99)00149-1

D.C. Baird, Experimentation: An Introduction to Measurement Theory and Experiment Design (Prentice-Hall, 1962)

Barker, J. A., & - Black, J. H. - *Slug tests in fissured aquifers* - AGU. doi:- 10.1029/WR019i006p01558

Barker, J. A. - A generalized radial flow model for hydraulic tests in fractured rock - AGU. doi:- 10.1029/WR024i010p01796

Beauheim, R. L. and R. M. Roberts "Flow-Dimension Analysis of Hydraulic Tests to Characterize Water-Conducting Features." Department of Energy.

Biot, M, 1956, Theory of Propagation of Elastic Waves in a Fluid-Saturated Porous Solid, Part I: Low Frequency Range" and "Part II: Higher Frequency Range: Journal of the Acoustical Society of America, v. 28, p. 168-178 and 179-191.

Butler, J.J., Jr., 1997, The design, performance, and analysis of slug tests: Lewis Publishers, Washington, D.C., 252 p.

Burbey, T. J., Hisz, D., Murdoch, L. C., & Zhang, M. (2012). Quantifying fractured crystalline-rock properties using well tests, earth tides and barometric effects. *Journal of Hydrology,* 414–415(0), 317-328. doi:10.1016/j.jhydrol.2011.11.013

Burbey, T.J., Helm, D.C., 1999. Modeling three-dimensional deformation in response to pumping of unconsolidated aquifers. Environmental and Engineering Geoscience 5 (2),
199–212.

Cappa, F. 2005. Coupled hydromechanical processes in heterogeneous fracture networksfield characterization and numerical simulations. Ph.D. Dissertation, University of Nice-Sophia Antipolis, Nice, France.

Cappa, F., Guglielmi, Y., Fénart, P., Merrien-Soukatchoff, V., & Thoraval, A. (2005). Hydromechanical interactions in a fractured carbonate reservoir inferred from hydraulic and mechanical measurements. *International Journal of Rock Mechanics and Mining Sciences, 42*(2), 287-306. doi:10.1016/j.ijrmms.2004.11.006

Cappa, F., Guglielmi, Y., Gaffet, S., Lançon, H., & Lamarque, I. (2006). Use of in situ fiber optic sensors to characterize highly heterogeneous elastic displacement fields in fractured rocks. *International Journal of Rock Mechanics and Mining Sciences, 43*(4), 647-654. doi:10.1016/j.ijrmms.2005.09.016

Cappa, F., Guglielmi, Y., Rutqvist, J., Tsang, C-F, and Thoraval, A., 2009, Hydromechanical Modeling of Pulse Tests that Measure both Fluid Pressure and Fracture-Normal Displacement of the Coaraze Laboratory Site, France: Lawrence Berkeley National Laboratory Paper LBNL-60442, http://repositories.cdlib.org/lbnl/LBNL-60442.

Cappa, F., Guglielmi, Y., Rutqvist, J., Tsang, C-F, and Thoraval, A., 2009, Estimation of fracture flow parameters through numerical analysis of hydromechanical pressure pulses

Comerlati, A., - Ferronato, M., - Gambolati, G., - Putti, M., & - Teatini, P. - *Saving venice by seawater* - AGU. doi:- 10.1029/2004JF000119

Cooper, H. H., JR., & C. E. Jacob. 1946. A generalized graphical method for evaluating formation constants and summarizing well-field history. Transactions, American Geophysical Union 27:526-34.

Cornet, F. H., Li, L., Hulin, J. -., Ippolito, I., & Kurowski, P. (2003). The hydromechanical behaviour of a fracture: An in situ experimental case study. *International Journal of Rock Mechanics and Mining Sciences, 40*(7–8), 1257-1270. doi:10.1016/S1365-1609(03)00120-5

Dawson, Karen and Istok, Jonathan, 1991, Aquifer Testing: Design and Analysis of Pumping and Slug Tests: Lewis Publishers, 280 p.

D.C. Baird, Experimentation: An Introduction to Measurement Theory and Experiment Design (Prentice-Hall, 1962)

Doe. T.W. (1991). "Fractional Dimension Analysis of Constant-pressure Well Tests." Proceedings: 1991 SPE Annual Technical Conference and Exhibition, 6-9 October.

Doe, T., and J.D. Osnes. 1985. Interpretation of fracture geometry from well tests. *Proc. Fundamentals of Rock Joints, Bjorkliden, Sweden*:281-292.

Doe, T.W., J.C.S. Long, H.K. Endo, and C.R. Wilson. 1982. Approaches to evaluating the permeability and porosity of fractured rock masses. Paper read at Proceedings of the 23rd U.S. Rock Mechanics Symposium, at Berkeley, Calif.

Elsworth, D., and T.W. Doe. 1986. Application of non-linear flow laws in determining rock fissure geometry from single borehole pumping tests. *International Journal of Rock Mechanics Mining Sciences & Geomechanics Abstracts* 23 (3):245-254.

Fabian, M., & Kümpel, H. -. (2003). Poroelasticity: Observations of anomalous near surface tilt induced by ground water pumping. *Journal of Hydrology, 281*(3), 187-205. doi:10.1016/S0022-1694(03)00234-8

Fenske, P.R. 1984. Unsteady drawdown in the presence of a linear discontinuity. *Water Resources Monograph* 9:125-145.

Fetter, C., 2001, Applied Hydrogeology, Fourth Edition, Prentice Hall Publishers.

Forms of hydraulic fractures created during a field test in overconsolidated glacial drift : L. C. murdoch, quarterly journal of engineering geology, 28(1), 1995, pp 23–35.(1995). International Journal of Rock Mechanics and Mining Sciences & Geomechanics Abstracts, 32(8), A390-A391. doi:10.1016/0148-9062(95)99620-D

Frere, J.M., and Baker, J.E. 1995. Use of soil fracturing to enhance soil vapor extraction, a case study. In Proceedings of the ACS Specialty Symposium on Emerging Technologies in Hazardous Waste Management VII, Atlanta, Ga., 17-20 September 1995. American Chemical Society (ACS), Washington, D.C. pp. 17-20

Gale, J.E. 1975. A numerical, field and laboratory study of flow in rocks with deformable fractures. Ph.D. Dissertation, University of California @ Berkeley, Berkeley.

Geertsma, J. 1957, The effect of fluid-pressure decline on volumetric changes of rocks: Trans. AIME, v. 210, p. 331–338.

Grader, A.S. 1991. Slug test; double-porosity, linear boundary, and variable storage effects.Paper read at International symposium on Ground water in practice. Nashville, TN,United States, July 29-Aug. 2, 1991.

Grattan, K. T. V., & Sun, T. (2000). Fiber optic sensor technology: An overview. *Sensors and Actuators A: Physical, 82*(1–3), 40-61. doi:10.1016/S0924-4247(99)00368-4

GRINGARTEN, A. C. (1971). UNSTEADY-STATE PRESSURE DISTRIBUTIONS CREATED BY A WELL WITH A SINGLE HORIZONTAL FRACTURE, PARTIAL PENETRATION, OR RESTRICTED ENTRY. (Ph.D., Stanford University). *ProQuest Dissertations and Theses,* Retrieved from http://search.proquest.com/docview/302557758?accountid=6167

Hakami, E., & Larsson, E. (1996). Aperture measurements and flow experiments on a single natural fracture. *International Journal of Rock Mechanics and Mining Sciences & Geomechanics Abstracts, 33*(4), 395-404. doi:10.1016/0148-9062(95)00070-4

Hantush, M. S. 1956. Analysis of data from pumping tests in leaky aquifers. Transactions, American Geophysical Union 37:702-14

Heath, R., 1989, The Piedmont Ground-Water system: in Proceedings of a Conference on Ground Water in the Piedmont of the Eastern United States, held October 16-18, 1989, E.D. Daniel, C., White, R., and Stone, P., p. 1-13.

Hisz, D. B. (2010). Predicting long-term well performance from short-term well tests in the piedmont. (M.S., Clemson University). *ProQuest Dissertations and Theses,* Retrieved from http://search.proquest.com/docview/758397228?accountid=6167

Hisz, D. B., Murdoch, L. C., & Germanovich, L. N. (2012). A portable borehole extensometer and tiltmeter for characterizing aquifers.

Indraratna, B., & Ranjith, P. G. (2001). Laboratory measurement of two-phase flow parameters in rock joints based on high pressure triaxial testing. *Journal of Geotechnical & Geoenvironmental Engineering, 127*(6), 530. Retrieved from http://search.ebscohost.com/login.aspx?direct=true&db=a9h&AN=4484927&site=ehost-live

Intergovernmental Panel on Climate Change. Climate change: the IPCC response strategies. Washington, DC: Island Press, 1991, p. 272.

Jancin, M., & Ebaugh, W. F. (2002). Shallow lateral DNAPL migration within slightly dipping limestone, southwestern kentucky. Engineering Geology, 65(2–3), 141-149. doi:10.1016/S0013-7952(01)00121-1

Karasaki, K., - Long, J. C. S., & - Witherspoon, P. A. - *Analytical models of slug tests -* AGU. doi:- 10.1029/WR024i001p00115

Kim, J., & Parizek, R. R. (1997). Numerical simulation of the noordbergum effect resulting from groundwater pumping in a layered aquifer system. *Journal of Hydrology, 202*(1–4), 231-243. doi:10.1016/S0022-1694(97)00067-X

Kim, J., & Parizek, R. R. (2005). Numerical simulation of the rhade effect in layered aquifer systems due to groundwater pumping shutoff. *Advances in Water Resources, 28*(6), 627-642. doi:10.1016/j.advwatres.2004.12.005

Kruseman, G.P., and N.A. deRidder. 1994. Analysis and evaluation of pumping test data. 2nd ed. The Netherlands: International Institute for Land Reclamation and Improvement.

Kumpel, H.-J., 1989. Verformungen in der Umgebung von Brunnen. Habil. Thesis, Math.-Nat. Fak., Univ. Kiel.

Lecomte, E., Le Pourhiet, L., Lacombe, O., & Jolivet, L. (2011). A continuum mechanics approach to quantify brittle strain on weak faults: Application to the extensional reactivation of shallow dipping discontinuities. Geophysical Journal International, 184(1), 1-11. doi:10.1111/j.1365-246X.2010.04821.x

Lehmann, K., 2001. Porendruckinduzierte Neigungssignale in geringen Tiefen und ihre Modellierung im homogenen Halbraum. Berichte aus der Geowissenschaft. Shaker Verlag, Aachen. ISBN 3-8265-8902-5. Diss. Thesis, Math.-Nat. Fak., Univ. Bonn.

Leveinen, J. (2000). Composite model with fractional flow dimensions for well test analysis in fractured rocks. Journal of Hydrology, 234(3–4), 116-141. doi:10.1016/S0022-1694(00)00254-7

Long JCS, Remer CR, Wilson CR, Witherspoon PA. Porous media equivalents for networks of discontinuous fractures. Water Resources Research 1982; 18:645–658.

Moench, A.F. 1988. The response of partially penetrating wells to pumpage from doubleporosity aquifers. Paper read at International conference on Fluid flow in fractured rocks. Atlanta, GA, United States, May 15-18, 1988.

Martin, C., Davison, C., and Kozak, E., 1990, Characterizing Normal Stiffness and Hydraulic Conductivity of a Major Shear Zone in Granite: Rock Joints. Barton and Stephansson, eds. Balkema, Rotterdam, p. 549-556.

Murdoch, L. C., & Germanovich, L. N. (2006). Analysis of a deformable fracture in permeable material. *International Journal for Numerical and Analytical Methods in Geomechanics, 30*(6), 529-561. doi:10.1002/nag.492

Murdoch, L. C. (2010). In Moysey S., Germanovich L. N.(Eds.), Proof-of-feasibility of using well bore deformation as a diagnostic tool to improve CO2 sequestration

Murdoch, L. C., Germanovich, L. N., Ebenhack, J. F., & Skawski, G. M. (2011). Multi-dimensional displacement sensor

Murdoch, L. C. (2002). Mechanical analysis of idealized shallow hydraulic fracture. Journal of Geotechnical & Geoenvironmental Engineering, 128(6), 488. Retrieved from http://search.ebscohost.com/login.aspx?direct=true&db=a9h&AN=6785183&site=ehost-live

National Research Council, 1996, Rock Fractures and Fluid Flow: Washington D.C., National Academy Press, 551 pp.

Nelson, A.E., J.W. Horton, Jr., and J.W. Clarke. 1998. Geologic map of the greenville 1degree by 2 degrees quadrangle, georgia, south carolina, and north carolina.

Neuman, S. P., & P. A. Witherspoon. 1969. Applicability of current theories of flow in leaky aquifers. Water Resources Research 5:817-29.

Neuzil, C. E., & - Tracy, J. V. - *Flow through fractures* - AGU. doi:-10.1029/WR017i001p00191

NGWA Press publication. (1999). Ground water hydrology for water well contractors.

Olsson, R., & Barton, N. (2001). An improved model for hydromechanical coupling during shearing of rock joints. International Journal of Rock Mechanics and Mining Sciences, 38(3), 317-329. doi:10.1016/S1365-1609(00)00079-4

Pollard, D., and Aydin, A., 1988, Progress in understanding jointing over the past century: Geological Society of America Bulletin, v. 100, p. 1181-1204.

Ruelleu, S., Moreau, F., Bour, O., Gapais, D., & Martelet, G. (2010). Impact of gently dipping discontinuities on basement aquifer recharge: An example from ploemeur (brittany, france). Journal of Applied Geophysics, 70(2), 161-168. doi:10.1016/j.jappgeo.2009.12.007

Rutqvist, J. (1995). Coupled stress-flow properties of rock joints from hydraulic field testing. (Takn.dr, Kungliga Tekniska Hogskolan (Sweden)). *ProQuest Dissertations and Theses,* Retrieved from http://search.proquest.com/docview/304288006?accountid=6167

Rutqvist, J., - Noorishad, J., - Tsang, C., & - Stephansson, O. - *Determination of fracture storativity in hard rocks using high-pressure injection testing* - AGU. doi:-10.1029/98WR01863

Rutqvist, J., & Stephansson, O. (2003). *The role of hydromechanical coupling in fractured rock engineering* Springer Berlin / Heidelberg. doi:10.1007/s10040-002-0241-5

Schmidt-Hattenberger, C., Naumann, M., & Borm, G. (2003). Fiber bragg grating strain measurements in comparison with additional techniques for rock mechanical testing. *Sensors Journal, IEEE, 3*(1), 50-55.

Schevenels, M., Degrande, G., and Lombaert, G., 2004, The Influence of Depth of the Groundwater Table on Free Field Road Traffic-Induced Vibrations: *International Journal*

Schweisinger, T., Svenson, E., & Murdoch, L. (2011). Hydromechanical behavior during constant-rate pumping tests in fractured gneiss Springer Berlin / Heidelberg. doi:10.1007/s10040-011-0728-z

Schweisinger, T., Svenson, E. J., & Murdoch, L. C. (2009). Introduction to hydromechanical well tests in fractured rock aquifers. Ground Water, 47(1), 69-79. doi:10.1111/j.1745-6584.2008.00501.x

Schweisinger, T. (2007). Measurement and analysis of hydromechanical effects in fractured rock. (Ph.D., Clemson University). *ProQuest Dissertations and Theses,* Retrieved from http://search.proquest.com/docview/304890754?accountid=6167

Schweisinger, T., and L. Murdoch. 2002. Measuring changes in fracture aperture during injection to estimate characteristics of fractured rock near a well. Eos. Trans. AGU 83(47, Fall Meeting Supplement):Abstract H71B-0821.

Setarri, A., 2002, A Reservoir Compaction: Journal of Petroleum Technology, v. 54, no.8, p.9-62.

Shapiro, A. M. (2002, Fractured-rock aquifers understanding an increasingly important source of water. U.S. Dept. of the Interior, U.S. Geological Survey,

Slack, T. Z. (2010). Hydromechanical interference slug tests in a fractured biotite gneiss. (M.S., Clemson University). *ProQuest Dissertations and Theses,* Retrieved from http://search.proquest.com/docview/751925535?accountid=6167

Streltsova, T.D. 1988. Well testing in heterogeneous formations (exxon monographs series): John Wiley& Sons.

Svenson, E., Schweisinger, T., & Murdoch, L. C. (2007). Analysis of the hydromechanical behavior of a flat-lying fracture during a slug test. Journal of Hydrology, 347(1–2), 35-47. doi:10.1016/j.jhydrol.2007.08.020

Svenson, E., Schweisinger, T., & Murdoch, L. C. (2008). Field evaluation of the hydromechanical behavior of flat-lying fractures during slug tests. Journal of Hydrology, 359(1–2), 30-45. doi:10.1016/j.jhydrol.2008.06.004

Svenson, E., 2006, Methods for Measuring and Analyzing Transient Head and Aperture Changes During Air-Slug Tests in Fractured Bedrock: Master's Thesis, Clemson University, 236 pp.

Terzhagi, K., 1936, The Shearing Resistance of Saturated Soils: in Proceedings of the International Conference on Foundation Engineering, Graduate School of Engineering, Harvard University, Boston, Spaulding Moss Company, p. 54-56.

Theis, C. V. 1935. The lowering of the piezometer surface and the rate and discharge of a well using ground-water storage. Transactions, American Geophysical Union 16:519-24.

Theodorakopoulos, D. D., Chassiakos, A. P., & Beskos, D. E. (2004). Dynamic effects of moving load on a poroelastic soil medium by an approximate method. *International Journal of Solids and Structures, 41*(7), 1801-1822. doi:10.1016/j.ijsolstr.2003.11.009

Thiem, G. 1906. Hydrologische methoden. Leipzig: Gebhardt, 56 pages

Thompson, P.M., and E.T. Kozak. 1991. In-situ measurement of coupled hydraulic pressure/fracture dilation in stiff crystalline rock. Paper read at Proceedings of the International Symposium on Field Measurements in Geomechanics, at Oslo, Norway.

Tsai, T. (2009). *Viscosity effect on consolidation of poroelastic soil due to groundwater table depression* Springer Berlin / Heidelberg. doi:10.1007/s00254-008-1391-0

Tseng, C., Tsai, T., and Huang, L., 2008, Effects of Body Force on Transient Poroelastic Consolidation Due to Groundwater Pumping: Environmental Geology, v. 54, p. 1507-1516.

Urlaub, M., & Fabian, M. (2011). Poroelasticity: Finite element modelling of anomalous tilt and pore pressure caused by pumping in a sedimentary half space with fault. *Journal of Geodynamics, 51*(4), 219-232. doi:10.1016/j.jog.2010.09.001

Wang, H., 2000, Theory of Linear Poroelasticity with Applications to Geomechanics and Hydrogeology: Princeton University Press, Princeton, New Jersey, 287 pp.

Wang, R., Ku¨mpel, H.-J., 2003. Poroelasticity: efficient modeling of strongly coupled slow deformation processes in multi-layered half-space. Geophysics, 68 (2), 705–717.

Williams, L., and Burton, W., 2005, Common Types of Water-Bearing Features in Bedrock, Rockdale County, Georgia: Proceedings of the 2005 Georgia Water Resources Conference, held April 25-27, 2005, e.d. Hatcher, K.

Witherspoon, P. A., - Wang, J. S. Y., - Iwai, K., & - Gale, J. E. - *Validity of cubic law for fluid flow in a deformable rock fracture* - AGU. doi:- 10.1029/WR016i006p01016

Wong, R.C.K., and Alfaro, M.C. 2001. Fracturing in low-permeability soils for remediation of contaminated ground. Canadian Geo-technical Journal, 38(2): 316-327.

Yeo, I. W., de Freitas, M. H., & Zimmerman, R. W. (1998). Effect of shear displacement on the aperture and permeability of a rock fracture. *International Journal of Rock Mechanics and Mining Sciences, 35*(8), 1051-1070. doi:10.1016/S0148-9062(98)00165-X

Yin, S., Dusseault, M. B., & Rothenburg, L. (2007). Analytical and numerical analysis of pressure drawdown in a poroelastic reservoir with complete overburden effect considered. *Advances in Water Resources, 30*(5), 1160-1167. doi:10.1016/j.advwatres.2006.10.008